Compressive Parallel MRI for Accelerated Imaging

Submitted in partial fulfillment of the requirements
of the degree of
Doctor of Philosophy
of the
Indian Institute of Technology, Bombay, India
and
Monash University, Australia
by

Kamlesh Pawar

Supervisors:

Prof. Arjun Arunachalam (IIT Bombay)
Prof. Jingxin Zhang (Monash University)

The course of study for this award was developed jointly by
Monash University, Australia and the Indian Institute of Technology, Bombay
and was given academic recognition by each of them.
The program was administered by The IITB-Monash Research Academy.

June - 2015

Approval Sheet

The thesis entitled "*Compressive Parallel MRI for Accelerated Imaging*" by *Kamlesh Pawar* is approved for the degree of **Doctor of Philosophy**

[redacted]

External Examiner

[redacted]

Internal Examiner

[redacted]

IITB Supervisor

[redacted]

Monash Supervisor

[redacted]

Date: 26/06/2015
Place: Mumbai

Declaration

I declare that this written submission represents my ideas in my own words and where others' ideas or words have been included, I have adequately cited and referenced the original sources. I also declare that I have adhered to all principles of academic honesty and integrity and have not misrepresented or fabricated or falsified any idea/data/fact/source in my submission. I understand that any violation of the above will be cause for disciplinary action by the Institute and can also evoke penal action from the sources which have thus not been properly cited or from whom proper permission has not been taken when needed.

Notice 1

Under the Copyright Act 1968, this thesis must be used only under the normal conditions of scholarly fair dealing. In particular no results or conclusions should be extracted from it, nor should it be copied or closely paraphrased in whole or in part without the written consent of the author. Proper written acknowledgement should be made for any assistance obtained from this thesis.

Notice 2

I certify that I have made all reasonable efforts to secure copyright permissions for third-party content included in this thesis and have not knowingly added copyright content to my work without the owner's permission.

[redacted]

Student Name : Kamlesh Pawar
IITB ID : 10407402
[redacted] [redacted]

Acknowledgments

I would like to express my special appreciation and thanks to my advisors Prof. Arjun Arunachalam and Prof. Jingxin Zhang, you both have been a tremendous mentor for me. I would like to thank you for encouraging my research and for allowing me to grow as a research scientist. Your advice on both research as well as on my career have been priceless. I would also like to thank my committee members, Prof. V. M. Gadre, Prof. Gary F Egan and Dr. David G Barnes for serving as my committee members even at hardship. I also want to thank you for your brilliant comments and suggestions. I would especially like to thank radiologist Richard McIntyre at Monash Biomedical Imaging facility for his valuable training and support in MRI data collection for my PhD thesis. I would like to thank all the staff at Monash Biomedical imaging for their support in using experimental facilities. I would like to thanks my colleagues Parnesh Raniga and Sulaiman Alhasani for their constructive discussions on research during my tenure at Monash University. I would also like to thank all of my friends who supported me during my stay at IIT Bomabay and Monash University during my PhD tenure.

A special thanks to my family. Words cannot express how grateful I am to my mother, brother and sister for all of the sacrifices that you‘ve made on my behalf. Your prayer for me was what sustained me thus far.

List of Publications

- K. Pawar, G. F. Egan and J. Zhang, "Multichannel Compressive Sensing MRI Using Noiselet Encoding", PLoS ONE, 10(5), 12 May 2015.
- K. Pawar, G. F. Egan and J. Zhang, "Accelerating k-t sparse using k-space aliasing for dynamic MRI imaging", Proceedings of the 35th Annual International conference of IEEE Engineering in Medicine and Biology Society, Osaka, Japan, July 2013.
- K. Pawar, A. Arunachalam, G. F. Egan and J. Zhang, "Noiselet Encoded Compressive Sensing Parallel MRI", Proceedings of the 10th IASTED International conference on Biomedical Engineering and IEEE EMBS (Acta Press), Innsbruck, Austria, Feb 2013.
- K. Pawar and A. Arunachalam, "Simultaneous Image and K-space Domain Aliasing for Accelerating Dynamic MRI Scans", Proceedings of the 20th Annual Meeting of ISMRM, Melbourne, Australia, 2012.
- A. Arunachalam and K. Pawar, "(RATE) Rapid MRI Acquisition using Tailored Signal Excitation modules: A K-space aliasing method to accelerate MRI scans", Proceedings of the 20th Annual Meeting of ISMRM, Melbourne, Australia, 2012.

Compressive Parallel MRI for Accelerated Imaging

Kamlesh Pawar, PhD Scholar
IIT Monash Research Academy, 2014

Supervisors:
Prof. Jingxin Zhang, Monash University
Prof. Arjun Arunachalam, IIT Bombay

Abstract

Magnetic Resonance Imaging (MRI) is one of the widely used imaging modalities in clinical practice due to its high quality diagnostic images. The good contrast between soft tissues provided by MRI makes it useful for a diverse range of clinical applications. It is used in a wide variety of clinical applications ranging from structural brain scans to detect tumors, functional neuro-imaging to analyse brain function, cardiovascular imaging to diagnose abnormalities in the heart and diffusion tensor imaging to map brain's neutral network to name a few. However these applications of MRI comes at a cost of its slow imaging speed compared to other imaging modalities such as Computed Tomography (CT) and ultrasound. Accelerating the data acquisition has been an active area of research since the advent of MRI. MRI acceleration techniques can be broadly classified in two categories, one is parallel imaging (PMRI) which uses knowledge of receiver coil sensitivities and second is compressive sensing (CS) which uses knowledge of inherent sparsity in MR images.

The objective of this thesis is to optimally combine the techniques of PMRI and CS to achieve higher acceleration and produce better quality images. This research has resulted in two novel acceleration techniques, one for static imaging and another for dynamic imaging.

The first technique "multichannel compressive sensing MRI using noiselet encoding" acquires reduced data in the noiselet domain and uses the knowledge of receiver coil sensitivities to reconstruct the image through a multichannel compres-

sive sensing (MCS) reconstruction. Simulations are presented in the MCS framework to compare the performance of noiselet encoding reconstructions and Fourier encoding reconstructions at different acceleration factors. The comparisons indicate that the multichannel noiselet measurement matrix has a better Restricted Isometery Property (RIP) than that of its Fourier counterpart, and that noiselet encoded MCS-MRI outperforms Fourier encoded MCS-MRI in preserving image resolution and can achieve higher acceleration factors. To demonstrate the feasibility of the proposed noiselet encoding scheme, a pulse sequence with tailored spatially selective RF excitation pulses was designed and implemented on a 3T scanner.

The second technique "k-space aliasing" uses multiple radio frequency (RF) excitation pulses to overlap different regions of k-space and simultaneously acquire all k-space data in a dynamic scan in a time span shorter than that of a full acquisition. The method exploits the fact that in most dynamic imaging, a non-uniform distribution of energy in k-space results in different k-space regions exhibiting different temporal bandwidths. In-vivo feasibility is first demonstrated for acceleration factor of 3 in 2D cardiac triggered imaging. Additionally, the method is combined with parallel imaging and compressive sensing to further accelerate the dynamic MRI scans.

Contents

List of Tables

List of Figures

Chapter 1

Introduction

1.1 Overview

Magnetic resonance imaging (MRI) or nuclear magnetic resonance imaging (NMRI) is a non invasive medical imaging technique used in radiology to visualize detailed internal structures. The first MR image was published in 1973 and the first cross-sectional image of a living mouse was published in January 1974. The first studies performed on humans were published in 1977. By comparison, the first human X-ray image was taken in 1895. MRI is a relatively new and advanced technology, it does not use any ionizing radiation and there are no known harmful effect of MRI examination. Instead it uses a powerful magnetic field to align the magnetization of hydrogen atoms in the body and then uses radio frequency (RF) fields to systematically alter the alignment of the magnetization. In response to a RF field, the excited region produces a rotating magnetic field detectable by the receive coils of the scanner, this information is recorded to construct an image of the scanned region of the body. MRI uses RF pulses to excite a region of interest, and magnetic field gradients are used to encode the excited region. In MRI, the combination of RF pulses and gradient waveforms is called a pulse sequence of MRI. The contrast in the MR images can be adjusted by tailoring the flip angle and the timing in the pulse sequence. MR images can provide different contrast of the region of interest called T1 and T2 relaxation. The good contrast between the soft tissues provided by MRI makes it useful in Neurology, Musculoskeletal, Cardiovascular and Cancer. Since MRI does not have any harmful radiations compared to CT, it is advisable to use MRI when both modalities can provide same diagnosis information.

1.2 Speed Limitation of MRI

The advantages of MR imaging comes at a cost of slow and long data acquisition times. MRI acquires data in the Fourier domain called k-space. In order to reconstruct a 2D image of the excited region, the whole of k-space needs to be traversed. In most of the basic pulse sequences, the k-space is traversed on a cartesian grid and one excitation is needed to acquire each line in k-space called a phase encoding line. This traversal is time consuming and often takes several minutes depending on the pulse sequence. For instance a spin echo sequence can take around 5-15 minute to acquire data for a single slice. The long scanning time of MRI results in patient discomfort and low throughput per day that limits the use of MRI for some dynamic imaging applications that require high spatial and temporal resolution. Often this limitation require radiographers to make a trade-off between spatial and temporal resolution in dynamic imaging applications such as cardiac cine, perfusion, angiography and function MRI, to name a few.

One important area in MRI where the sluggish imaging speed of MRI effects most is dynamic imaging. The goal of dynamic MRI is to capture the time evolution of a signal of interest through the fast acquisition of k-t space. Since MRI acquires signal from a preferred imaging location through the use of magnetic field gradients, only a sequential acquisition of k-t data is possible, this places fundamental restrictions on the maximum spatial and temporal resolution that can be simultaneously realized by a dynamic MRI acquisition. Over the years, several methods have been proposed to address this issue. Some of these methods make certain assumptions about the imaged object and/or temporal signal of interest [3–19], and other techniques operate independent of the same [20–24]. These assumptions, when made, are typically done so to exploit any spatial and/or temporal redundancy that may exist in the k-t data to be acquired.

Provided their assumptions hold, these methods can tailor the acquisition of k-t data to capture information efficiently. Irrespective of the assumptions, in all these approaches, the acquisition of k-t space is altered in an attempt to satisfy the competing requirements for spatial and temporal resolutions. Despite the advances, applications such as interventional imaging [25], contrast enhanced MR Angiography [26], evaluation of cardiac function [27] and abdominal imaging [28] can always benefit from larger acceleration factors. The fundamental limitation in these and other dynamic imaging applications continues to be the trade-off between spatial and temporal resolutions.

Accelerating data acquisition in MRI has been an active area of research since

the advent of MRI. Initially researchers focused on improving the hardware of the scanner to speed up the data acquisition process. This lead to fast and better gradient system which eventually have been used in fast imaging sequences such as EPI [29, 30], GRASE [31] and RARE [32]. However further improvement in the hardware could not be carried out with the same pace because of some fundamental and physiological limitations such as specific absorption rate (SAR) and nerve stimulation. Therefore, the later research in 1990's and early 2000's was focused on acquiring less amount of data and exploiting various redundancies in the MR acquisition process to reconstruct the desired image. The technique of Parallel Imaging (PMRI) [21, 23, 33–35] was one of them which uses information about the spatial sensitivities of the multiple receiver coils to reconstruct image from undersampled data. Another interesting active area of research that came up in late 2000's is compressive sensing (CS). Compressive sensing exploits the fact that MR images are sparse in wavelets/finite difference domain thus all of the data is not required for perfect reconstruction of the sparse representation of the image. CS acquires incoherent measurements and attempt to estimate the compressed representation of image from the randomly under-sampled data.

1.3 Research Aims and Technical Approaches

The objective of this research work is to optimally combine the existing techniques of parallel imaging and compressive sensing. This research work aims to achieve high acceleration factors and/or improve the image quality using both PMRI and CS in tandem. At the conception stage, extensive simulations were used to validate the new ideas. After validation of idea, MR pulse sequences were designed to implement the developed methods on and to acquire data from the MRI scanner for the validation of experimental feasibility of the proposed ideas/methods.

The novel contributions of this thesis are two new acceleration techniques. The first technique is developed to reduce scan time in static imaging and is called noiselet encoded multichannel compressive sensing MRI [36, 37]. The noiselets have certain favorable mathematical properties for CS such as they are unitary basis hence perfect reconstruction is possible from fully sampled data, they are completely incoherent with wavelet basis and spreads energy in measurement domain hence well suited for CS reconstruction from under-sampled data. Therefore, in order to take the advantage of these mathematical properties a new method of acquiring data in the noiselet domain is developed and implemented on a 3T MRI scanner. This new data acquisition and reconstruction method achieves better

image quality and higher acceleration factors than conventional Fourier encoding. The second technique is developed for dynamic imaging called k-space aliasing [38] that uses multiple excitation pulses to acquire k-space data in aliased form. The acquired aliased k-space is then un-aliased in the post processing using a simple Fourier transformation along time frames. This technique of k-space aliasing is combined with the technique of PMRI and CS to achieve further acceleration in MR imaging [39].

1.4 Thesis Structure

In chapter 2 fundamentals of MR physics, MR signal generation, data acquisition and MR image reconstruction is presented. This chapter provides a literature survey of the various existing methods in the field of accelerated MR imaging, which includes parallel imaging techniques - SENSE [21], SMASH [34], AUTO-SMASH [35] and GRAPPA [23]. An introduction to the theory of compressive sensing and its application to MRI is also presented in this chapter.

In chapter 3, a new technique is developed to address the imaging speed problem in static MRI. A compressive sensing technique that acquires data in noiselet domain instead of conventional Fourier domain is described in detail. A detailed theory is developed to use noiselets in compressive sensing MRI. The design and implementation details of pulse sequence to acquire noiselet encoded data is described and experimental results are presented. The simulation and experimental studies that compare the performance of the proposed noiselet encoding and conventional Fourier encoding are also presented here.

In chapter 4, a new technique for accelerating dynamic MRI scans called k-space aliasing is developed. The theory of k-space aliasing is described in detail followed by the reconstruction method for k-space un-aliasing. A design and implementation of pulse sequence for k-space aliasing is presented followed by invivo cardiac cine experimental results. A combination of k-space aliasing with the parallel imaging technique GRAPPA is also presented here.

In chapter 5, an existing compressive sensing method for accelerating cardiac cine scans called k-t sparse is presented. This method is combined with our technique of k-space aliasing to further accelerate cardiac cine scans. A comparative experimental study is presented that compares the performance of the proposed combination with the existing method of k-t sparse.

In chapter 6, contributions of the thesis are summarized and some possible extensions for future work are proposed.

Chapter 2

Principles of MRI and Acceleration Techniques

2.1 MRI Physics

An understanding of MRI physics at atomic level requires quantum mechanics. However, a classical treatment is simple to understand the macroscopic behavior of the atoms. MRI is a spectroscopic method where the image is formed by localizing the Nuclear Magnetic Resonance (NMR) signal by frequency [1]. The phenomenon of NMR arises in atoms with odd number of protons/neutrons since they possess a nuclear spin. These individual spinning charges have an associated small magnetic moment. MRI acquires signal generated from these spinning nuclei to reconstruct image of internal organs of human body. The Hydrogen (1H proton) atom is most abundant in the body and therefore MRI essentially acquires signal generated from these hydrogen atom. The hydrogen atoms act as a tiny magnet and in the absence of any external magnetic field, they are randomly oriented in space in such a way that the net magnetization due to all atoms is zero (Fig. 2.1 (a)). When a uniform magnetic field B_0 is applied, all the atoms either aligned parallel or anti parallel to the direction of the applied magnetic field (Fig. 2.1 (b)). This give rise to a net magnetization in the direction of magnetic field (M). Interaction of these spins with radio frequency field B1 is used to generate MR signal and linear gradient field G is used to encode the signal on to the Fourier space known as k-space. In the sections following this we will describe the interaction of spins with the three magnetic field (B0, B1 and gradients) present in the MRI scanner.

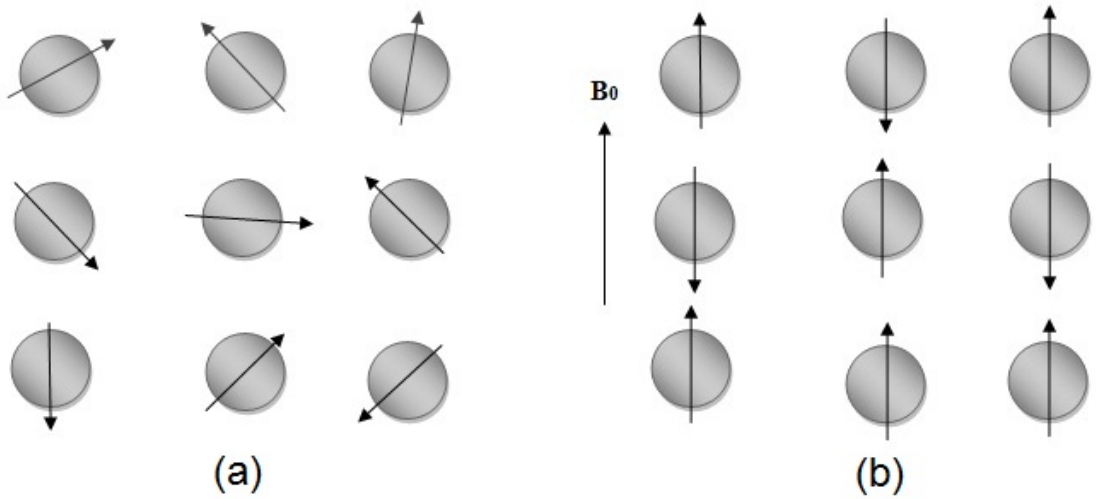

Figure 2.1: (a): Spins of hydrogen atoms randomly aligned in the absence of magnetic field B_0; **(b):** Spins of hydrogen atoms aligned parallel and anti-parallel to the applied magnetic filed B_0, here the number of spins aligned parallel are more than that of spins aligned anti-parallel.

2.1.1 Interaction with Static Magnetic Field B_0

When nuclear spins are subjected to a static magnetic field, B_0 in the z direction, the spins align in the direction of B_0, giving rise to a net magnetization vector M. This effect is termed as magnetization. These aligned spins exhibits resonance and precesses at a well defined frequency called Larmor frequency. The spin angular momentum of a proton is a vector quantity expressed as

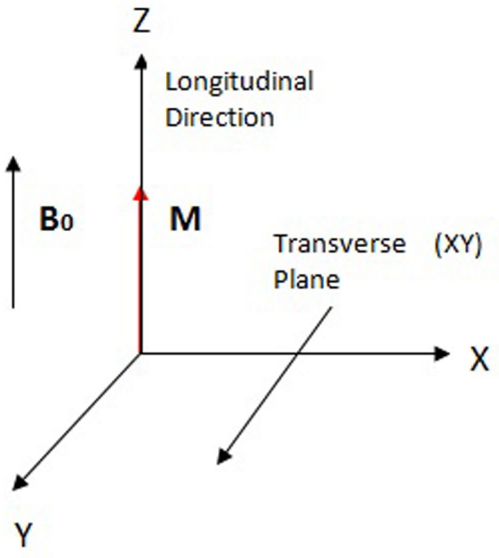

Figure 2.2: Axis convention in MRI

$$S = \frac{h}{2\pi} \tag{2.1}$$

where h is Planck's constant. And I is called the spin operator in quantum mechanics. For hydrogen $I = \pm 1$. The magnetic dipole moment associated with S is given by

$$\mu = \gamma S \tag{2.2}$$

where γ is called the gyromagnetic ratio of the proton (42.58 MHz T^{-1}).Therefore, per unit volume of the magnetic dipole moment $M = \sum \mu$.

Fig. 2.2 shows the axis conventions. The z direction is called the longitudinal direction while the xy direction is called the transverse direction. At thermal equilibrium, M and B will be pointing in the same direction. If M is made to point in a different direction than B, precessional behavior of the magnetization will occur. The torque applied to the dipole moment μ in the presence of B is $\mu \times$B and torque is equal to rate of change of angular momentum.

$$\frac{dS}{dt} = \mu \times B \tag{2.3}$$

Multiplying both sides by γ

$$\frac{dS}{dt} = \mu \times \gamma B \tag{2.4}$$

The solution to this equation is for M to precess about B at a frequency, known as **Larmor frequency**, given by

$$\omega = \gamma B \quad rad/sec \tag{2.5}$$

$$f = \gamma \frac{h}{2\pi} B \quad Hz \tag{2.6}$$

The magnetization is resonant at this well-defined frequency.

2.1.2 Bloch Equation

To describe the dynamics of the nuclear magnetization we combine Eq.2.4 with Eq.2.9 and Eq.2.12, which gives rise to Bloch equation

$$\frac{dM}{dt} = \mu \times \gamma B - \frac{M_x i + M_x j}{T_2} - \frac{(M_z - M_o)k}{T_1} \tag{2.7}$$

where
γ is gyromagnetic ratio
T_1 is spin-lattice (longitudinal-z) relaxation time constant
T_2 is spin-spin (transverse-xy) relaxation time constant
i, j, k are unit vectors in x,y,z - directions respectively
The cross product relation describes a precessional behaviour while the relaxation terms describe the exponential behaviour of both the longitudinal and transverse components.

2.1.3 Interaction with the Radiofrequency Field B_1

A magnetic field B_1 applied in the transverse direction and rotating at the Larmor frequency induces a torque on the magnetization, causing M to rotate away from the equilibrium position along z while precessing about the z-axis. The frequency of rotation away from the z-axis is $\omega = \gamma B_1$, an analogous result to the Larmor relationship. Following this excitation, the magnetization will continue to precess about the z axis at a processional frequency proportional to the applied field(B_1). Given a transverse component to the magnetization, detection of the magnetization becomes possible via Faraday's law of induction. The detection occurs because the precessing magnetization causes a change in flux ϕ in the coil, thereby inducing a small electromotive force (EMF)

$$\epsilon = \frac{\partial \phi}{\partial t} \tag{2.8}$$

The resulting time signal is known as free induction decay (FID) as shown in Fig. 2.3 and represents a basic MR signal that is recorded. The common excitation angle is 90° in which magnetization gets rotated completely to the xy plane and corresponds to a largest possible recordable signal. Eventually M returns to its equilibrium state along z. This implies that the transverse component M_{xy} must decay away and longitudinal component M_z must regrow. Following the excitation, the transverse component of the magnetization decays away while the longitudinal component returns to its thermal equilibrium state. Two MR parameters, T_1 and T_2, characterize this return to equilibrium and are called **relaxation time constants**.

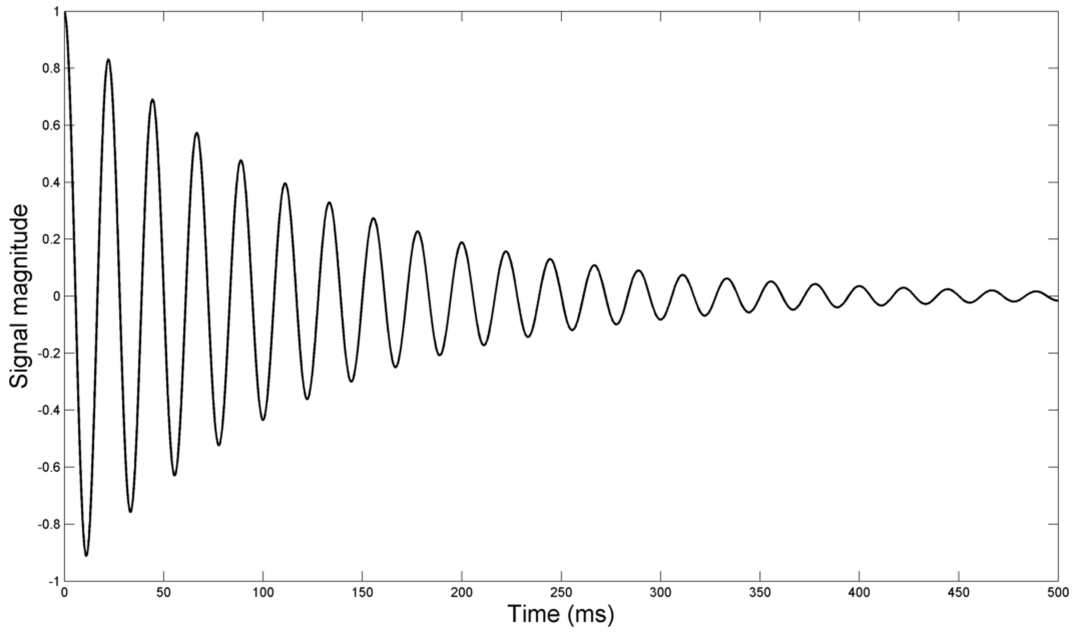

Figure 2.3: Free induction decay signal generated in the transverse plane (xy-plane) after excitation with 90° RF pulse.

2.1.4 Longitudinal Relaxation

In the presence of a strong static magnetic field the spins are in thermal equilibrium resulting in magnetization M_0 in the longitudinal direction. After applying a 90° RF pulse, the longitudinal component of the magnetization behaves according to

$$\frac{dM_z}{dt} = \frac{M_z - M_0}{T_1} \tag{2.9}$$

The solution of this equation is

$$M_z = M_0 + (M_z(0) - M_0)e^{-t/T_1} \tag{2.10}$$

Following a 90° excitation $M_z(0) = 0$. Therefore

$$M_z = M_0(1 - e^{-t/T_1}) \tag{2.11}$$

T_1 is called the spin-lattice time constant and characterizes the return to equilibrium along the z-direction. The longitudinal relaxation curve is shown in Fig. 2.4(a). Physically this involves the exchange of energy between the nuclei and the surrounding lattice. Thermal equilibrium occurs when M_z is restored to M_0. This happens when the lowest energy state is reached.

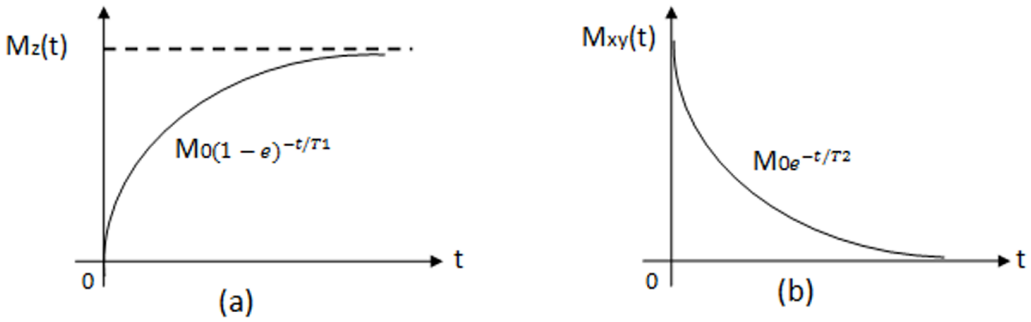

Figure 2.4: (a) Longitudinal relaxation time curve: With the 90° excitation pulse the longitudinal component becomes zero. Following the 90° excitation pulse the spins comes back to thermal equilibrium and longitudinal magnetization recovers exponentially with the time constant T_1. (b) Transverse relaxation time curve: With the 90° excitation pulse all the spins flips into the transverse plane resulting in magnetization M_0 in transverse plane. Following the 90° excitation pulse the spins comes back to thermal equilibrium and the transverse magnetization decays exponentially with the time constant T_2, this decay results from the dephasing of spins in the transverse plane

2.1.5 Transverse Relaxation

In the presence of a strong static magnetic field all the spins are aligned along the longitudinal direction resulting in zero magnetization in transverse plane. after 90° excitation RF pulse the behavior of transverse component of the magnetization is described by

$$\frac{dM_{xy}}{dt} = -\frac{M_{xy}}{T_2} \tag{2.12}$$

The solution (after a 90° excitation -$M_{xy}(0) = M_0$) is simply

$$M_{xy} = M_0 e^{(-t/T_2)} \tag{2.13}$$

T_2 is called the spin-spin time constant and characterizes the decay of transverse magnetization. The intermolecular interaction of the spins results in dephasing among the spins in the transverse plane resulting in T_2 decay. The transverse relaxation curve is shown in Fig. 2.4(b). However T_2 relaxation process also depend on z-component field fluctuations, therefore $T_2 < T_1$. The z-component fluctuations often dominate T_2 relaxation process. The relaxation due to z-component fluctuations is called the T_2* decay. In the presence of field fluctuations in z-component, the transverse component dephase rapidly resulting in very fast decay of transverse component characterized as T_2* decay.

2.2 Interaction with the Magnetic Gradient Field

Distribution of spinning hydrogen can be estimated from the FID signal which is characterized by the precession frequency. However, it is not possible to acquire signal separately from individual spinning hydrogen atom, the signal acquired by the receiver coils will be summation of the signal emanating from the entire excited region of interest. Therefore to estimate the distribution of hydrogen atom in space, linear gradient fields are used to create a spatial localization. This spatial localization is achieved by using linear magnetic field gradients (G) on top of static magnetic field B_0. Gradients can create a linearly varying magnetic field across the bore of the scanner in all three directions. With the application of linear gradient the resonance frequency of protons varies in space and a signal equivalent to the bandwidth of precessing protons is generated.

2.2.1 X-Gradient Field

If we apply a gradient, G_x in the x-direction, then the applied field is $B_0 + G_x x$. The frequency of spins thus becomes a function of their x-locations. i.e. $\omega(x) = \gamma(B_0 + G_x x) = \omega_0 + \gamma G_x x$. So if a constant G_x is turned on after an excitation, the recorded time (FID) signal contains contribution from oscillators emitting signals over a range of frequencies. Therefore, the Fourier transform of the FID time signal determines the contribution from each frequency which in turn linearly maps to a particular position. So a one dimensional image can be formed since x-position is encoded as temporal frequency.

2.2.2 Selective Excitation through Z Gradient Field

If B_1 is applied in the presence of B_0, then all spins are at the same resonance frequency and the excitation is non-selective as all spins in the volume are tipped. This necessitates a 3D imaging to be performed which is usually a time consuming endeavor unless image contrast or spatial resolution is compromised. Hence it is desirable to reduce 3D imaging into a manageable 2D one by exciting a plane. Such a selective excitation is achieved by applying B_1 in presence of B_0 and a linear gradient field G_z. If we wish to excite a plane perpendicular to the z-axis of thickness $\triangle$Z, then G_z turns on during the RF excitation. With G_z on the resonance frequency varies along the z-position. As B_1 must be tuned to the Larmor frequency for excitation to occur, B_1 must possess temporal frequency bandwidth that matches the bandwidth of resonance frequencies of the spins in

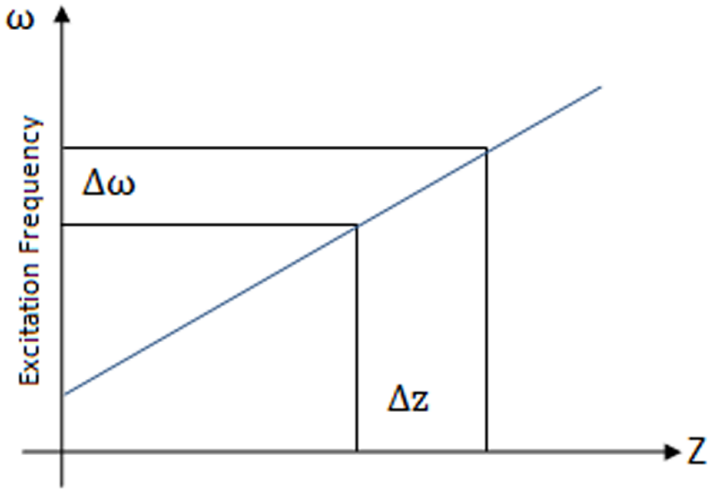

Figure 2.5: Selective excitation of a slice perpendicular to Z-axis by the RF Pulse. The gradient in Z-direction makes the spins to precess at different frequency and the bandwidth of the RF excitation pulse determines the thickness of slice.

the slice of interest. The desired bandwidth is $\triangle\omega = \gamma G_z \triangle \mathrm{Z}$, centered about ω_0 for excitation of the plane at Z = 0 (Fig. 2.5).To achieve a slice excitation with a rectangular profile, the frequency content of B_1 must be a rectangular function. Thus if Fourier transform of B_1 is to be a rectangular function, and then ideally B_1 must be a sinc function.

2.2.3 2D Fourier Transform Imaging Method

After a selective excitation of a 2D section, the signal readout occurs in the presence of a constant gradient field G_x and a FID time signal $S_r(t)$ is recorded. At a particular location all the spins along y oscillate at the same frequency and therefore sum to give the value at that frequency bin. This signal corresponds precisely to acquiring a projection in which the line integrals are along the y-direction. Thus the Fourier transform of $S_r(t)$ directly gives the projection of magnetization $m(x, y)$ along the y-direction. Going for a phased representation of the rotating magnetization vectors, the signal generated by the oscillator at position (x, y) can be written as $m(x, y)e^{-\omega t}$ where $m(x, y)$ is a complex quantity given by $m(x, y) = m_x(x, y) + im_y(x, y)$ and ω is the frequency of rotation of the vector $e^{-\omega t}$. In the presence of the gradient in the x direction, the frequency is spatially dependent and given by $\omega(x) = \omega_0 + \gamma G_x x$.
The total received signal $S_r(t)$ can be written by integrating over the entire excited

plane.

$$S_r(t) = \int_x \int_y m(x,y) e^{-i\omega t} e^{-i\gamma G_x x t} dx dy \tag{2.14}$$

Since we are interested in the base band signal, the base band signal $s(t)$ is expressed as

$$s(t) = S_r(t) e^{+\omega t} \tag{2.15}$$

$$= \int_x \int_y m(x,y) e^{-i\gamma G_x x t} dx dy \tag{2.16}$$

However, this signal does not provide the object distribution along the ray path. So $m(x,y)$ is to be spatially weighted in some clever way before the projection takes place.

2.2.4 Y-Gradient Field

To effectively apply the spatial frequency weighting factor in MR, a gradient G_y in the y direction is turned on a time t_y before recording the FID. As a result the spins which were originally in phase become increasingly out-of-phase with time. i.e., the phase of the spins oscillating at $\omega(y) = \omega_0 + \gamma G_y y$ after an interval t_y is $\omega_0 t_y + \gamma G_y t_y y$. In essence the spins are spatially phase-encoded by the time the FID is to be recorded, with the amount of phase encoding dependent on the amplitude G_y and on the interval t_y. Because $m(x,y)$ is complex valued, the distribution becomes weighted by the complex exponential corresponding to the spatial frequency $(\gamma/2\pi)G_y t_y$ and the distribution that is projected at time t_y is $m(x,y)e^{-i\gamma G_y t_y y}$.

Once all FIDs are assembled, a simple 2D Inverse Fourier transform is used to reconstruct $M(X,Y)$. Effectively, when the Fourier transform is performed in the k_x-direction, the FID time signal transforms into projections, each projection corresponding to a particular k_y spatial frequency component. Now, if a Fourier transform is performed on these projections in the k_y-direction, yields the object distribution $m(x,y)$. The baseband signal is written as

$$s(t, t_y) = \int_x \int_y [m(x,y) e^{-i\gamma G_y t_y y}] e^{-i\gamma G_x x t} dx dy \tag{2.17}$$

Let $g_{t_y}(x) = \int_x m(x,y)e^{-i\gamma G_y t_y y}dy$ be the line integral of $m(x,y)e^{-i\gamma G_y t_y y}dy$, then

$$s(t,t_y) = \int_x\int_y g_{t_y} e^{-i\gamma G_x x t}dxdy \tag{2.18}$$

Thus $s(t,t_y)$ provides information about $g_{t_y}(x)$ the projection of phase warped version of $m(x,y)$. Generalized form can written as

$$s(t,t_y) = \int_x\int_y [m(x,y)e^{-i\gamma G_y t_y y}]e^{-i\gamma G_x x t}dxdy \tag{2.19}$$

$$= F_{2D}[m(x,y)]|_{k_x=(\gamma/2\pi)G_x t, k_y=(\gamma/2\pi)G_y t_y} \tag{2.20}$$

So after assembling all FIDs (and therefore all horizontal lines in Fourier space), we simply take the inverse 2-D transform to reconstruct $m(x,y)$.

2.3 K-space and Spatial Aliasing

k-space is the spatial frequency space which is the original domain in which data is acquired in MRI. k-space is discretely sampled. The resolution of the final image is determined by the highest spatial frequency sampled (Ω_x and Ω_y) while the field of view is determined by the sampling rate ($\triangle k_x$ and $\triangle k_y$.)
The Nyquist theorem implies the following inequalities:

$$\triangle kx \leq \frac{1}{2\Omega_x}, FOV_x = \frac{1}{\triangle kx} \tag{2.21}$$

Similar inequalities can be obtained for the image height (y-direction). The optimal spacing in the k-space is given by

$$\triangle k_x^* \leq \frac{1}{2FOV_x}, \triangle k_y^* \leq \frac{1}{2FOV_y} \tag{2.22}$$

In the frequency encode (x) direction the sampling rate is dictated by the analogue-to-digital converter (ADC) used on the receiver, boards which rarely presents aliasing problems. However, in the phase encode (y) direction the sampling rate is dictated by the magnitude of the k-space shift imposed by the phase encode gradient lobe. As each phase encoding step takes a significant amount of time it is imperative that we minimize the number of steps required to traverse a fixed extent of k-space if we are to reduce the scan time. So we obviously intend to take

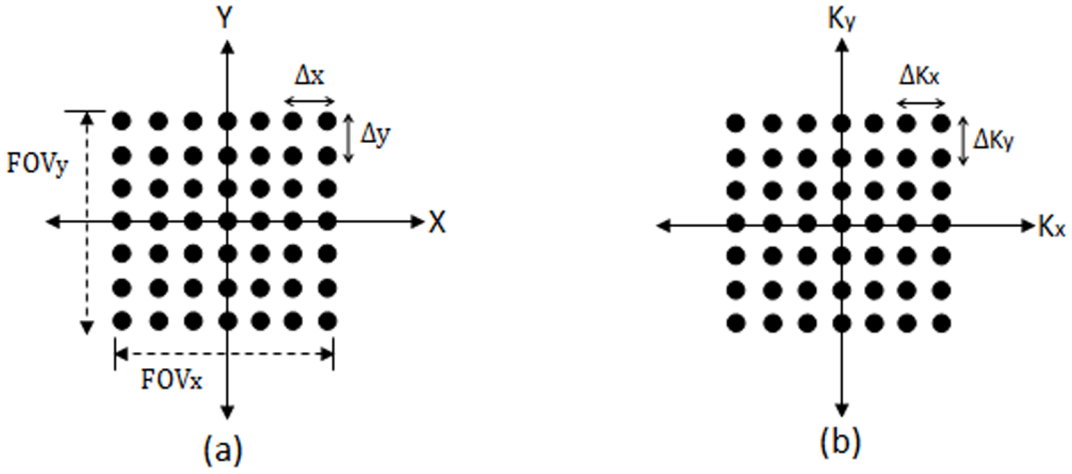

Figure 2.6: (a): Image domain; **(b):** k-space domain

as large step as possible or as small FOV as possible. However, if the FOV does not wholly contain the object then this will lead to aliasing in the object domain.

2.4 MRI Pulse Sequence

Fig. 2.7 shows a typical pulse sequence for MRI data acquisition. In the presence of uniform magnetic field B0, first z-gradient is applied which creates a linear variation in magnetic field along z direction then RF pulse is applied which flips all the atoms of a particular slice at $z = z_0$ in the transverse plane (xy plane). Following this a phase encode is applied for some time that creates phase variation along y direction. Now x-gradient is applied which creates linear variation in magnetic field in x direction, as a result all the atom precesses along x direction with different frequency. The signal is readout during the application of x-gradient and is called readout gradient of frequency encode. The whole process is repeated with different phase encoding step every time and corresponding k space locations are filled. For an image of dimension 256×256, one needs 256 phase encodes and 256 sampling points during readout.

2.5 Acceleration with Parallel Imaging

Parallel imaging [33,40] is based on the idea that the spatially varying sensitivities of individual coil elements forming a receive coil array can be used to instantaneously encode spatial information during signal reception. This simultaneous sig-

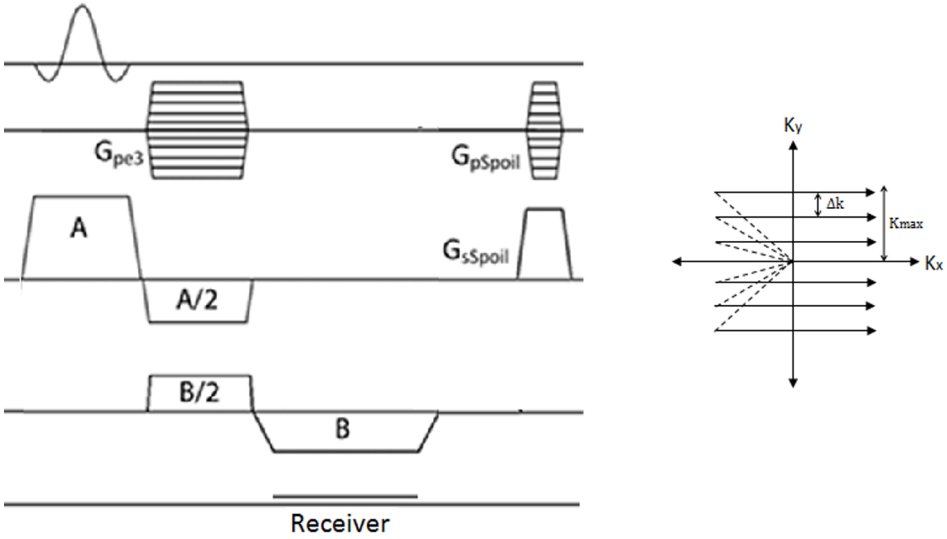

Figure 2.7: Gradient Recall Echo Pulse Sequence

nal encoding allows for the reduction of the number of necessary phase-encoding steps conventionally required for magnetic resonance imaging and thus the acceleration of scanning or the increase of spatial resolution, keeping the total scan time constant. The development of parallel imaging began with the introduction of the phased array coil concept as a suitable hardware platform to increase the signal-to-noise ratio. Multiple independent and decoupled reception coils each connected to an individual receiver allowed a local signal reception, minimizing the noise, dominated by the object itself, to the sensitive volume of the coil. Different algorithms have been used to combine the individual coil data and to compensate for the residual reception inhomogeneities. Some of these approaches already partly anticipated recent developments in parallel imaging and have, therefore, something in common with algorithms used for approaches to accelerate scanning. Parallel imaging algorithms can primarily be classified in two categories:

1. Algorithm that works in image domain such as SENSE, SPACE RIP
2. Algorithm that works in k-space domain such as SMASH, AUTOSMASH, GRAPPA.

2.5.1 SENSE

As originally presented, the Cartesian form of SENSE [21, 22] is found upon a uniform downsampling pattern. Based on the subsequent aliasing pattern that results from this subsampling choice, one can construct a small system for each

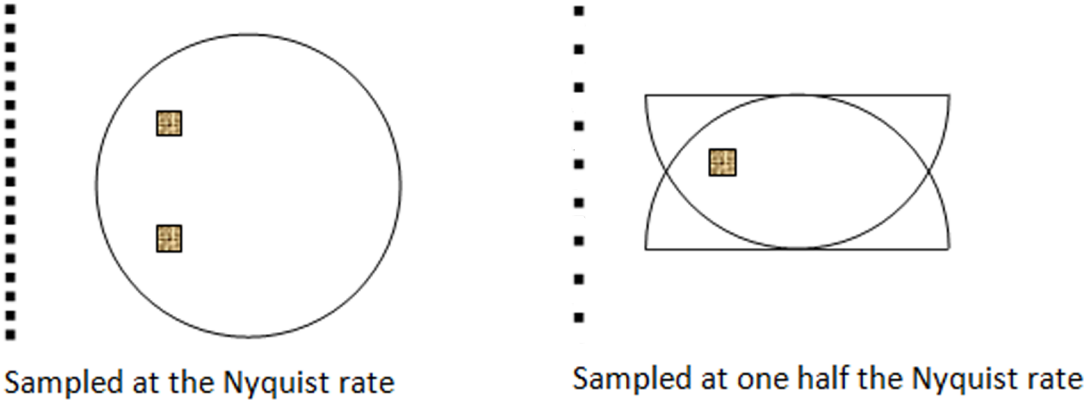

Figure 2.8: When k-space is sampled at Nyquist rate there is no aliasing in the image (left), however with the uniform down sampling by a factor of 2 in k-space results in aliasing in the image (right)

spatial-domain pixel in the acquired data reference frame. Solving this small system gives unaliased spatial-domain pixels. This process is then repeated for each pixel in the FOV. For example, consider a multiple coil acquisition employing a uniform downsampling by 2 phase-encode k-space acquisition pattern. In the spatial domain, this sampling pattern will alias a pixel (j, x) with a pixel from the alternate half of the FOV, $(j + N/2, x)$, as shown in Fig. 2.8. To reconstruct the image, SENSE estimate these two pixel values, [I(j, x), I(j + N/2, x)]. The reconstruction equation is formed using estimates of the coil sensitivity at the location of these aliased pixels.

$$v_1(j,x) = W_1(j,x)I(j,x) + W_1(j+N/2,x)I(j+N/2,x) \tag{2.23}$$

Collecting together the expressions for each coil yields the SENSE linear system of equations

$$\begin{bmatrix} v_1(j,x) \\ v_2(j,x) \\ \vdots \\ v_L(j,x) \end{bmatrix} = \begin{bmatrix} W_1(j,x) & W_1(j+N/2,x) \\ W_2(j,x) & W_2(j+N/2,x) \\ \vdots & \vdots \\ W_L(j,x) & W_L(j+N/2,x) \end{bmatrix} \times \begin{bmatrix} v_1(j,x) \\ v_2(j,x) \\ \vdots \\ v_L(j,x) \end{bmatrix}$$

which is repeated for each pixel location in the acquired spatial-domain coordinate system. Using an identical framework, this approach has also been used for variable density under-sampling patterns

2.5.2 SMASH

SMASH [20, 23, 34, 41] stands for simultaneous acquisition of spatial harmonics, is a k-space technique, in the sense that it seeks to estimate a composite k-space of the image from partial data acquired in different coils. Image reconstruction is performed by Fourier transformation of the composite k-space. SMASH operates by using linear combinations of simultaneously acquired signals from multiple surface coils with different spatial sensitivities.

First, the sensitivity profiles $W_k(x, y)$ are linearly combined to approximate composite spatial harmonics in the phase-encoded direction as follows:

$$W_m^{Comp} = \sum_{k=1}^{K} a_k^m W_k(x, y) \approx A e^{jm\triangle k_y y} \tag{2.24}$$

where $k_y = 2/\text{FOV}$, A is a complex constant, and K is the total number of coils used. This approximation tries to fit the 2-D coil-sensitivity profiles to a 1-D function in the y direction, rendering the fit challenging and error prone. Once the weights are computed, the signals can be combined to form shifted lines of the image k-space as follows:

$$s_m^{Comp} = \sum_{k=1}^{K} a_k^m . s_k(G_y^i, t) \tag{2.25}$$

$$= \sum_{k=1}^{K} a_k^m \iint I(x, y) W_k(x, y) e^{j(k_x xt + k_y y)} dxdy \tag{2.26}$$

$$= \iint I(x, y) \sum_{k=1}^{K} a_k^m W_k(x, y) e^{j(k_x xt + k_y y)} dxdy \tag{2.27}$$

Combining Equation 2.24 and Equation 2.27 results in:

$$s_m^{Comp} = \iint I(x, y) A e^{j(m\triangle K_y y)} e^{j(k_x xt + k_y y)} dxdy \tag{2.28}$$

$$= A \iint I(x, y) e^{j[k_x xt + (k_y + m\triangle k_y)y]} dxdy \tag{2.29}$$

This shows that shifted k-space lines can be synthesized using a linear combination of the same phase-encoded signals acquired in all the coils in the array. Note that the harmonic fit is approximately, but not exactly, sinusoidal leading to the problems in reconstruction. Fig. 2.9 shows the signal flow for the SMASH algorithm. Here each coil is used to collect regularly subsampled k-space sets with a

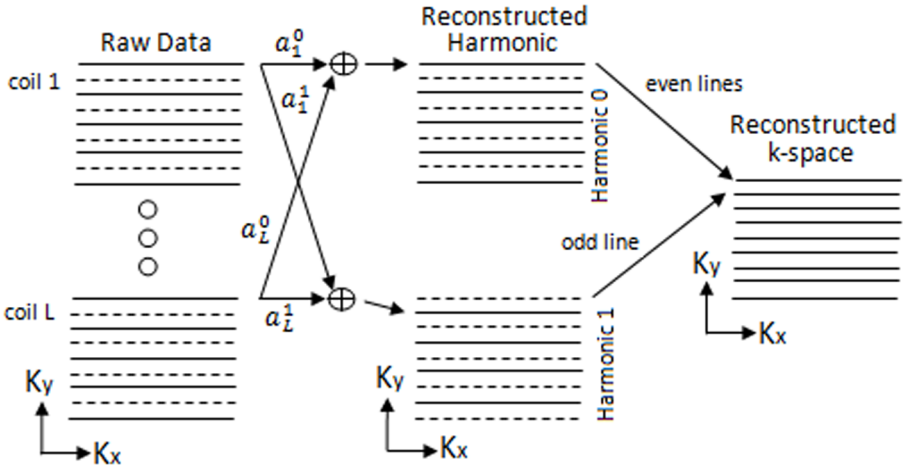

Figure 2.9: Combining data in SMASH imaging

skip factor of two. Reconstructing these sets yields aliased images, weighted by the coil sensitivity profiles. The acquired signals are combined linearly to form the harmonics as described in Equation 2.14. Reconstruction of each harmonic set separately also yields aliased images, where the coil weighting has been removed. Finally, the harmonic sets are combined into a k-space representation, filling odd lines from one harmonic and even lines from the other. Note that the chosen acceleration factor in SMASH imaging determines the number of harmonic fits needed to generate the composite k-space data.

2.5.3 AUTO-SMASH

One of the significant difficulties with implementing SMASH clinically is that the reconstruction quality is greatly dependent on the coil configuration used. Compounding this difficulty is the fact that coil sensitivities are only approximately known. Thus, more recent k-space methods have focused on bypassing the need to estimate coil-sensitivity maps. The first such approach was AUTO-SMASH [35], in which one additional line of k-space is acquired in the low-frequency region and futher improvements were made in [42]. The harmonic fit coefficients are then determined by fitting the acquired lines of k-space to this autocalibration line. Specifically, the k-space extrapolation coefficients $a_k(m)$ are determined via

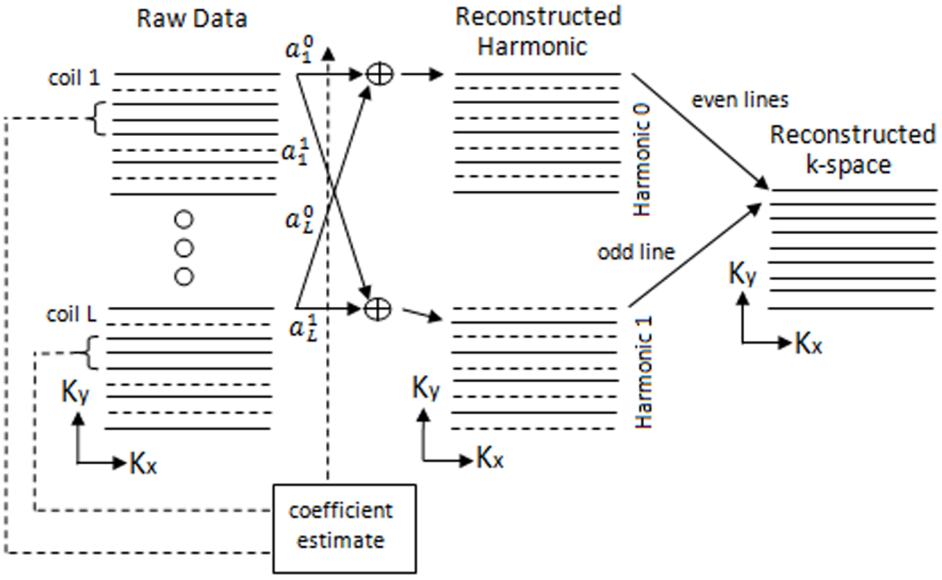

Figure 2.10: Data flow and reconstruction in AUTO-SMASH imaging

solution of a linear system of equations:

$$S^{Comp}(k_y + m\triangle k_y) = \sum_{l=1}^{L} b_l^{(m)}.S_l(k_y) \tag{2.30}$$

$$= \sum_{l=1}^{L} a_k^{(m)} S_l^{ACS}(k_y + n\triangle k_y) \tag{2.31}$$

This expression can be written in matrix form as

$$S^{Comp}(:, k_y + m\triangle k_y) = \begin{bmatrix} b_1^{(m)} & b_2^{(m)} & \dots & b_L^{(m)} \end{bmatrix} \times \begin{bmatrix} S_1(.., k_y + m\triangle k_y) \\ S_2(.., k_y + m\triangle k_y) \\ \vdots S_L(.., k_y + m\triangle k_y) \end{bmatrix} \tag{2.32}$$

where $S^{Comp}(:, k_y + m\triangle k_y)$ and $S_l(:, k_y + m\triangle k_y)$ represent vectors from the acquired k-space data set.

The reconstructed image is formed using these coefficients in the same fashion as the original SMASH reconstruction equations. A schematic describing the data flow in AUTO-SMASH is shown in Fig. 2.10

2.5.4 GRAPPA

Generalized Partial Parallel Acquisition uses coil sensitivity to estimate missing line of undersampled k-space. It generates full FOV image for each coil that are

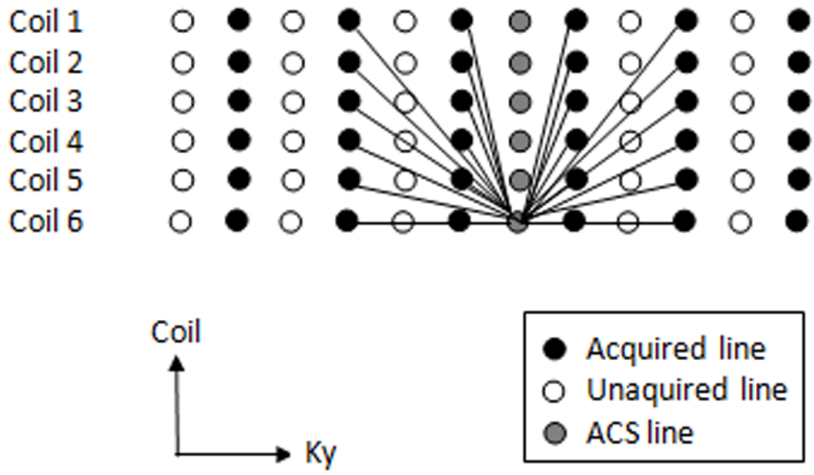

Figure 2.11: Pictorial representation of GRAPPA Algorithm

futher combined to reconstruct final image. As individual coil images are reconstructed with GRAPPA method, it result in higher SNR than the AUTO SMASH technique. In [43–47] researchers showed the improvement in the GRAPPA technique and analysis of the reconstruction quality based on G-Factor analysis. This technique is also used for dyanamic imaging for cardiac application and is extended to non cartesian trajectories in [48–54]. In GRAPPA [23], uncombined images are generated for each coil in the array by applying multiple blockwise reconstructions to generate the missing lines for each coil. This process is shown in Fig. 2.11. Again, data acquired in each coil of the array (black circles) are fit to the ACS line (gray circles). However, as can be seen, data from multiple lines from all coils are used to fit an ACS line in a single coil, in this case an ACS line from coil 4. This fit gives the weights which can then be used to generate the missing lines from that coil. Once all of the lines are reconstructed for a particular coil, a Fourier transform can be used to generate the uncombined image for that coil. Once this process is repeated for each coil of the array, the full set of uncombined images can be obtained, which can then be combined using a normal sum of squares reconstruction. In general, the process of reconstructing data in coil j at a line $(k_y - m\triangle k_y)$ offset from the normally acquired data using a blockwise reconstruction can be represented by

$$S_j(k_x, k_y + m\triangle k_y) = \sum_{l-1}^{L} \sum_{b=0}^{N_b-1} W(j, b, l, m) S_l(k_x, k_y - bR\triangle k_y) \tag{2.33}$$

where R represents the acceleration factor. N_b is the number of blocks used in the reconstruction, where a block is defined as a single acquired line and (R -1) miss-

ing lines (Fig.2.11). In this case, $n(j, b, l, m)$ represents the weights used in this now expanded linear combination. In this linear combination, the index l counts through the individual coils, while the index b counts through the individual reconstruction blocks. This process is repeated for each coil in the array, resulting in L uncombined single coil images which can then be combined using a conventional sum of squares reconstruction or any other optimal array combination.

SENSE and GRAPPA are most commonly used in practice, particularly on commercial scanner and SMASH/AUTO SMASH are rarely used now because of their limitation and poor performance.

2.6 Acceleration with Compressive Sensing

Compressive Sensing [55–58] is a technique that tries to acquire data in compressed form. In other words, CS is a technique that uses prior information about the signal to reconstruct it from the fewer number of measurements than required. In most of the applications of CS, the prior information about the signal is sparsity. If the signal is known to be sparse in certain domain such as wavelet, finite difference or DCT, then according to this newly developed theory of CS it is possible to reconstruct signal from fewer measurements than required for perfect reconstruction.

2.6.1 Compressive Sensing Theory

Compressive sensing is a mathematical theory describing how a sparse signals can be faithfully recovered after sampling projections well below the Nyquist sampling rate.

Consider a signal x in the n dimensional complex space C^n that can be sparsely represented in Ψ domain as $s = \Psi x$, where Ψ is the $n \times n$ sparsifying transform matrix. The signal s is K-sparse, that is, only the K coefficients in s are non-zero. A measurement system measures signal y in m dimensional space by taking only m projections of the signal x as

$$y = \Phi x \tag{2.34}$$

where $y \in C^m$, $K < m \ll n$ and Φ is the $m \times n$ measurement matrix. In MRI, Φ is usually a (partially) randomly under-sampled discrete Fourier transform matrix.

Equation (2.34) can be further expressed as

$$y = \Phi\Psi^* s, \quad x = \Psi^* s \tag{2.35}$$

where * represents the conjugate transpose operation and the signal x is sparse in the Ψ domain. MR images can be sparsely represented in the wavelet domain using the wavelet transform matrix. Given the measurement y and the matrices Φ and Ψ, there exist many solutions satisfying (2.34) and recovering x becomes an ill posed problem. The CS theory provides a unique solution to the ill-posed problem by solving the following optimization program:

$$\min_{\hat{x}} \quad \|\Psi\hat{x}\|_{l_1} \quad s.\,t. \quad y = \Phi\hat{x} \tag{2.36}$$

where $\|x\|_{l_1} := \sum_i |x_i|$ is the l_1 norm of x, with x_i the ith element of x. Exact reconstruction of the signal x is achievable if certain mathematical conditions hold.

2.6.2 Restricted Isometry in Compressive Sensing

An important sufficient condition for exact reconstruction of x is the so called restricted isometry property (RIP) [59–61]. For a normalized measurement matrix Φ with unit column norms, the RIP is given as

$$(1 - \delta_K)\|x\|_{l_2}^2 \leq \|\Phi x\|_{l_2}^2 \leq (1 + \delta_K)\|x\|_{l_2}^2 \tag{2.37}$$

where $\delta_K \in (0, 1)$ is called the RIP constant and l_2 norm is defined as $\|x\|_{l_2} = (\sum_i |x_i|^2)^{1/2}$. The RIP (2.37) is equivalent to [59, 62, 63]

$$(1 - \delta_K) \leq \sigma_{min}^2[\Phi_{sub}(K)] \leq \sigma_{max}^2[\Phi_{sub}(K)] \leq (1 + \delta_K), \tag{2.38}$$

where $\Phi_{sub}(K)$ is the $m \times K$ submatrix formed from K distinct columns of Φ, and $\sigma_{min}[\Phi_{sub}(K)]$ and $\sigma_{max}[\Phi_{sub}(K)]$ are the minimum and maximum singular values[1] of $\Phi_{sub}(K)$, respectively. The RIP constant δ_K is the smallest constant that satisfies the inequalities (2.38) for every $m \times K$ sized submatrix of Φ, and it is essentially a bound on the distance between unity and the singular values of all $\Phi_{sub}(K)$s. It is shown in [61] that if $\delta_{2K} < 1$, then a K-sparse signal x can be exactly reconstructed from the measurements of Φ.

[1] In [59, 62, 63], the eigenvalue $\lambda[\Phi_{sub}(K)^*\Phi_{sub}(K)]$ is used for (2.38), where $\lambda[\Phi_{sub}(K)^*\Phi_{sub}(K)] = \sigma^2[\Phi_{sub}(K)]$.

While $\delta_K \in (0, 1)$ renders the exact reconstruction of x, the value of δ_K determines the stability of reconstruction. In the presence of measurement noise ϵ, $y = \Phi x + \epsilon$ and the reconstructed signal $\hat{x}$ satisfies (Section 5.2 [64])

$$\|x - \hat{x}\|_{l_2}^2 \leq \frac{4\epsilon^2}{1 - \delta_{2K}}. \tag{2.39}$$

Thus, the smaller the δ_K, the smaller the reconstruction error, and vice versa. Since measurement noise always exists in practice, the size of δ_K is an important performance measure of a measurement matrix Φ for both the reconstruct-ability and reconstruction error. However, the computation of δ_K for a given Φ is NP hard and hence intractable. Since the RIP constant δ_K is essentially a bound on the distance between 1 and the singular values of all $\Phi_{sub}(K)$s, the size of δ_K can be assessed by the distances from 1 to the $\sigma_{min}[\Phi_{sub}(K)]$s and $\sigma_{max}[\Phi_{sub}(K)]$s. The smaller the distance, the smaller the δ_K and hence the better performance of Φ. Since (2.38) must hold for all the $m \times K$ submatrices of Φ, the statistics of $\sigma_{min}[\Phi_{sub}(K)]$ and $\sigma_{max}[\Phi_{sub}(K)]$ over randomly sampled $\Phi_{sub}(K)$'s are used in [62, 63, 65] to assess the RIP performance of a given measurement matrix Φ. This method is also adopted in this work.

2.6.3 Incoherence in Compressive Sensing

Another important sufficient condition for exact reconstruction of x is the incoherence [57, 66]. For a pair of measurement matrix Φ and sparsifying transform matrix Ψ, satisfying $\Phi^*\Phi = nI$ and $\Psi^*\Psi = I$, their incoherence is defined as

$$\mu(\Phi, \Psi) = \max_{k,j} |\langle \Phi_k, \Psi_j \rangle| \tag{2.40}$$

where Φ_k and Ψ_j are respectively the kth and jth columns of Φ and Ψ, and $\mu(\Phi, \Psi) \in [1, \sqrt{n}]$. The value $\mu(\Phi, \Psi) = 1$ is termed as maximal incoherence. As shown in [57], if $m \geq C \cdot \mu^2(\Phi, \Psi) \cdot K \cdot log(n)$, where C is a small constant, then a K-sparse signal x can be exactly reconstructed. Thus, $\mu(\Phi, \Psi)$ determines the minimum number of measurements needed for exact reconstruction of x. The smaller the $\mu(\Phi, \Psi)$, the smaller the m (the fewer the measurements) needed for exact reconstruction of x.

It is important to note that both the RIP and the incoherence are sufficient conditions on the measurement matrix. So they are parallel and either or both of them can be used to design, analyze and assess the measurement matrix for exact reconstruction of x.

2.6.4 Compressive Sensing in MRI

Accelerating the data acquisition process is an active area of research in MRI, and Compressive Sensing (CS) is a promising solution that can improve the speed of data acquisition in MRI. CS [57, 59, 65, 67, 68] is a technique that permits the faithful reconstruction of the signal of interest from the data acquired below the Nyquist sampling rate. MRI is a ideal system [69] for CS applications as it acquires image already in encoded form rather than in pixel domain. The application of CS in MRI was first described in [2], where variable density random under-sampling of phase encodes was suggested as a sampling strategy. Parallel imaging techniques [20, 21, 23] have also been combined with CS in [70–75] to further accelerate MRI scans, and CS-MRI has been applied for dynamic imaging, exploiting k-t space sparsity [73, 76–79].

The theory of CS provides a solution to an ill-posed inverse problem by exploiting prior knowledge of signal sparsity or compressibility. This theory guarantees perfect reconstruction of the signal from the under-sampled data if certain conditions are satisfied [57, 59, 60, 65, 67, 68]: (i) sparsity or compressibility of the signal in the transform domain; (ii) Restricted Isometry Property (RIP) of the measurement matrix or incoherence between the measurement and sparsifying transform matrices; and (iii) a non-linear reconstruction algorithm that promotes sparse representation of the image and enforces data consistency of reconstruction with the acquired data.

2.6.5 Sampling Scheme in CS MRI

Regular or equally spaced under-sampling in k-space results in aliasing artifact in the image domain. However, random under-sampling in k-space results in noise like artifact in the image domain instead of aliasing. Therefore, an image reconstructed with random under-sampling of k-space is almost free from aliasing artifact but contains noise like artifact in the image called incoherent artifacts. These incoherent artifacts are thus eliminated using the non-linear reconstruction in CS-MRI. Ideally in 2D MR imaging, random under-sampling in both phase encode (PE) and frequency encode (FE) direction is required to optimally use CS reconstruction. However random under-sampling in both PE and FE direction is not possible due to practical limitation of the MRI scanner. Practically, only under-sampling along PE direction is feasible in 2D MR imaging. Therefore in [69], random under-sampling in PE direction was used to acquire data. One fact that was considered while designing under-sampling pattern in [69] is that most of the

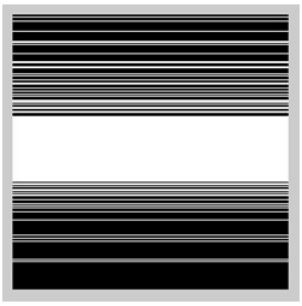

Figure 2.12: Practical random under-sampling of k-space

energy in k-space is concentrated in the centre phase encodes. Thus, in order to capture most of the energy during acquisition, a variable density under-sampling of the k-space was proposed as shown in Fig.2.12, where up-down direction is PE direction and left-right is FE direction.

2.6.6 Example of Compressive Sensing in 1D

The CS sampling and reconstruction can be understood with an intuitive example show in Fig.2.13. Consider a sparse signal (Fig. 2.13(1)) in image domain [2] and its representation in k-space Fig. 2.13(2). Equispaced under-sampling in k-space by a factor of eight and reconstruction with zero filling result in aliasing in image domain as shown in Fig.2.13(3a). This reconstruction results in inherent ambiguity and it is not possible to recover the original signal without any further knowledge about the signal. Now consider a random under-sampling of the same signal by a factor of eight in k-space. The zeros filled Fourier transform reconstruction of the randomly under-sampling k-space signal results in image domain signal as shown in Fig. 2.13(3). The random under-sampling and zero filled Fourier transform reconstruction results in original signal superimposed with additive random noise. These random noise like artifact are noise but a leakage of energy from the non zero coefficient of the signal to zero coefficient of the signal. The energy from the non zero coefficient interfere with the zero coefficient and appears as noise in the reconstructed signal. Therefore, the problem is transformed into a signal denoising problem. A simple reconstruction procedure involves thresholding and recovering strong coefficient as shown in Fig. 2.13(4-5), followed by calculation of interference due to strong coefficient (Fig. 2.13(6)) and subtracting it from the originally reconstructed signal (Fig. 2.13(4)). This procedure eliminates the interference due to strong coefficient and results in signal having smaller coefficients above the noise floor (Fig. 2.13(7)). With iterative thresholding and subtraction, smaller coefficient can be recovered and original signal can be restored.

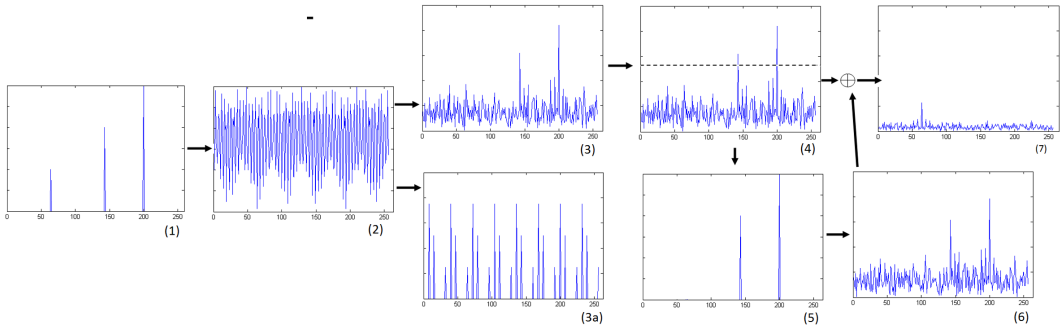

Figure 2.13: Compressive sampling and signal reconstruction

2.6.7 Application of Compressive Sensing in MRI

In Fig.2.14 [2] a brain image is represented as m, let Ψ denote the linear operator that transforms from pixel representation into a sparse representation, and let F_u be the under-sampled Fourier transform operator, corresponding to the k-space under-sampling schemes discussed in subsection 2.6.5. The partial k-space data is acquired as $y = F_u x$, direct zero filled inverse Fourier reconstruction ($\hat{m} = F_u^* y$) results in image with incoherent artifact (Fig.2.14). In order to obtain the desired image the following constrained optimization program is solved:

$$\min \quad \|\Psi \hat{m}\|_{l_1} \qquad s.t \qquad \|F_u \hat{m} - y\|_{l_2} < \epsilon$$

Here $\hat{m}$ is the reconstructed image, y is the measured k-space data from the scanner, and ϵ controls the fidelity of the reconstruction to the measured data. The threshold parameter ϵ is set below the expected noise level. The first term in above reconstruction program essentially minimizes the the sparse representation (wavelet) of the desired image and the second term enforces the consistency with the acquired data.

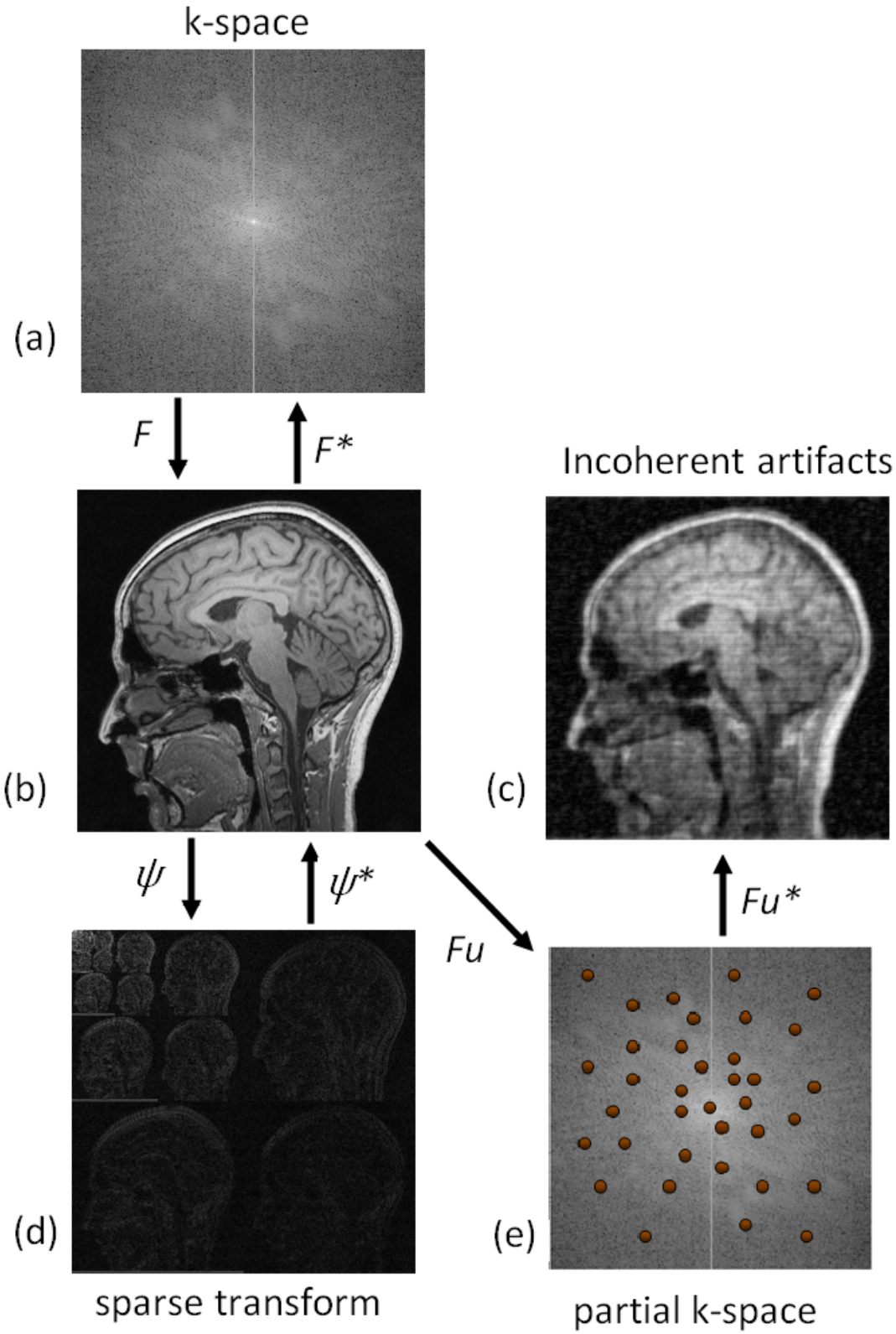

Figure 2.14: Application of Compressive Sensing in MRI [2]. (a) is acquired k-space of the image, (b) is image reconstructed after taking 2D FFT of the k-space, (d) is sparse representation of the image after taking 2D wavelet transform of the image, (e) represents a partial k-space, here the red dots represent the sampled points in k-space and (c) represents the image reconstructed after taking 2D FFT of the partial k-space. The image shown in (c) looks similar to the original image (b) but have some incoherent artifacts, these noise like incoherent artifacts are removed by applying the compressive sensing reconstruction algorithm.

Chapter 3

Multichannel Compressive Sensing MRI Using Noiselet Encoding

3.1 Introduction

The structural imaging applications such as 3D MRI can always benefit from the accelerated imaging. The scan time reduction in static imaging can reduce the patient discomfort, increase the throughput thereby reducing the cost incurred per person and can reduce the imaging artifact due to patients motion. Therefore in order to accelerate static imaging, in this chapter we present a method to accelerate structural MRI scans. The approach we have used to accelerate static MRI is a mutichannel compressive sensing framework.

Compressive Sensing (CS) is a promising technique that can improve the speed of data acquisition in MRI. CS [59, 65, 67, 68, 80] is a technique that permits the faithful reconstruction of the signal of interest from the data acquired below the Nyquist sampling rate. MRI is a ideal system [69] for CS applications as it acquires image already in encoded form rather than in pixel domain. The application of CS in MRI was first described in [2], where variable density random under-sampling of phase encodes was suggested as a sampling strategy. Parallel imaging techniques [21, 23, 35] have also been combined with CS in [70–75] to further accelerate MRI scans, and CS-MRI has been applied to dynamic imaging, exploiting k-t space sparsity [73, 76–79].

The theory of CS provides a solution to an ill-posed inverse problem by exploiting prior knowledge of signal sparsity or compressibility. This theory guarantees

perfect reconstruction of the signal from the under-sampled data if certain conditions are satisfied [59,60,65,67,68,80]: (i) sparsity or compressibility of the signal in the transform domain; (ii) Restricted Isometry Property (RIP) of the measurement matrix or incoherence between the measurement and sparsifying transform matrices; and (iii) a non-linear reconstruction algorithm that promotes sparse representation of the image and enforces data consistency of reconstruction with the acquired data.

The sparsity or compressibility condition is satisfied by MR images as they are known to be sparse or compressible in the wavelet domain and the finite difference domain [2, 70–72]. However, the RIP is difficult to verify for a given deterministic measurement matrix since it is computationally NP (Non-deterministic Polynomial-time) hard [81]. An empirical solution to this problem in the CS literature is to use random measurement matrices. A randomly sampled frequency domain data can capture pertinent information from a sparse signal with fewer measurements and allows accurate reconstruction of the signal by the convex l_1 optimization program. This property was first proved mathematically for Gaussian matrices [61, 65] and has recently been extended to a wide class of random matrices [82]. Based on this property, [83] proposed using spatially selective RF pulses to implement random encoding along the phase encode direction, with the entries of the random measurement matrix drawn from Gaussian distribution. This random encoding scheme attempts to approximate the sufficient conditions for perfect CS reconstruction, but as described in [83], this measurement matrix is not unitary and results in noise amplification even after taking all the required measurements. Another problem with random encoding is computational complexity. Dense random matrices consume large amounts of memory and require computationally expensive matrix multiplications in CS-reconstruction [80, 84]. This problem is partially alleviated in [83] by using fast Fourier transforms of the matrix multiplications, but still requires more memory and computations than those of structured/unitary measurement matrices.

MRI uses the Fourier basis to encode the excited region of interest. The Fourier measurement matrix is weakly incoherent with the wavelet sparsifying transform matrix, thus is sub-optimal for CS-MRI [85]. The incoherence is essentially a measure of the spread of sparse signal energy in the measurement domain [80]. Various attempts have been made in [83,85–88] to spread the energy of the MR signal in the measurement domain. In [85, 89], the spread spectrum technique was presented which convolves the k-space with the Fourier transform of a chirp function to spread the energy of the MR signal in the measurement domain. The chirp modu-

lation is implemented through the use of second order shim coils. In [86–88,90–92], other non-Fourier encoding strategies were described for compressive sensing that aims to spread the energy of the MR signal in the measurement domain. While these encoding strategies can spread the signal energy to some extent, none of them has the theoretically proven maximal incoherence for the complete spread of the signal energy.

Noiselet bases [66, 93] are known to completely spread out the energy of the signal in the measurement domain, which is a desired property in CS. Noiselets are also known to be maximally incoherent with Haar wavelets that makes them the best suited bases for CS. Further, noiselet matrices are complex valued, symmetric and unitary, which simplifies the implementation of image reconstruction program in CS-MRI. In the simulation study of [94], it is found that the noiselet measurement matrix outperforms the chirp modulation measurement matrix when the noise level is high. Also, as shown in Section 3.3.5 of this chapter, the multichannel noiselet measurement matrix exhibits much better RIP than that of its Fourier counterpart. In order to take the advantage of maximal incoherence and better RIP provided by noiselet measurement matrix, we have investigated the use of noiselet encoding for CS-MRI.

In order to take the advantage of multiple measurements provided by an MR scanner through the use of multiple channels, a Multichannel Compressive Sensing (MCS) framework is proposed in [70] for CS reconstructions. The MCS framework simultaneously uses data from the multiple channels to reconstruct the desired image instead of reconstructing separate images from each channel, resulting in higher acceleration factors and improved image quality. Therefore, in this work we describe the theory and implementation details of using noiselet bases as the measurement matrix in MCS-MRI. Considering the lack of analysis and sufficient understanding of MCS-MRI in the literature, we also present an empirical RIP analysis of the multichannel noiselet measurement matrix in comparison with its Fourier counterpart. The results indicate that the multichannel noiselet measurement matrix outperforms its Fourier counterpart, and that noiselet encoding outperforms Fourier encoding in preserving image resolution for the same acceleration factors, and can achieve higher acceleration factors than the Fourier encoding scheme for the desired image quality and resolution.

This chapter is organized as follows. In section 3.2, we describe the background of CS, sufficient conditions for CS and develops a model for MCS-MRI reconstruction. In section 3.3, we describe the noiselet basis function, its properties and our motivation for using noiselets in MRI. A pulse sequence design to implement the

proposed noiselet encoding scheme is also described in this section, followed by an empirical RIP analysis of the multichannel noiselet measurement matrix in comparison with its Fourier counterpart. In section 3.4, simulation studies comparing the performance of noiselet encoded and Fourier encoded MCS-MRI for different acceleration factors are demonstrated on a brain image. The effect of the number of channels and level of noise on the reconstruction is also evaluated for both the encoding schemes. In section 3.5, we demonstrate the feasibility of the proposed encoding scheme by acquiring noiselet encoded data from a phantom and a human brain. Retrospective under-sampling is performed on the acquired noiselet encoded and the Fourier encoded data to simulate accelerated acquisition. The nonlinear conjugate method [69] with wavelet and total variation (TV) penalties is used to solve the minimization program for MCS-MRI. In section 3.6, we discuss the findings, limitation and further extension of the technique.

3.2 Multichannel Compressive Sensing

In section 2.6, the theory of compressive sensing and associated mathematical properties were described in detail. Since MRI acquire multiple measurements of the desired signal through use multiple channels, thus it make sense to use all the data together. Therefore, in this section we develop a mathematical model for multichannel compressive sensing.

Given the multiple channels, the data acquisition process can be modeled as $y_i = \Phi\Gamma_i x = \Phi\Gamma_i\Psi^* s, i = 1, 2, \cdots, L$, where $\Gamma_i = diag[\gamma_{ij}]_{j=1,2,\cdots,n}$ is the complex valued sensitivity map matrix of the ith receive channel, with γ_{ij} being the sensitivity of the ith channel at the jth pixel of the vectorized image, L is the number of receive channels, y_i is the data acquired from the ith receive coil and $s = \Psi x$. In matrix form, the y_i's can be written as

$$Y := \begin{bmatrix} y_1 \\ y_2 \\ \vdots \\ y_L \end{bmatrix} = \begin{bmatrix} \Phi\Gamma_1 \\ \Phi\Gamma_2 \\ \vdots \\ \Phi\Gamma_L \end{bmatrix} x =: Ex = E\Psi^* s. \tag{3.1}$$

As seen from above, with L receive channels, the measurement matrix for x becomes E, which has a column of L measurement matrices $\Phi\Gamma_i$'s and dimension $Lm \times n$. It is important to note that Γ_is are complex valued and $\Gamma_i \neq \Gamma_j, i \neq j$, in general. Hence, $\Phi\Gamma_i \neq \Phi\Gamma_j$ for $i \neq j$ and they can be independent of each

other, depending on the specific values of Γ_i and Γ_j. As a result, the multichannel measurement matrix E provides more independent measurements than that of the single channel Φ, which may reduce the number of measurements, m, needed at each channel for exact reconstruction of x. This reasoning is confirmed by the empirical analysis of E in Section 3.3.5.

In light of the above discussion, the following MCS optimization is considered for reconstructing the desired image x from the multichannel measurements of MRI.

$$\min_{\hat{x}} \quad \|\Psi\hat{x}\|_{l_1} \quad s.t. \quad \|Y - E\hat{x}\|_{l_2} \leq \epsilon \tag{3.2}$$

where Ψ is the wavelet transform operator and ϵ determines the allowed noise level in the reconstructed image. The l_n norm is defined as $\|x\|_{l_n} = (\sum_i |x_i|^n)^{1/n}$

MR images are also known to be sparse in the total variation (TV) domain. It is demonstrated in [95] that the TV penalty is critical to the performance of CS-MRI, and that MR images can be recovered more efficiently with the use of TV penalty together with the wavelet penalty. Therefore, most of the CS-MRI work [2, 69, 71, 72, 83, 86, 88, 91, 92] has used both TV and wavelet penalties for better reconstruction performance. To be consistent with this common practice in CS-MRI, the TV penalty is included in the objective function (3.2) for MCS-MRI reconstruction, together with the wavelet penalty. Equation (3.2) is a constrained optimization problem which is computationally intensive to solve. To relax the problem, (3.2) is converted to the unconstrained optimization problem with the inclusion of TV penalty.

$$\min_{\hat{x}} \quad \lambda_1\|\Psi\hat{x}\|_{l_1} + \lambda_2\|TV\hat{x}\|_{l_1} + \|Y - E\hat{x}\|_{l_2}^2 \tag{3.3}$$

where TV is a 2D total variation operator and λ_1, λ_2 are regularization parameters for wavelet and TV penalties, respectively. The 2D TV is defined as $TV(x) = \sum_{i,j}(|x_{i+1,j} - x_{i,j}| + |x_{i,j+1} - x_{i,j}|)$

Daubechies-4 (db-4) wavelet is usually used in CS-MRI because of its superior performance in sparsifying the MR images. To be consistent with this fact and fair in comparison with the existing CS-MRI results, the unconstrained objective function (3.3) with the Ψ of the db-4 wavelet operator will be used throughout all the simulations and reconstructions in this work.

3.3 Noiselet Encoding in CS-MRI

3.3.1 Noiselets

Noiselets are functions which are noise-like in the sense that they are totally incompressible by orthogonal wavelet packet methods [66, 93]. Noiselet basis functions are constructed similar to the wavelet basis functions, through a multi-scale iteration of the mother bases function but with a twist. As wavelets are constructed by translates and dilates of the mother wavelet function, noiselets are constructed by twisting the translates and dilates [80]. The mother bases function $\chi(x)$ can be defined as

$$\chi(x) = \begin{cases} 1 & x \in [0,1) \\ 0 & \text{otherwise} \end{cases}$$

The family of noiselet basis functions are generated in the interval $[0, 1)$ as

$$\begin{aligned} f_1(x) &= \chi(x) \\ f_{2n}(x) &= (1-i)f_n(2x) + (1+i)f_n(2x-1) \\ f_{2n+1}(x) &= (1+i)f_n(2x) + (1-i)f_n(2x-1) \end{aligned} \tag{3.4}$$

where $i = \sqrt{-1}$ and $f_{2^n}, \ldots\ldots, f_{2^n+1}$ form the unitary basis for the vector space V_n. An example of a 4×4 noiselet transform matrix is given below.

$$\frac{1}{2}\begin{bmatrix} 0-1i & 1+0i & 1-0i & 0+1i \\ 1+0i & 0+1i & 0-1i & 1-0i \\ 1-0i & 0-1i & 0+1i & 1+0i \\ 0+1i & 1-0i & 1+0i & 0-1i \end{bmatrix} \tag{3.5}$$

Fig.3.1 shows real, imaginary and absolute part of the first basis of a 16 point noiselets. The real and imaginary part consist of only three values -1,0,1 and absolute part is always 1. This makes noiselets easy implement as it consist of only three values compared to random encoding where the basis are made up of random values.

Noiselets totally spread out the signal energy in the measurement domain and are known to be maximally incoherent with the Haar wavelet. The mutual incoherence parameter between the noiselet measurement matrix Φ and the sparsifying Haar wavelet transform matrix Ψ has been shown to be equal to 1 [80], which is the minimum value possible for the incoherence. Therefore, theoretically, noiselets are the best suited measurement basis function for CS-MRI when the wavelet is

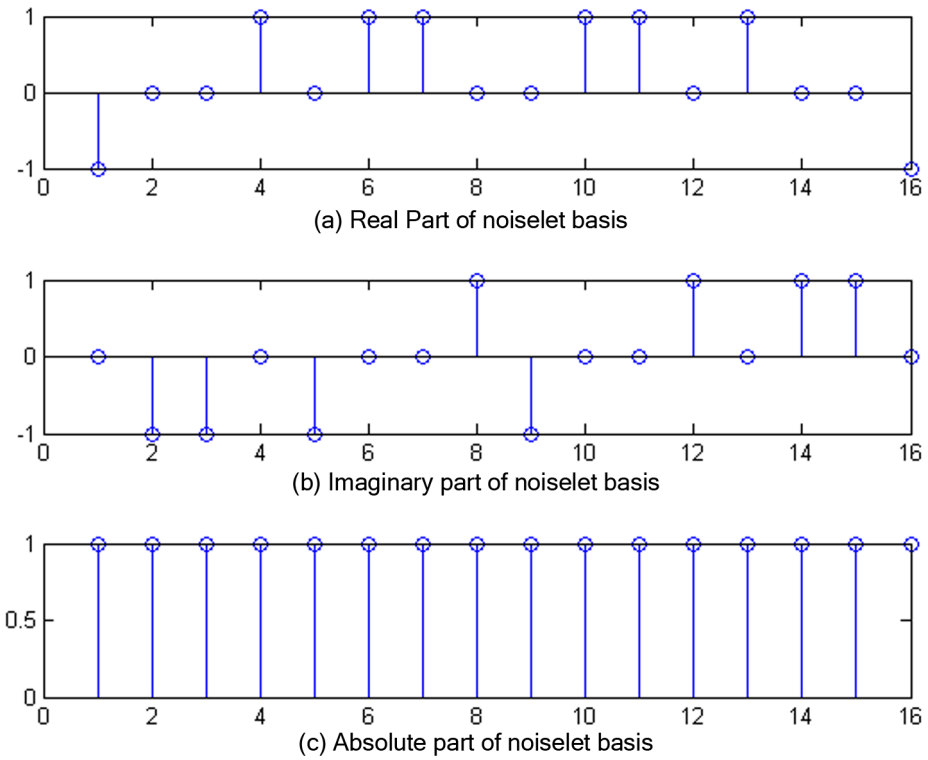

Figure 3.1: (a): Real part of noiselet basis; **(b):** Imaginary part of noiselet basis **(c):** solute part of noiselet basis. The real and imaginary part consist of only three values -1,0,1 and absolute part is always 1. This makes noiselets easy implement as it consist of only three values compared to random encoding where the basis are made up of random values.

used as sparsifying transform matrix.

3.3.2 Motivation

The motivations behind using noiselets as a measurement matrix in MCS-MRI are as follows:

- Noiselet basis function is unitary and hence does not amplify noise as in the case of random encoding [83].
- Noiselets completely spreads out the signal energy in the measurement domain and are maximally incoherent with wavelets.
- Unlike random basis, noiselet basis has conjugate symmetry. Thus, this property of symmetry can be exploited by using the partial Fourier like technique.
- Noiselets are derived in the same way as wavelets, therefore it can be modelled as a multi-scale filter-bank and can be applied in $O(n \cdot log(n))$.

We proposed to use the noiselet encoding in the phase encode (PE) direction in 2D and 3D MR imaging. Therefore, the acquired data is noiselet encoded in the PE direction and Fourier encoded in the frequency encode (FE) direction/s.

3.3.3 Pulse Sequence Design for Noiselet Encoding

In conventional 2D MR imaging sequences, a spatially selective RF excitation pulse is used to select the slice and the linear spatial gradients are used to encode the excited slice onto the Fourier transform space. In [89, 90, 96, 97], it is demonstrated that the spatially selective RF excitation pulse can also be used to encode the imaging volume. In [83, 90, 98, 99], the wavelet, SVD and random encoding profiles have been implemented using the spatially selective RF excitation pulses. An analysis using the linear response model described in [96] provides a theoretical framework to design spatially selective RF excitation pulses for implementation of non-Fourier encoding. Under the small flip angle ($\leq 30^\circ$) regime, the RF pulse envelope can be calculated directly by taking the Fourier transform of the desired excitation profile. However this method of designing an RF excitation pulse requires excellent RF and main field homogeneity.

To excite a noiselet profile during excitation, one can design an RF pulse envelope by directly taking the Fourier transform of the noiselet basis functions. For an image of size 256×256, the noiselet measurement matrix has 256 rows and 256 columns (see (3.5) for the low dimensional example). The Fourier transformation of each row of the noiselet matrix will result in 256 RF excitation pulses.

A pulse sequence for the noiselet encoding of 2D MR imaging is shown in Fig. 3.2 (a). The pulse sequence is designed by tailoring the spin echo sequence. The RF excitation pulse in the conventional spin echo sequence is replaced by the noiselet RF pulse, and the slice select gradient is shifted to phase encoding axis. The 180° refocusing RF pulse is used in conjunction with the slice selection gradient to select the slice that refocuses the spins only in the desired slice. Spoilers are used after the readout gradient to remove any residual signal in the transverse plane. A new RF excitation pulse is used for every new TR to excite a new noiselet profile, and a total of 256 TR are required for excitation of the complete set of noiselet bases. The readout gradient strength determines the FOV in the readout direction, while the phase encoding gradient strength and duration of the RF excitation pulse determines the field of view (FOV) in phase encoding direction.

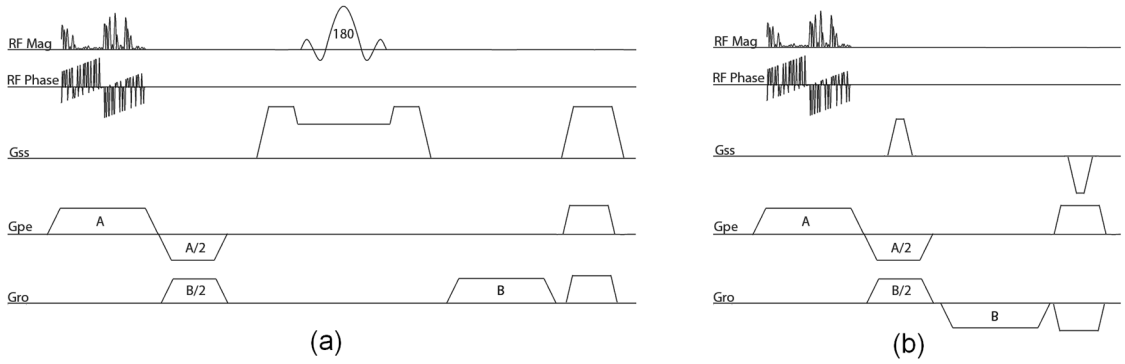

Figure 3.2: (a): Pulse sequence diagram for implementation of noiselet encoding in 2D imaging, where G_{ss} is the gradient in slice (z) direction, G_{pe} is the gradient in phase encoding (y) direction, and G_{ro} is the gradient in readout (x) direction. The RF pulse duration is 5.12 ms and the flip angle is 10°, which excites a noiselet profile along y-direction. The 180° refocusing pulse is used to select the desired slice in z-direction. A new RF pulse is executed for every new TR and the complete acquisition of all noiselet basis functions requires 256 different RF pulses derived from the noiselet measurement matrix. **(b):** Pulse sequence diagram for implementation of noiselet encoding in 3D imaging. The RF pulse excites a noiselet profile along y-direction and gradient blips are used along slice encode direction to encode slice direction with Fourier bases.

The FOV in phase encoding direction is determined as

$$FOV_{pe} = \frac{1}{\gamma G_y \Delta t_p} \tag{3.6}$$

where G_y is the gradient strength in PE direction, γ is the gyromagnetic ratio, and Δt_p is the dwell time of the RF pulse which is defined as Δt_p = (Duration of RF pulse) / (Number of points in RF pulse). Equation (3.6) is used to calculate the gradient strength G_y required in the phase encoding direction during execution of RF excitation pulse.

The method described above can also be used to design the pulse sequence for the noiselet encoding of 3D MR imaging as shown in Fig. 3.2 (b).

3.3.4 Under-sampling in noiselet encoding

Noiselet transform is a type of Haar-Walsh transform. The noiselet transform coefficients totally spread out the signal in scale and time (or spatial location) [93]. As a result, each subset of the transform coefficients contains a certain information of the original signal at all the scales and times (spatial locations), and can be used alone with zero padding to reconstruct the original signal at a lower resolution. This important property is demonstrated by the example shown in Fig. 3.3.

Fig. 3.3 shows a brain image of size 256 × 256, and the 3D magnitude map of the noiselet transform of the brain image along the phase encoding direction

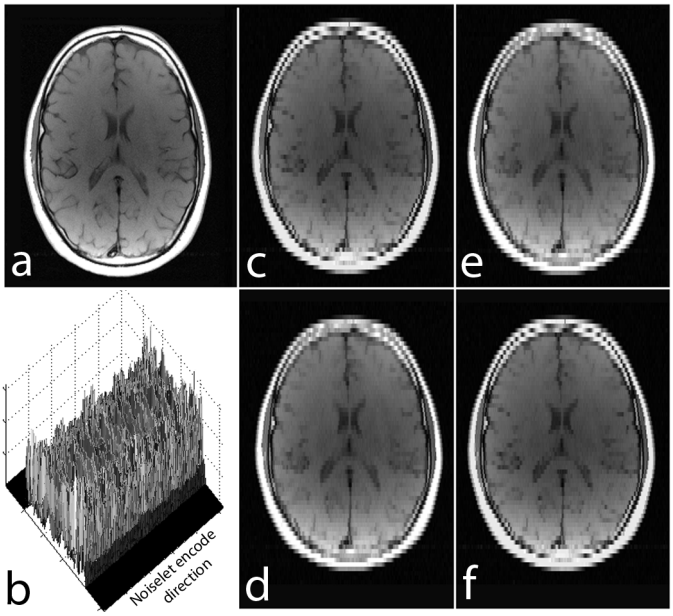

Figure 3.3: (a): Brain image of size 256×256; **(b):** 3D magnitude map of the noiselet transform of the brain image along phase encoding direction (noiselet encodes); **(c):** image reconstructed using only the first 64 noiselet encodes; **(d), (e) and (f):** are the images reconstructed with the second, third and fourth 64 noiselet encodes respectively.

(all noiselet encodes). Fig. 3.3 (c-f) shows the images reconstructed with the first, second, third and fourth 64 noiselet encodes by zero padding the rest. Each of these images are reconstructed using one quarter of the noiselet encodes and has low resolution than the original image. However, each of these images have complementary information about the original image and have approximately the same amount of energy and information because they are reconstructed using the same size of partial matrix from the original coefficient matrix.

Based on the above property of noiselet transform, we propose to under-sample the noiselet encoded data along the phase encoding direction according to the uniform probability distribution function. One sampling mask using this scheme is shown in Fig. 3.4(a) where the white lines represent the sampled data points and the black lines represent the unsampled data points. Fig. 3.4(b) shows the sampling mask for Fourier encoding scheme drawn from a variable density probability distribution function shown in Fig. 3.4(c).

3.3.5 Empirical RIP analysis of measurement matrix

According to the CS theory summarized in Section 3.2, the measurement matrix is crucial to the performance of CS reconstruction, and the performance of a measurement matrix Φ for a K-sparse signal x can be assessed by the statistics

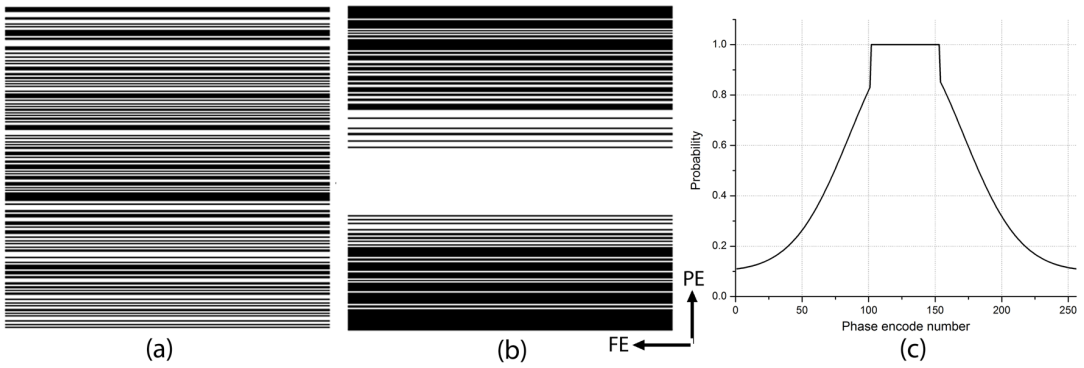

Figure 3.4: (a): Completely random sampling pattern for noiselet encoding generated using the uniform probability distribution function, where the white lines represent the sampled phase encodes; **(b):** variable density random under-sampling pattern for the Fourier encoding scheme, with the sampling mask generated according to Gaussian probability distribution function; and **(c):** probability distribution function used to generate variable density random undersampling pattern where the probability of sampling the center phase encodes is equal to 1, while the probability decays as a Guassian function with distance from the center phase encodes. The central fully sampled region is always between 20%-25% of the total number of sampled phase encodes.

of $\sigma_{min}[\Phi_{sub}(K)]$ and $\sigma_{max}[\Phi_{sub}(K)]$ over the $\Phi_{sub}(K)$s consisting of k distinct columns of Φ. To understand the behavior and advantage of the noiselet encoding proposed above, we have used this method to assess the noiselet measurement matrix in comparison to the conventional Fourier measurement matrix.

In the assessment, the size of the signal was $n = 256$, the number of measurements $m = 100$, the number of channels $L = 1, 8$ and 14, and the sparsity K was varied from 5 to 100 with an increment of 5. For $L = 1$, the measurement matrices, Φs, were generated for the noiselet and Fourier encodings, respectively. For $L = 8$ and 14, the measurement matrices Es as given in (3.1) were generated for the noiselet and Fourier encodings, respectively. For each K, 2,000 submatrices $\Phi_{sub}(K)$s were drawn uniformly randomly from the columns of Φ, then the $\sigma_{min}[\Phi_{sub}(K)]$ and $\sigma_{max}[\Phi_{sub}(K)]$ of every $\Phi_{sub}(K)$ were calculated. The same procedure is used to obtain the submatrices $E_{sub}(K)$s from E and to calculate the $\sigma_{min}[E_{sub}(K)]$ and $\sigma_{max}[E_{sub}(K)]$ of every $E_{sub}(K)$. The statistics of $\sigma_{min}[\Phi_{sub}(K)]$s, $\sigma_{max}[\Phi_{sub}(K)]$s, $\sigma_{min}[E_{sub}(K)]$s and $\sigma_{max}[E_{sub}(K)]$s were accumulated from their respective 2,000 samples.

Fig. 3.5 shows the means and standard deviations of the minimum and maximum singular values of $\Phi_{sub}(K)$s and $E_{sub}(K)$s versus the sparsity K for the Fourier and noiselet measurement matrices. As seen from the figure, in single channel case, the singular values of noiselet measurement matrix are closer to 1 than those of Fourier measurement matrix, but are not significantly different. As

the number of channels increases, the singular values of noiselet and Fourier measurement matrices all move towards 1, but those of noiselet measurement matrix move much closer to 1 than those of Fourier measurement matrix. By the CS theory, when the maximum distance from 1 to the singular values is less than 1, it equals roughly the RIP constant δ_K [61]. Therefore, the figure actually reveals two facts: 1) For both the noiselet and Fourier measurement matrices, the RIP constant δ_K decreases as the number of channels increases. 2) As the number of channels increases, the RIP constant δ_K of noiselet measurement matrix deceases much more than that of Fourier measurement matrix. According to the CS theory, these imply that the multichannel measurement matrix should generally outperform the single channel measurement matrix, and that the multichannel noiselet measurement matrix should generally outperform the multichannel Fourier measurement matrix.

As a particular example consider the curves in Fig. 3.5 (d) for the noiselet measurement matrix. To facilitate discussion, the distances from 1 to the singular values of a measurement matrix will be called the δ-distances here. In single channel case, the δ-distances of noiselet measurement matrix are less than 1 for $K \leq 40$. By RIP, this implies that the single channel noiselet measurement matrix can guarantee the recovery of the signals with sparsity $K \leq 20$. When the number of channels is increased to 14, the δ-distances are less than 1 for $K \leq 85$. So the 14 channel noiselet measurement matrix can guarantee the recovery of the signals with sparsity $K \leq 42$. The improvement in terms of sparsity is two folds. In contrast, for the 14 channel Fourier measurement matrix shown in Fig. 3.5 (c), its δ-distances are less than 1 only for $K < 30$, so it can only guarantee the recovery of the signals with sparsity $K < 15$.

From the above assessment, it can be expected that the multichannel CS MRI will outperform the single channel CS MRI and that the noiselet encoding multichannel CS MRI will outperform the Fourier encoding multichannel CS MRI in practice. These are confirmed by the simulation and experiment results presented in the next sections.

It is important to note that the above empirical analysis results are obtained by using the complex valued sensitivity maps. If only the magnitudes of the sensitivity maps are used, the above results will not hold. Therefore, the complex valued sensitivity maps of multiple receive coils are the source for the significant performance improvement of the multichannel measurement matrix.

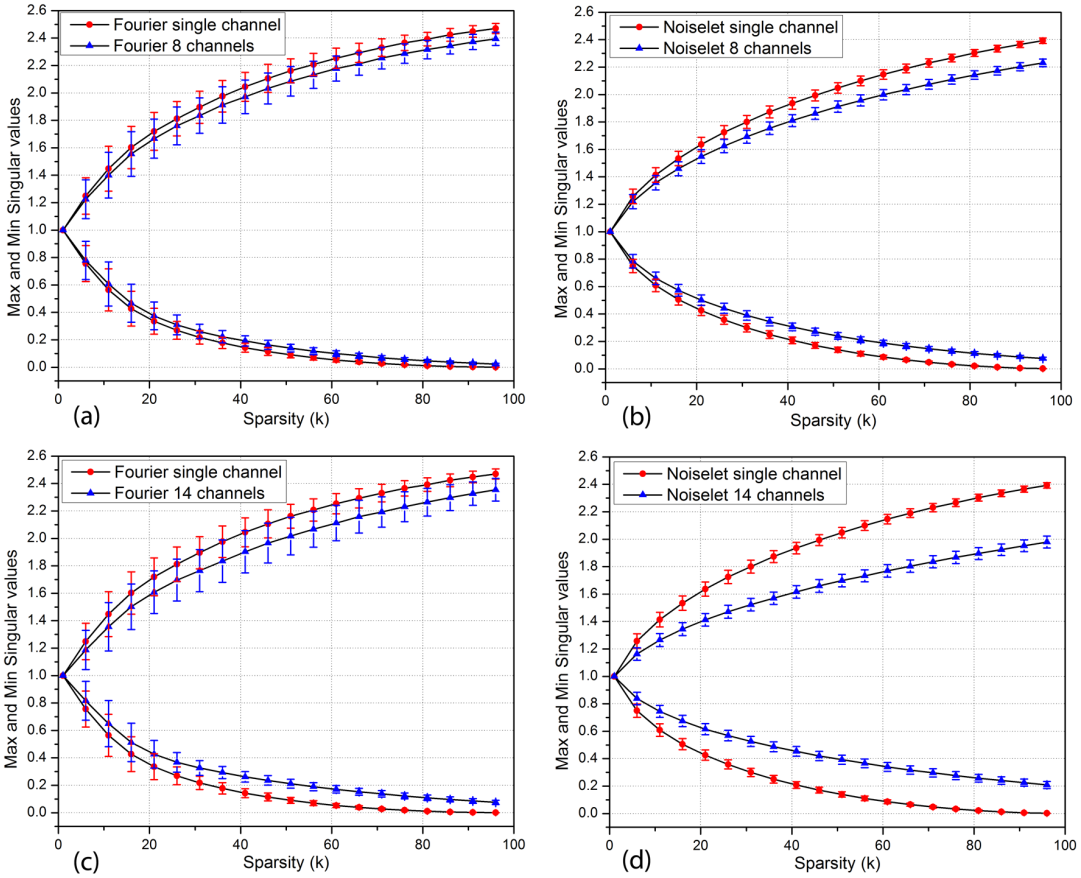

Figure 3.5: The means and standard deviations of maximum and minimum singular values versus sparsity K for **(a)** and **(c):** Fourier measurement matrix, **(b)** and **(d):** noiselet measurement matrix. The distance (δ_k) of singular values from unity determines the RIP of the measurement matrix. Smaller the value of δ_k better the RIP of the measurement matrix. It is evident from this figure that for all the cases the RIP for noiselet measurement matrix is better than that of Fourier measurement matrix. Moreover it can also be observed that as the number of receiver channel increases, the RIP for noiselet measurement matrix improves more that that of Fourier measurement matrix.

3.4 Simulation Study and Results

Simulations were performed on a (256×256) brain image to investigate the performance of noiselet encoded and Fourier encoded MRI. The simulation study was divided into two parts: (i) a simulation study with a single channel using uniform sensitivity and (ii) a simulation study with multiple channels where the sensitivity profiles were estimated from the acquired data.

3.4.1 Single Channel Simulation with a Uniform Sensitivity Profile

Fourier encoded CS-MRI A Fourier transform of the image was taken in the PE direction to simulate Fourier encoding. Two types of sampling strategies were used to sample Fourier encoded data: (i) a variable density random sampling pattern as shown in Fig. 3.4 (b) where samples were taken in the PE direction according to a Gaussian distribution function, and (ii) a completely random sampling pattern as shown in Fig. 3.4 (a) where samples were taken in the PE direction according to the uniform density function. The non-linear program of (3.3) was solved to reconstruct the final image for acceleration factors of 2 and 3. In these cases the encoding matrix E does not have any sensitivity information (i.e. $E = \Phi$).

Noiselet encoded CS-MRI A noiselet transform of the image was taken in the PE direction to simulate noiselet encoding. A completely random sampling pattern was used to sample the noiselet encoded data in the PE direction and the non-linear program of (3.3) was solved to reconstruct the final image for acceleration factors of 2 and 3. In these cases the encoding matrix E does not have any sensitivity information (i.e. $E = \Phi$).

Fig. 3.6 show the images reconstructed with Fourier encoding and noiselet encoding using variable density random under-sampling and completely random under-sampling pattern respectively. The noiselet encoded CS-MRI performs similar to that of the Fourier encoded CS-MRI. This is due to the fact that in the case of variable density random under-sampling, the Fourier encoding judiciously exploits extra information about the data, namely the structure of k-space. The center of the k-space data has maximum energy and hence, by densely sampling the center of k-space, the Fourier encoding captures most of the signal energy and results in better performance.

In practice, the MR data is collected through the use of multiple channels, and data in each channel is slightly different from the other channels. The actual k-space data is convolved with the Fourier transform of the sensitivity profiles of the individual channel, making the data from each channel different from others. This sensitivity information can also be taken into consideration while performing the CS reconstruction, by applying the multichannel CS frame. Therefore, to further study the effect of sensitivity information on noiselet encoding and Fourier encoding, MCS-MRI simulations were performed. To quantitatively compare the performance of both the encoding schemes, we used the relative error defined in

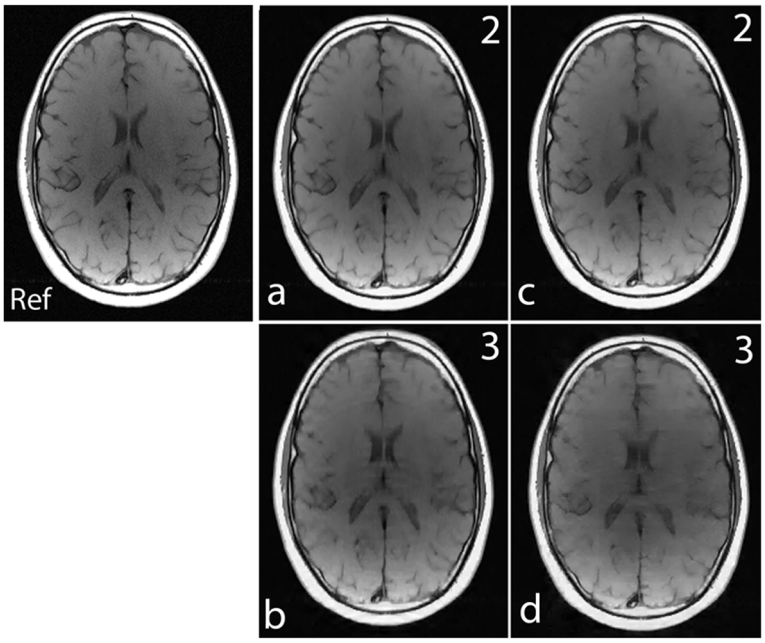

Figure 3.6: Ref: represents the reference image 256×256 (up/down: phase encodes, left/right: frequency encode); **(a)-(b):** show images reconstructed using Fourier encoding with variable density random under-sampling patterns for acceleration factors of 2 and 3 respectively; **(c)-(d):** show images reconstructed using noiselet encoding with completely random under-sampling patterns for acceleration factors of 2 and 3 respectively. Noiselet encoded CS-MRI performs better than the Fourier encoded CS-MRI when completely random under-sampling is used for both the encoding schemes. This is due to the better incoherence provided by the noiselets. However, noiselet encoding with a random under-sampling pattern performs similar to Fourier encoding with a variable density random under-sampling pattern.

(3.7) as a metric:

$$Relative\ error = \frac{\|x_0 - \hat{x}\|_{l_2}}{\|x_0\|_{l_2}} \tag{3.7}$$

First we investigated the effect of the number of channels on the reconstruction quality using the MCS framework. For a fixed number of measurements, the number of channels was varied and the mean of the relative error for 1000 such simulations was calculated. Fig. 3.7 shows the plot of the mean relative error versus the number of channels for the acceleration factors of 2 and 3. When the number of channels was two, the noiselet encoding scheme outperformed the Fourier encoding scheme for both the acceleration factors of 2 and 3. However, when number of channels was equal to one, the noiselet encoding outperformed the Fourier encoding for an acceleration factor of 2, but not for an acceleration factor of 3. It is interesting to note that noiselet encoding outperformed Fourier encoding for both acceleration factors when the number of channels was greater than one. These simulations suggest that noiselet encoding should take into account the sensitivity information while performing CS, and therefore noiselet encoding is potentially a

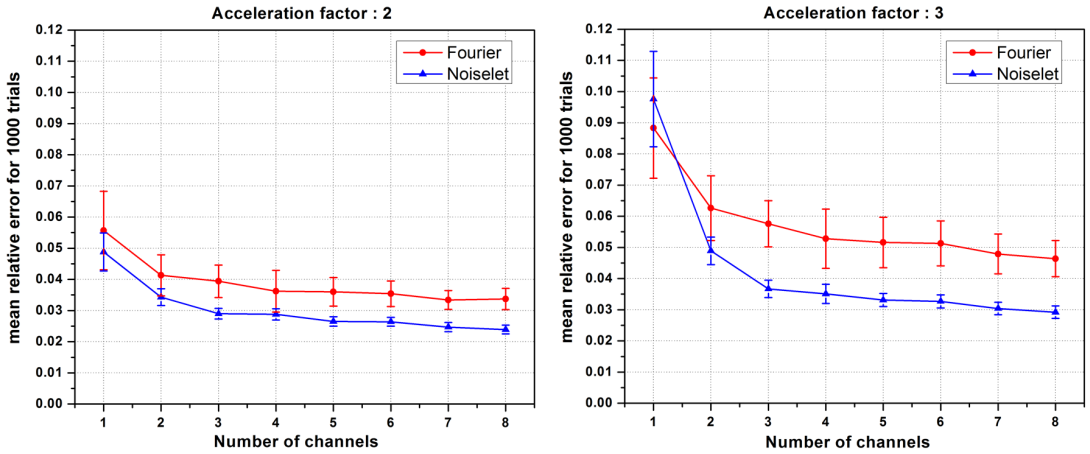

Figure 3.7: The mean relative error and standard deviation (vertical bar) versus the number of receive channels for acceleration factors of 2 and 3, showing that the error increases as the number of channels decreases. Noiselet encoding outperforms Fourier encoding for both acceleration factors when the number of channels is more than two. However for a single channel, noiselet encoding outperforms Fourier encoding only for the acceleration factor of 2.

better encoding scheme for MCS-MRI. Based on the fact that noiselet encoding performs better than Fourier encoding for multi-channel data, we investigated the performance of both the encoding schemes using muti-channel data.

3.4.2 Multiple Channel Simulation

A (256×256) brain image was used to compare the performance of noiselet encoding and Fourier encoding in MCS-MRI for different acceleration factors. Eight complex sensitivity maps (Fig. 3.8) obtained from the head coil of a Siemens Skyra 3T scanner were used to perform the simulations. For solving the minimization program in (3.3), we used the nonlinear conjugate gradient with the backtracking line search method [2]. The measurement matrix (Φ) was the discrete Fourier transform matrix while the daubechies-4 wavelet transform matrix (Ψ) and TV were used as sparsifying transforms.

Fourier encoded MCS-MRI The reference brain image was multiplied by the sensitivity function to generate eight sensitivity encoded images. The Fourier transform of each these images was taken in the PE direction; only a few PEs were taken according to the Gaussian probability distribution function. MCS-MRI reconstruction of (3.3) was solved using the nonlinear conjugate gradient algorithm on this data. An example sampling scheme for the Fourier encoded MCS-MRI is shown in Fig. 3.4(a). **Noiselet encoded MCS-MRI** A Noiselet transform of the sensitivity encoded images was taken in the PE direction, with only a few PE selected according to the uniform probability distribution function. MCS-MRI

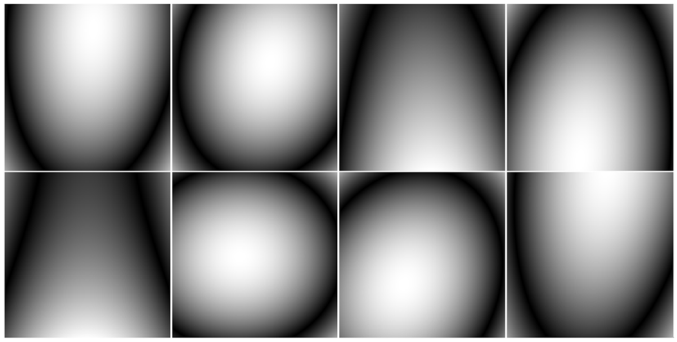

Figure 3.8: The eight coil sensitivity magnitude maps used in simulations that were estimated from the data acquired on MR scanner.

reconstruction of (3.3) was solved using the nonlinear conjugate gradient on this data. An example of the sampling scheme for noiselet encoded MCS-MRI is shown in Fig. 3.4(b).

For a noiseless simulation, the reconstructed images for different acceleration factors (4, 8 and 16) are shown in Fig. 3.9. The difference images in Fig. 3.9 (d)-(f) and (j)-(l) demonstrate that the error in noiselet encoding is always less than in Fourier encoding, and that the noiselet encoded MCS-MRI reconstruction preserves spatial resolution better than the Fourier encoded MCS-MRI. Fig. 3.9 (m) and (n) show the zoomed images reconstructed with Fourier encoding for acceleration factors of 8 and 16 respectively, while Fig. 3.9 (o) and (p) show the zoomed images reconstructed with noiselet encoding for an acceleration factors of 8 and 16 respectively. The zoomed images highlight that the spatial resolution of the noiselet encoded reconstructions outperforms the Fourier encoded reconstructions. Moreover, the spatial resolution provided by the noiselet encoding at an acceleration factor of 16 is comparable to that of the Fourier encoding at an acceleration factor of 8, suggesting that noiselet encoding performs approximately twice as good as Fourier encoding.

To measure the relative error, simulations were performed on the brain image for 1000 times by randomly generating a sampling mask each time. The mean of the relative errors was calculated after 1000 such reconstructions at every acceleration factor. The mean relative error versus the number of measurements is plotted in Fig. 3.10 and highlights that noiselet encoding outperforms Fourier encoding for all acceleration factors. The relative error for noiselet encoding at an acceleration factor of 16 was the same as the relative error for Fourier encoding at an acceleration factor of 8 indicating that higher acceleration factors are achievable with noiselet encoding compared to Fourier encoding.

In practice, MR data always has some noise and the level of noise depends upon

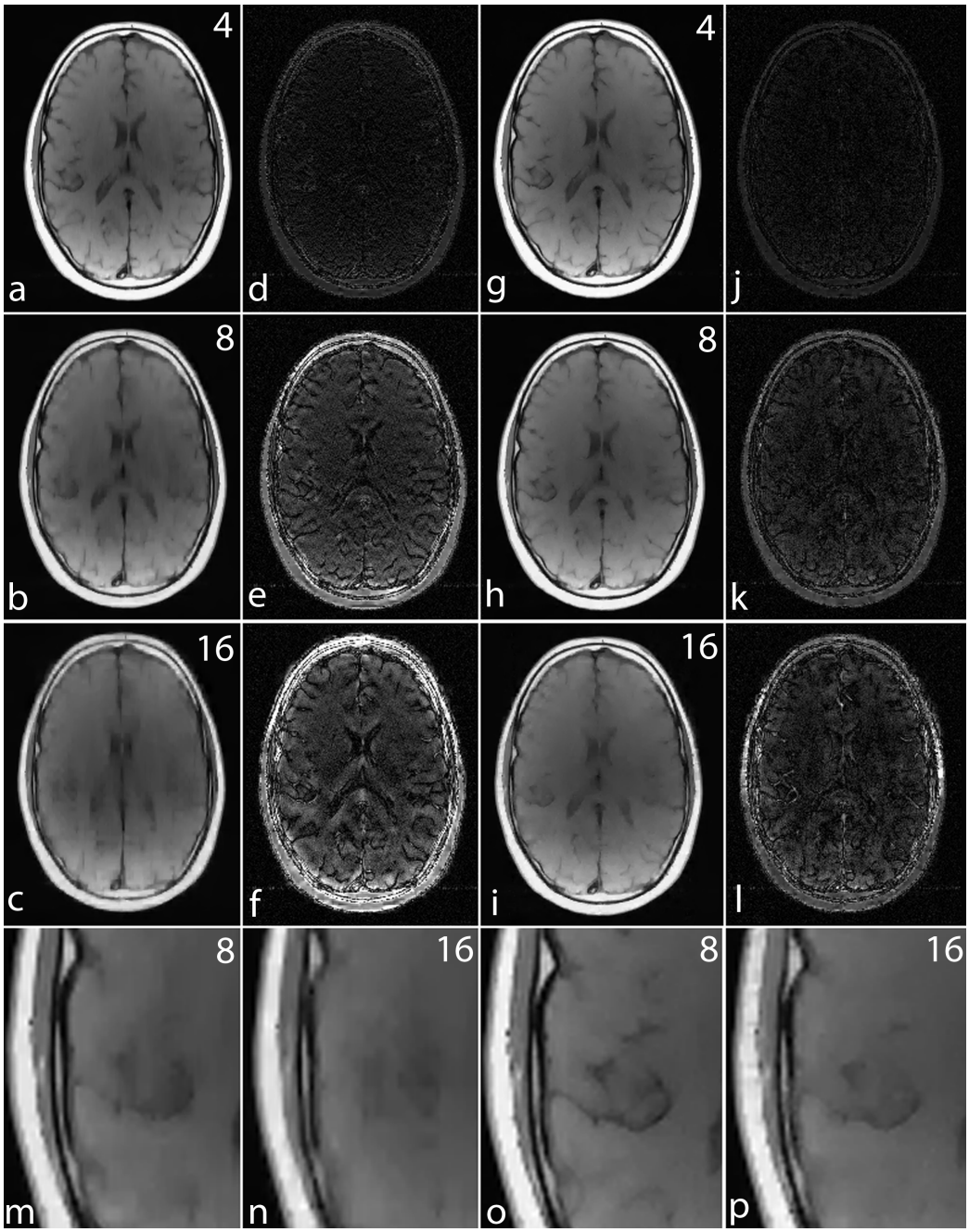

Figure 3.9: Simulation results for MCS-MRI comparing the noiselet encoding and Fourier encoding schemes (up/down: phase encodes, left/right: frequency encode). **(a)-(c):** show images reconstructed with Fourier encoding for acceleration factors of 4, 8, and 16 respectively; **(d)-(f):** show difference images with Fourier encoding for acceleration factors of 4, 8, and 16 respectively; **(g)-(i):** show images reconstructed with noiselet encoding for acceleration factors of 4, 8, and 16 respectively; **(j)-(l):** show difference images with noiselet encoding for acceleration factors of 4, 8, and 16 respectively; **(m)-(n):** show zoomed portion of images reconstructed with Fourier encoding for acceleration factors of 8, and 16 respectively; **(o)-(p):** show zoomed portion of images reconstructed with noiselet encoding for acceleration factors of 8, and 16 respectively. The zoomed images highlight that MCS-MRI using noiselet encoding reconstructions outperforms the Fourier encoding for preserving image resolution.

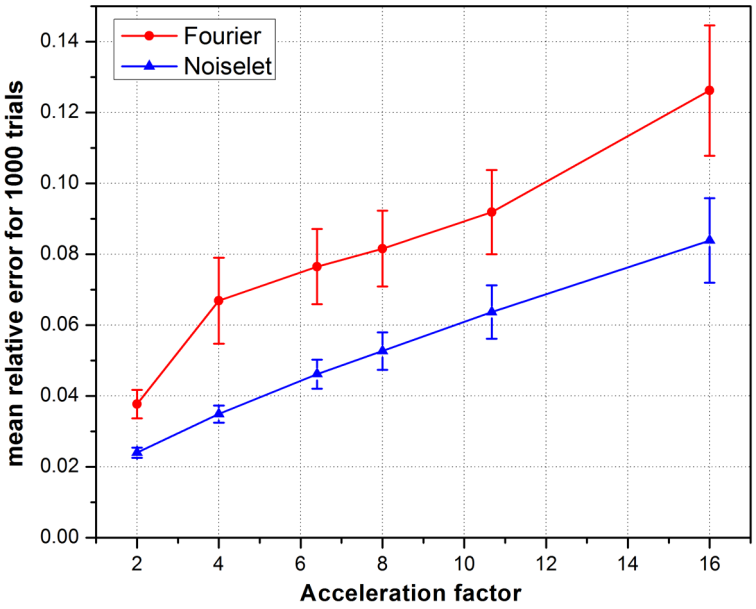

Figure 3.10: The mean relative error and standard deviation (vertical bar) versus the acceleration factor in MCS-MRI highlighting that noiselet encoding consistently outperforms Fourier encoding.

many factors including the FOV, resolution, type of imaging sequence, magnetic field inhomogeneity and RF inhomogeneity. Therefore, simulations were carried out to evaluate the performance of both the noiselet encoding and Fourier encoding schemes in the presence of variable levels of noise. Different levels of random Gaussian noise were added to the measured k-space data, and MCS-MRI reconstruction was performed for noiselet and Fourier encoding schemes. For every level of noise, 1000 simulations were performed and the mean of the relative error was calculated. Fig. 3.11 shows the mean relative error as a function of the Signal to Noise Ratio (SNR), demonstrating the comparative performance of noiselet encoding reconstructions and Fourier encoding reconstructions in the presence of noise. The plots demonstrate that noiselet encoding outperforms Fourier encoding for SNR above 20 dB for all acceleration factors, but does a poor job at SNR of 10 dB. However, as shown in the images in Fig. 3.11(d), only the images with SNR above 20 dB are adequate for diagnostic purposes. Thus, acquisitions with 10 dB SNR is not a viable scanner operation condition and the poor performance of noiselet encoding at 10 dB SNR is not a practical limitation. The poor performance of noiselet encoding at 10 dB SNR can be attributed to the fact that at extremely low SNR, most of the noiselet coefficients are severely corrupted by the noise since their magnitudes are approximately uniform. In contrast, the Fourier coefficients at the center of k-space have much larger magnitudes and hence are less affected

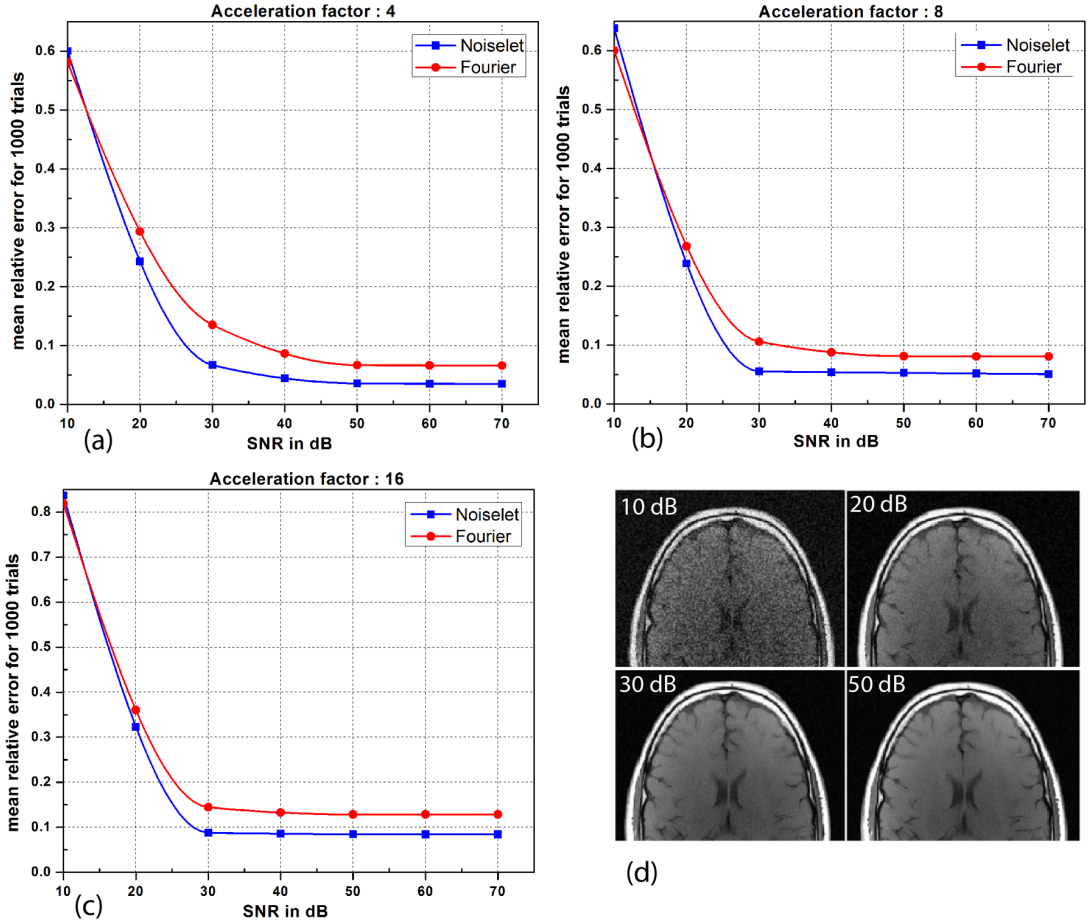

Figure 3.11: (a), (b) and (c): are the plots of the mean relative error as a function of the signal to noise ratio (SNR) for different number of measurements. When the SNR is greater than 20 dB, the noiselet encoding outperforms Fourier encoding in the presence of noise for all acceleration factors; **(d):** show the brain images with SNR of 10, 20, 30 and 50 dB.

by the noise at low SNR. These large magnitude coefficients are fully utilized in reconstruction because of the centralized variable density sampling scheme, hence Fourier encoding is less affected by the noise and performs better at low SNR.

3.5 Experiments

Experiments were carried out on Siemens Skyra 3T MRI scanner with a maximum gradient strength of 40 mT/m and a maximum slew rate of 200 mT/m/sec. Informed consent was taken from healthy volunteers in accordance with the Institution's ethics policy. To validate the practical implementation of noiselet encoding, the pulse sequence shown in Fig. 3.2 was used to acquire noiselet encoded data. An RF excitation pulse with 256 points was used with the duration equal to 5.12 ms and flip angle of 10°. We also acquired the Fourier encoded data using the

spin echo (SE) sequence to compare the quality of the reconstructed image from the data acquired by the noiselet encoding sequence. An apodized slice selective sinc RF excitation pulse was used in the spin echo sequence with a duration of 2.56 ms and a flip angle of 10°. The protocol parameters for the noiselet encoding sequence and the Fourier encoding SE sequence were **(i) Phantom experiments** FOV = 200 mm, TE/TR = 26/750 ms, averages = 2, image matrix = 256×256; and **(ii) *In vivo* experiments** FOV = 240 mm, TE/TR = 26/750 ms, averages = 2, image matrix = 256×256.

The performance of the MCS-MRI reconstruction depends on the accuracy of the sensitivity matrix estimated. We used the regularized self-calibrated estimation method [100] to estimate the sensitivity maps from the acquired data. This method estimates the sensitivity map $\hat{\Gamma}_i$ of the ith receive coil by using

$$\hat{\Gamma}_i = \min_{\Gamma} \frac{1}{2}\|I_i - \Gamma I_{ref}\|^2 + \beta R(\Gamma) \tag{3.8}$$

where $i \in [1, 2, \cdots, L]$ and $R(\Gamma)$ is a spatial roughness penalty function with weighting factor β. The reference image I_{ref} can be obtained using the sum of squares of individual coil images I_i's. For the experimental results presented below, the sensitivity maps were estimated from fully sampled images using (3.8). The data was acquired using a 32 channel head coil, but only the data from 14 channels with good SNR was used in the reconstruction.

Non-Fourier encoding in general is sensitive to field inhomogeneities, but careful design of the sequence and good shimming can result in high quality images. To reconstruct the noiselet encoded data the inverse Fourier transform was taken along the frequency encoding axis and the inverse noiselet transform was taken along the PE axis. To reconstruct the Fourier encoded data, an inverse Fourier transform was taken along both axes. Fig. 3.12 shows the images reconstructed from the noiselet encoded data and Fourier encoded data sets. These images demonstrate that the noiselet encoding reconstructions are practically feasible and produce artifact free images. Fig. 3.12(c) shows a zoomed portion of the noiselet encoded image, while Fig. 3.12(f) shows a zoomed portion of the Fourier encoded image. The zoomed images reveal that the resolution of the image from noiselet encoding with 256 noiselet excitation is the same as that of the image from Fourier encoding with 256 phase encodes. Fig. 3.12 (g) and (i) show the T2 weighted images for the brain with noiselet encoding and Fourier encoding, respectively. Fig. 3.12 (h) and (j) show the T1 weighted images for the brain with noiselet encoding and Fourier encoding, respectively. It is evident from the *in vivo*

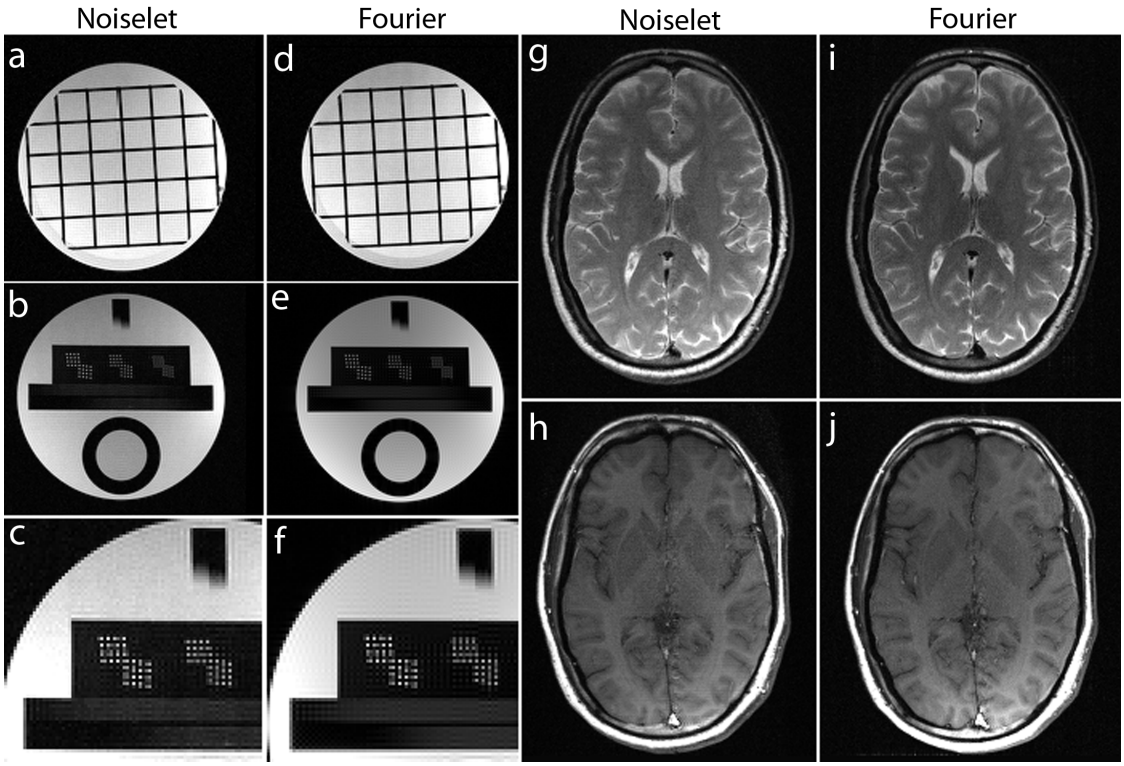

Figure 3.12: Images reconstructed using fully sampled noiselet encoded and Fourier encoded data acquired on the 3T scanner (up/down: phase encodes, left/right: frequency encode). The noiselet encoded data was acquired using the pulse sequence described in section 3.3.3, and Fourier encoded data was acquired using a conventional spin echo sequence. **(c)-(f):** show the zoomed portion of the images in (b) and (e) respectively, with the zoomed images demonstrating that noiselet encoding provides similar image resolution to that of Fourier encoding; **(g)-(h):** show T2 and T1 weighted brain images using noiselet encoding respectively; **(i)-(j):** show T2 and T1 weighted brain images using Fourier encoding respectively. These *in vivo* images demonstrate the practical feasibility of the proposed noiselet encoding scheme.

images that the proposed noiselet encoding is feasible in practice.

To validate the feasibility of the proposed reconstruction method, we performed retrospective under-sampling on the acquired noiselet encoded data and Fourier encoded data to simulate accelerated data acquisition. After retrospective under-sampling, the unconstrained optimization program (3.3) was solved using the non-linear conjugate gradient method to reconstruct the desired image for different acceleration factors. Fig. 3.13 (a)-(c) shows the reconstructed images for the acceleration factors of 4, 8 and 16 on the Fourier encoded data while Fig. 3.13 (d)-(f) shows the corresponding difference images. Similarly, Fig. 3.13 (g)-(i) shows the reconstructed images for the acceleration factors of 4, 8 and 16 on the noiselet encoded data, and Fig. 3.13 (j)-(l) shows the corresponding difference images for noiselet encoded MCS-MRI. These results on the acquired data are consistent with the simulation results and indicate that the noiselet encoding is

superior to the Fourier encoding in preserving resolution.

Fig. 3.13 (A-H) shows the zoomed portion of the reconstructed images with Fourier encoding and noiselet encoding. One can distinguish between the small dots in the zoomed images reconstructed with noiselet encoding while it is difficult to distinguish these dots in the images reconstructed with Fourier encoding. This demonstrates that noiselet encoding is able to preserve resolution better than the Fourier encoding. Fig. 3.14 show the images reconstructed with Fourier encoding and noiselet encoding for various acceleration factors on the data acquired for one axial slice of the brain. Since the SNR of the *in vivo* images is less than in the phantom images, reconstruction is shown only up to an acceleration factor of 8. The difference images demonstrate that noiselet encoding outperforms Fourier encoding for all acceleration factors. In particular, at the acceleration factor of 8 the image reconstructed with Fourier encoded data has significantly poorer resolution compared to the image reconstructed with noiselet encoded data.

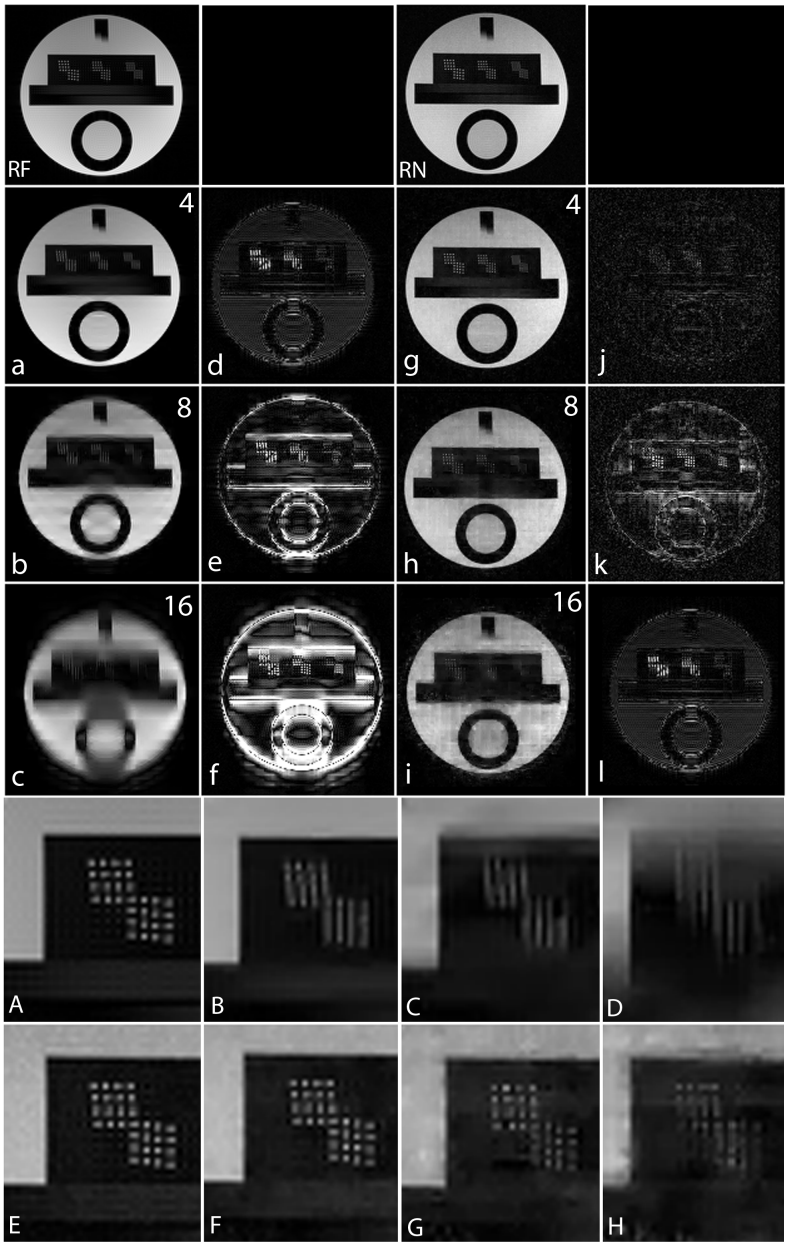

Figure 3.13: MCS-MRI reconstruction on the acquired noiselet encoded and Fourier encoded data for different acceleration factors (up/down: phase encodes, left/right: frequency encode). **RF:** shows reference image reconstructed from fully sampled Fourier encoded data; **RN:** shows reference image reconstructed from fully sampled Noiselet encoded data; **(a)-(c):** show images reconstructed using Fourier encoding for acceleration factor of 4, 8 and 16 respectively; **(d)-(f):** show the difference images using Fourier encoding for acceleration factor of 4, 8 and 16 respectively; **(g)-(i):** show images reconstructed using noiselet encoding for acceleration factor of 4, 8 and 16 respectively; **(j)-(l):** show the difference images using noiselet encoding for acceleration factor of 4, 8 and 16 respectively. The result here aligns with the simulation results and noiselet encoding outperforms Fourier encoding in preserving resolution. **(A-H):** Zoomed portion of phantom images reconstructed with Fourier encoding and noiselet encoding with different acceleration factors. **(A):** shows the original image reconstructed from fully sampled Fourier encoded data; **(B), (C) and (D):** show the Fourier encoded reconstructed images for acceleration factors of 4, 8 and 16 respectively; **(E):** shows the image reconstructed from fully sampled noiselet encoded data; **(F), (G) and (H):** show the noiselet encoded reconstructed images for acceleration factors of 4, 8 and 16 respectively demonstrating that noiselet encoding produces improved resolution images than than Fourier encoding at all acceleration factors.

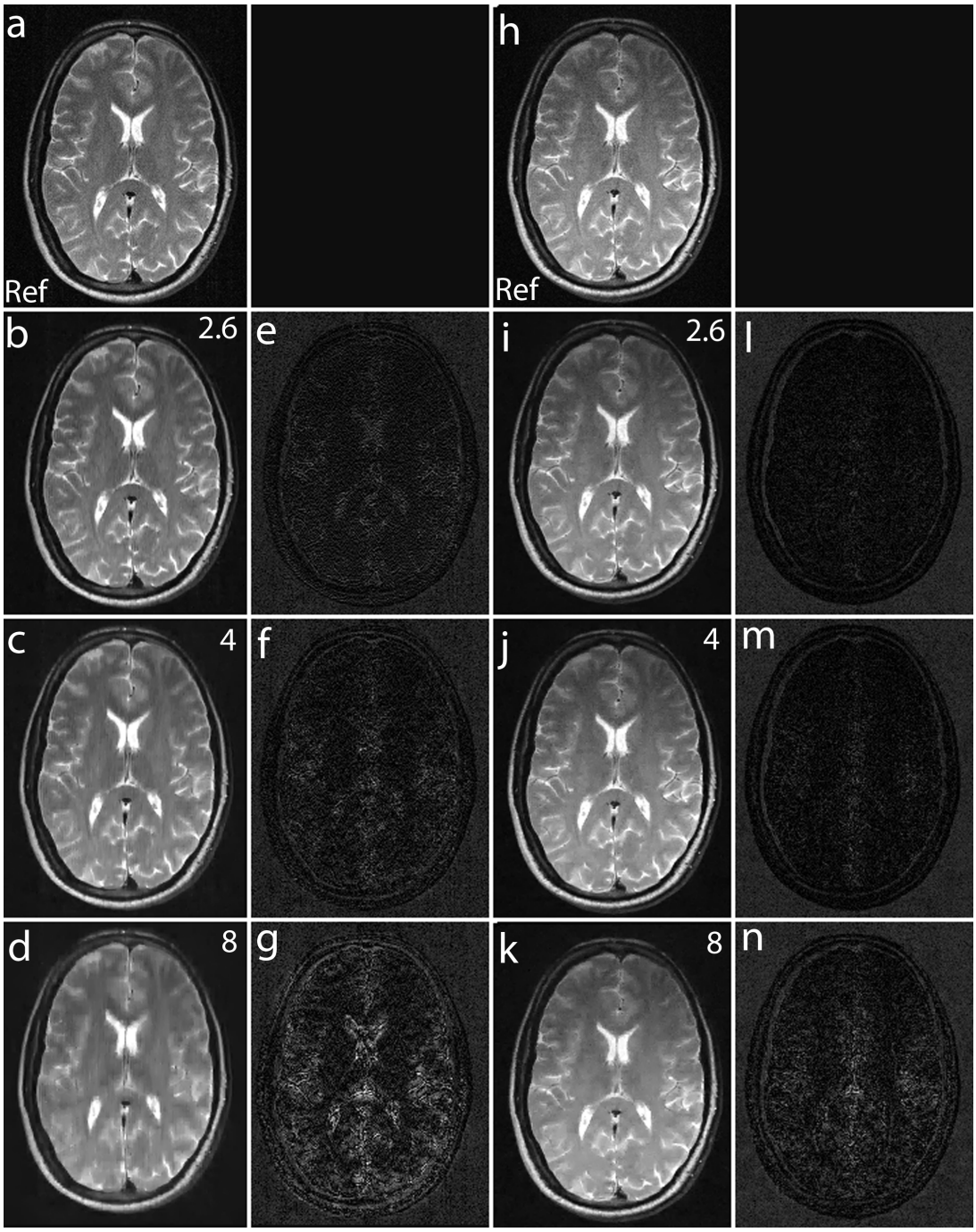

Figure 3.14: MCS-MRI reconstruction on *in vivo* brain images using acquired noiselet encoded and Fourier encoded data for different acceleration factors (up/down: phase encodes, left/right: frequency encode). **(a):** shows reference image reconstructed from fully sampled Fourier encoded data; **(b)-(d):** show images reconstructed using Fourier encoding for acceleration factor of 2.6, 4 and 8 respectively; **(e)-(g):** show the difference images using Fourier encoding for acceleration factor of 2.6, 4 and 8 respectively; **(h):** shows reference image reconstructed from fully sampled Noiselet encoded data; **(i)-(k):** show images reconstructed using noiselet encoding for acceleration factor of 2.6, 4 and 8 respectively; **(l)-(n):** show the difference images using noiselet encoding for acceleration factor of 2.6, 4 and 8 respectively. It can be seen from the difference images that noiselet encoding outperforms Fourier encoding on the acquired invivo data. The loss in resolution is clearly visible for Fourier encoding at an acceleration factor of 8.

Fig. 3.15 shows the images reconstructed with noiselet and Fourier encodings using 3D GRE sequence. In our implementation of noiselet encoding in 2D spin echo sequence, the flip angle of 10° was used, which results in loss of some available SNR. Therefore, we have implemented noiselet encoding in 3D Gradient Echo (GRE) sequence as shown in Fig. 3.2 (b), which uses noiselets encoding in one direction and Fourier encoding in other two directions. The noiselet encoding is performed using specially selective RF excitation pulse, while the Fourier encoding is performed using gradients. Phantom data was acquired using this sequence with the following parameters: FOV = 200×200 mm^2, TE/TR = 6.5/13 ms, slices = 32, FOV of slice = 160 mm, flip angle = 5° and (noiselets) phase encodes = 256. A 3D Fourier encoded data was also acquired with exactly same parameters. It can be seen from the images that the noiselet encoding provides similar quality of images to that of Fourier encoding. These images are only shown here to demonstrate the feasibility that noiselet encoding can be implemented in 3D GRE sequence.

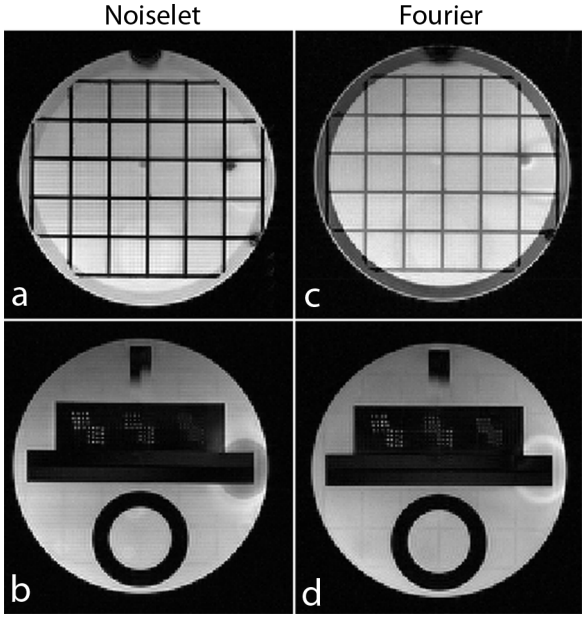

Figure 3.15: (a) and **(b):** Two slices of image reconstructed using 3D GRE noiselet encoding sequence, the up/down direction is noiselet encoding direction and left/right direction if Fourier encoding direction; **(c)** and **(d):** two slices of image reconstructed with Fourier encoding using 3D GRE sequence.

3.6 Discussion

We have presented a new method of encoding the MR data in PE direction with noiselet basis functions for accelerating MRI scans using MCS-MRI reconstruc-

tion. The simulation results demonstrate that the proposed encoding gives rise to a multichannel measurement matrix with improved RIP, and the reconstruction method using the noiselet bases outperforms the conventional Fourier encoding scheme. The mean relative error for noiselet encoding at the acceleration factor of 16 is comparable to that of Fourier encoding at the acceleration factor of 8, demonstrating that higher acceleration factors can be achieved with noiselet encoding than the Fourier encoding in the MCS framework.

The reconstruction from the noiselet encoding scheme preserves image spatial resolution far better than the Fourier encoding scheme. The Fourier encoding scheme intelligently exploits the property of k-space since most of the energy is concentrated at the center of the k-space. Therefore, densely sampling the center and randomly under-sampling the outer regions of the k-space retains most of the energy in the acquired data. However retaining most of the energy does not imply that most of the information is captured in the acquisition. The low energy (high frequency) component in the outer k-space contains the information about the fine features of the image that the variable density random under-sampling pattern fails to capture. Therefore, the images reconstructed with the Fourier encoding scheme look visually good but have reduced resolution due to insufficient information about the high frequency components in the acquired data. On the other hand, noiselet encoding completely spreads out the energy of the signal in the measurement domain. Therefore each measurement in the noiselet domain has sufficient information to reconstruct the fine details of the image, thus preserving the resolution better than the Fourier encoding.

Noiselet basis functions have some interesting properties that can be exploited, for example noiselets are unitary basis functions and have complex conjugate symmetry. This conjugate symmetry property can be exploited in a way similar to that of the Fourier encoding for partial acquisition [101, 102]. Another interesting property of noiselet basis functions, as for the Fourier basis functions, is that regular under-sampling in the noiselet domain results in aliasing in the image domain. Therefore in the case of regular under-sampling in the noiselet domain, unaliasing with SENSE [21] alone can also be used for noiselet encoding.

In general the implementation of non-Fourier encoding suffers from a few limitations, and hence the current implementation of noiselet encoding also suffers from these limitations as summarized below. (i) In 2D imaging implementation of noiselet encoding, the excitation of noiselet profile is not slice selective, thus a slice selective 180° pulse is required after excitation, which limits the noiselet encoding to spin echo type sequences. The spin echo sequence always have long TR, there-

fore the proposed noiselet encoding can only be used for applications requiring long TR, such as structural scans, but will be of little use in dynamic imaging. (ii) In the current implementation, to simplify the design of noiselet excitation pulse we have used direct Fourier transform method that limits the excitation to the low flip angle regime, resulting in the sacrifice of some available SNR. (iii) The duration of noiselet RF excitation pulse is long compared to the conventional sinc RF pulse and the noiselet encoding can only be implemented in one direction in the current implementation. (iv) Due to dielectric effects, etc, in practice, B1 field is always not perfectly homogeneous. Because B1 is used for spatial encoding in the proposed noiselet encoding scheme, B1 inhomogeneity may introduce some perturbations to the noiselet measurement matrix, which in turn may result in some image artifact if the perturbation is large.

The above limitations are not specific to noiselet encoding scheme but are common to all non-Fourier encoding schemes. Here we discuss some probable solutions to the above mentioned problems. (i) The problem of slice selection can be alleviated using a 3D gradient echo (GRE) sequences where a 3D volume can be excited with a noiselet profile in one dimension and other two dimensions can be Fourier encoded. A demonstrative pulse sequence for this solution has been given in Section 3.3.3 and its scan result has been given in Section 3.5, showing the feasibility of this solution. (ii) The low tip angle in current implementation is the limitation of the direct Fourier transform method used to compute the RF pulse. It is not an intrinsic limitation of noiselet encoding. Although difficult, computation of large tip angle noiselet RF pulse is possible by using nonlinear computation methods such as direct iterative solution of Bloch equation [103] and the SLR method [104, 105], which are currently being investigated. (iii) The duration of the RF pulse can be reduced by using parallel-transmit and multiple dimensional excitation of noiselet profiles to achieve encoding [103, 106]. This is our ongoing research. (iv) The perturbations to the measurement matrix induce an equivalent deterministic noise additive to the measured MR signals. When the inverse noiselet transform is applied directly to the fully sampled dataset to reconstruct the image, a structured artifact may show up if the perturbation is large. This problem can be alleviated when the CS reconstruction method as given in (3.3) is used for image reconstruction. This is because the CS reconstruction algorithm has inherent denoising capability, which can suppress small perturbations by enforcing the prescribed bound ϵ on the reconstruction error. See Section 3.2 and the references therein for detailed discussions. For this reason and also because of the high quality of the new 3T scanner used in our experiments, we have

not observed structured image artefacts in the experiments presented in Section 3.5.

3.7 Conclusion

In this chapter we have introduced a method of acquiring data in the noiselet domain and presented a method for the design and implementation of pulse sequences to acquire data in the noiselet domain. The performance of the noiselet encoding has been thoroughly evaluated by extensive numerical analysis, simulation and experiments. The results indicate that the multichannel noiselet measurement matrix has better RIP than that of its Fourier counterpart, and that the noiselet encoding scheme in MCS-MRI outperforms the conventional Fourier encoding in preserving image resolution, and can achieve higher acceleration factors than the conventional Fourier encoding scheme. The implementation of noiselet encoding by tailoring spin echo and gradient echo sequences demonstrates that the proposed encoding scheme is pragmatic. The proposed technique has the potential to accelerate image acquisition in applications that require high resolution images.

Chapter 4

K-Space Aliasing for Accelerated Imaging

In chapter 3, we presented a method to accelerate static imaging with multichannel CS using noiselet encoding. However, the dynamic imaging application are the ones that can benefit most from accelerated imaging. Therefore in this chapter we propose a novel method to accelerate dynamic MRI scans using a new technique of k-space aliasing.

4.1 Introduction to Dynamic MRI

The goal of dynamic MRI is to capture the time evolution of a signal of interest through the fast acquisition of k-t space. Since MRI acquires signal from a preferred imaging location through the use of magnetic field gradients, only a sequential acquisition of k-t data is possible, thus placing fundamental restrictions on the maximum spatial and temporal resolution that can be simultaneously realized by a dynamic MRI acquisition. Over the years, several methods have been proposed to address this issue while some of these methods make certain assumptions about the imaged object and/or temporal signal of interest [3–19], other techniques operate independent of the same [20–24]. The assumptions, when made, are typically done so to exploit any spatial and/or temporal redundancy that may exist in the k-t data that is to be acquired.

Of the various dynamic MRI methods that make assumptions about the imaged object and/or temporal information, some are of particular interest given the work presented here. These are techniques such as UNFOLD [16] and reduced FOV approaches [12–15], which operate on the assumption that dynamic infor-

mation is largely confined to a portion of the imaged object and methods such as keyhole imaging [3–7], TRICKS [8] and others [9,10] that make a similar assumption of the imaged objects k-space representation.

Provided their assumptions hold, these methods can tailor the acquisition of k-t data to capture information efficiently. For example, in UNFOLD spatially distinct voxels are deliberately overlapped by under-sampling k-space while simultaneously tagging the overlapped voxels in time with a phase function. A Fourier transformation along the time axis of k-t space can then resolve the aliased voxels. In methods such as keyhole imaging and the like, while central k-space is acquired in every time frame, it is assumed that the higher spatial frequencies contain little or no dynamic information and are therefore acquired less frequently. Techniques such as Fourier interpolation, weighted substitution, utilizing a priori information [18, 19] and sliding window reconstruction are then used to estimate the unacquired data points. Irrespective of the assumptions, in all these approaches, the acquisition of k-t space is altered in an attempt to satisfy the competing requirements for spatial and temporal resolution.

Separately, image acceleration techniques falling under the category of Parallel Imaging (PMRI) [20–24] and Compressed Sensing (CS) [2] have also been employed to increase spatial and/or temporal resolution of a dynamic MRI scan. While PMRI methods rely on spatial encoding provided by multiple RF coils to complement the MRI gradient encoding process, CS methods are applicable when certain conditions related to the sparsity of the MRI image or its representation in a transform domain are fulfilled. These techniques can be employed either independently [2, 24, 73, 107, 108] or in tandem [109, 110] with any of the methods previously mentioned to accelerate a dynamic MRI scan. Despite the advances, applications such as interventional imaging [25], contrast enhanced MR Angiography [26], evaluation of cardiac function [27] and abdominal imaging [28] can always benefit from larger acceleration factors. The fundamental limitation in these and other dynamic imaging applications continues to be the trade-off between spatial and temporal resolution.

In this chapter, we introduce the concept of k-space aliasing and attempt to address this trade-off between spatial and temporal resolution by leveraging the same. The method, here after referred to as RATE (Rapid MRI Acquisition using Tailored Signal Excitation modules), utilizes a combination of RF excitation pulses and gradient waveforms to deliberately overlap distinct k-space points. The method exploits the fact that in most dynamic imaging, a non-uniform distribution of energy in k-space results in different regions exhibiting different temporal

bandwidths. By accelerating the scan through k-space aliasing, additional temporal bandwidth is made available and the same is used to accommodate the differing temporal bandwidths of the overlapped k-space points. Additionally, the amplitude and phase of the RF excitation pulses are used to tag the overlapped k-space points that then enables the use of a simple Fourier transformation along the time axis of the acquired data to resolve the overlapped k-space points.

A feature of the technique is that overlapping of k-space points is achieved through the signal excitation process and not through the use of any data sampling trajectory. Furthermore, as demonstrated in this work, the method can be combined with Parallel Imaging to achieve very large acceleration factors.

4.2 Theory

4.2.1 Signal Excitation in RATE

In order to acquire overlapped or aliased k-space data with a pulse sequence, the conventional RF excitation pulse in the sequence is replaced by a signal excitation module comprising of RF excitation pulses and gradient waveforms. A simple example of such a module is given in Fig. 4.1 for a k-space aliasing factor R_k = 2. The two RF pulses in this module will generate two Free Induction Decay (FID) signals and one spin echo. Table 4.1 lists the analytical expressions for the amplitudes of each of these signal pathways along with their values for two different sets of flip angles. For Set.2, the FIDs are the dominant signal pathways while the spin echo is 42 dB weaker than the weakest FID and is therefore irrelevant. Once a condition is established wherein the FIDs are the dominant signal pathways, the phase encoding blips in the module can be used to encode the two FIDs to different phase encoding locations. A readout gradient that follows such a module will now detect the two FIDs simultaneously resulting in an aliased acquisition. The total signal resulting from the excitation module under such conditions is given by:

$$S(t) = \int O(x,y)\{a_1 e^{-jk_1 y} + a_2 e^{-jk_2 y}\} e^{-jk_x x} dx\, dy \tag{4.1}$$

Here, $k_1 = \gamma(G_{pe1} + G_{pe2})t_p, k2 = \gamma(G_{pe2})t_p, t_p$ is the duration of the phase encode blips, $O(x,y)$ is a 2D slice of the imaged object and a_1, a_2 are the FID amplitudes given by the analytical expressions in Table 4.1.

One or both the phase encoding blips in the module can now be varied from

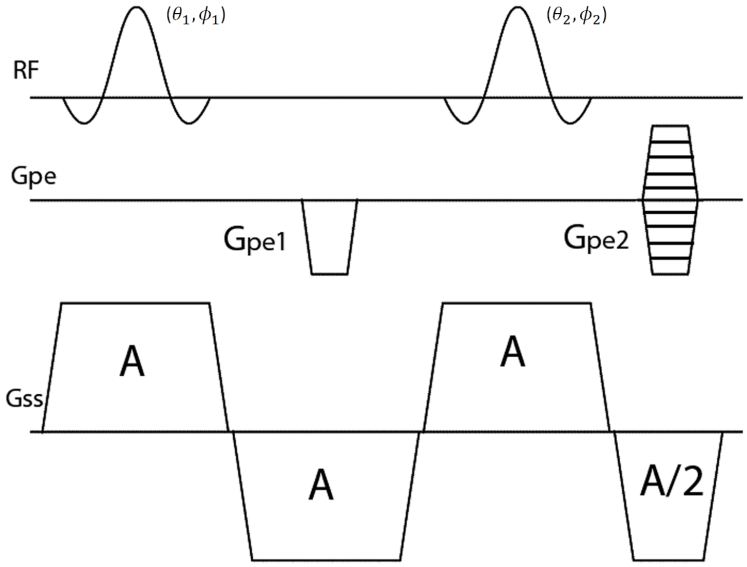

Figure 4.1: The RATE module for N=2 consisting of two RF pulses with flip angle and initial phase of (θ_1, ϕ_1) and (θ_2, ϕ_2) respectively. In this implementation, G_{pe1} is kept constant while G_{pe2} is varied from one TR to the next. A denotes the areas of the respective slice select gradient and rewinder lobes.

Table 4.1: Magnitude of signal pathways generated by using two excitation RF pulses

Siganl pathways	Amplitude	Set - 1	Set - 2
		$\theta_1 = 90°, \theta_2 = 90°$ $\phi_1 = \phi_2 = 0°$	$\theta_1 = 10°, \theta_2 = 10°$ $\phi_1 = \phi_2 = 0°$
FID - 1	$sin(\theta_1)cos^2(\theta_2/2)e^{j\phi_1}$	0	0.1666
FID - 2	$cos(\theta_1)sin(\theta_2)e^{j\phi_2}$	0	0.3502
Spin Echo-1	$sin(\theta_1)sin^2(\theta_2/2)$	1	0.0013

one TR to the next in order to complete an aliased 2D acquisition. For 3D k-space aliasing, the secondary phase encoding axis must be introduced inside the module along with additional secondary phase encoding blips. In order to acquire sub-sampled aliased k-space that can later be restored through PMRI, a simple increase of the step size of one or more of the phase encoding blips in the module will suffice.

The excitation module is compatible with all pulse sequences and depending on the sequence in which it is used, the effective acceleration that is achievable will vary. For instance, with a short TR SSFP [111] sequence, a large R_k excitation module will result in increased TE and TR that will quickly negate the benefits of acceleration provided by the module itself. However, the excited aliased signals property is such that the one or more k-space lines acquired in a TR will always be from the desired aliased k-space. As a result, the modules can be used sparingly in time efficient multiple echo sequences such as EPI [112] that preserve the benefits of acceleration. Therefore, in this work, an IGEPI [113] sequence was preferred to demonstrate the larger acceleration factors.

4.2.2 Application to dynamic imaging

As can be seen from the analytical expressions of a_1, a_2, the amplitudes and phases of the FIDs are user controlled through the flip angles and phases of the RF excitation pulses in the excitation module. Therefore, given eqn.(4.1), it can be stated that the coefficients a_1, a_2 are tagging coefficients that are used to control the magnitudes and phases of the individual FID signal pathways and is a useful property when using the module in dynamic imaging scenarios.

For instance, consider a dynamic imaging scan where the module from Fig. 4.1 is used in a pulse sequence to acquire aliased and thus accelerated k-t space. Now, in the first time frame of this acquisition, assume the user sets the RF phases to be $\phi_1 = \phi_2 = 0$, such that two phase encodes k_1 and k_2 overlap onto a single k-space point $k_a = k_1 + k_2$. Next, during the second time frame, all module parameters remain the same except for ϕ_2, which the user sets to π. The overlapped point k_a is now $k_1 - k_2$. Now, consider the acquisition of a time series of images where $\phi_1 = \phi_2 = 0$ for every even time frame and $\phi_1 = \phi_2 = \pi$ for every odd time frame. The overlapped point k_{alias} is then given by the following equation:

$$k_a(t) = k_1 + k_2 e^{j\pi t} \tag{4.2}$$

Here, t is the time frame number. If the overlapped phase-encodes contain dynamic information, then eqn.(4.2) becomes the following:

$$k_a(t) = k_1(t) + k_2(t)e^{j\pi t} \tag{4.3}$$

A Fourier transformation in time will give the temporal frequency spectrum of $k_a(t)$. This spectrum will consist of the spectrum of $k_1(t)$, centered at DC, and that of $k_2(t)$, centered at the Nyquist frequency. As shown in Fig. 4.2, the two spectra can now be separated using a simple filter. For R_k (k-space aliasing factor) $= N$, the signal at the overlapped k-space point is given by:

$$k_a(t) = \sum_{n=1}^{N} k_n(t)e^{j\phi_n(t)} \tag{4.4}$$

In eqn.(4.2) - (4.4), the magnitudes of all the 'a' coefficients have been assumed to be unity.

Clearly, in order for this process to be successful, there must exist a relative difference in the temporal bandwidths of the overlapped k-space points, in this case $k_1(t)$ and $k_2(t)$. For instance, in Fig. 4.2, it is assumed that $k_1(t)$ is more dynamic than $k_2(t)$. Crucially, no assumptions need to be made about the relative difference between the temporal bandwidths of these two points and it is only required that there exist such a difference for the RATE method to be applicable. However, the extent of this difference does have an impact on the efficiency of the process and as a result, the effective acceleration that can be achieved. For instance, if only one of the overlapped points were dynamic in Fig. 4.2 while the other remained completely static, the method will result in maximum efficiency as all the additional temporal bandwidth provided by acceleration can be allocated to just one point. However, when both points are equally dynamic, the technique will prove ineffective as the overlaps can never be fully corrected. In between these two extremes there exist a whole range of dynamic imaging conditions where the technique will function with varying degrees of efficiency.

Therefore, the effective achievable acceleration due to RATE is given by the following:

$$A_{eff} = \eta A_{target}\left(\frac{TR_{orig}}{TR_{RATE}}\right) \tag{4.5}$$

Here, η is the maximum fraction of the additional temporal bandwidth allocated to a particular portion of k-space usually central k-space, A_{target} is equal to R_k, TR_{orig} is the original TR of the pulse sequence and TR_{RATE} is the new TR after the

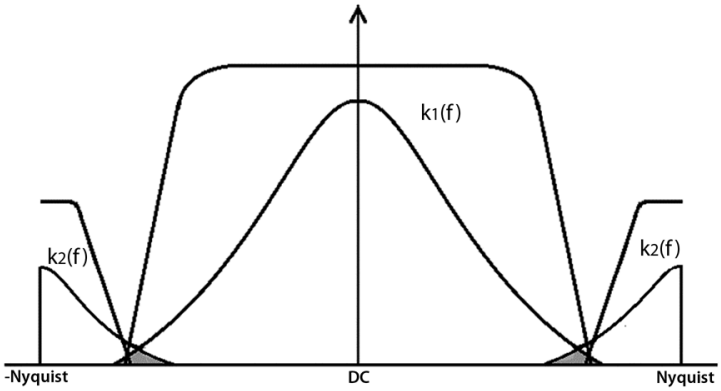

Figure 4.2: The temporal spectra of two overlapped points is shown wherein $k_1(f)$ is more dynamic than $k_2(f)$. The Fermi filter used to extract $k_1(f)$ has a larger bandwidth compared to the filter used to extract $k_2(f)$.

insertion of the RATE module.

4.2.3 Improving A_{eff} with Parallel Imaging

As can be seen from eqn.(4.5), there are two sources of inefficiency that can result in A_{eff} that is lower than what was desired. The first source of inefficiency is caused by the insertion of the signal excitation module into the pulse sequence while the second source of inefficiency is η, which is a function of the differences in the temporal bandwidths across various regions of k-space. Moreover, the factor η depends on the nature of the dynamic scan itself and there is little flexibility available to the user in defining the same without loss of information. However, the first source of inefficiency can be addressed, at least for the IGEPI sequence, by increasing the acquisition echo-train length (ETL). Nevertheless, as R_k is increased, large ETL will be required to compensate for the same that can result in increased eddy current related artifacts. Another powerful and easy to implement option for increasing A_{eff} is to use the RATE method in combination with PMRI. The acquisition of aliased, sub-sampled k-space using the RATE-PMRI combination will result in an $A_{target} = R_k \times R_{pmri}$ where R_{pmri} is the acceleration factor due to PMRI. Clearly, such a combination will provide effective acceleration factors larger that of either of the two methods individually.

Fig. 4.3 shows the sampling pattern that can be used for simultaneous aliasing and sub-sampling of k-space. The aliased k-space (Fig. 4.3(c)) is regularly sub-sampled to get aliased and sub-sampled k-space (Fig. 4.3(e)) resulting in reduced dimension aliased image (Fig. 4.3(f)).

A complete realization of the proposed method is now possible through the

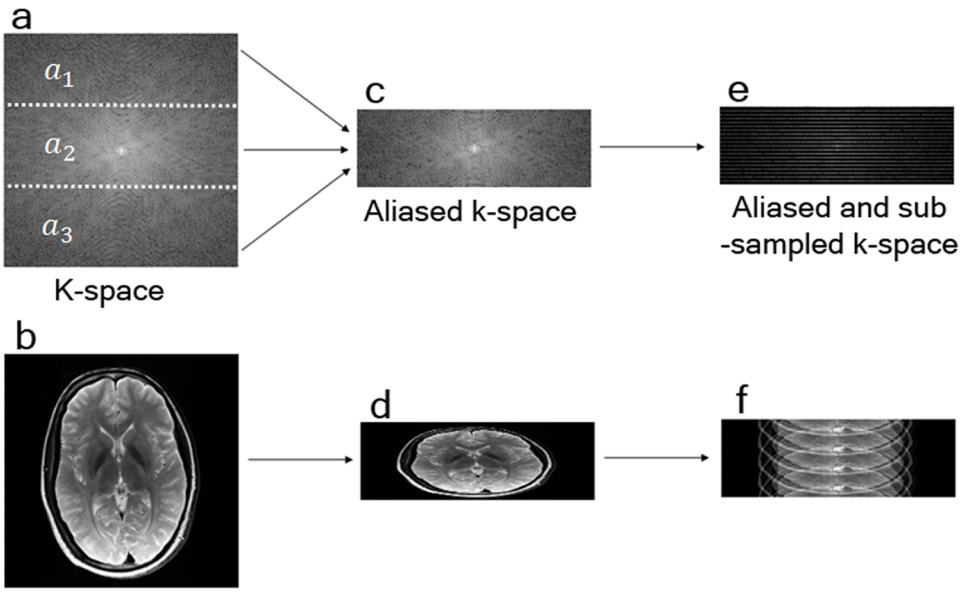

Figure 4.3: (a): k-space for the brain image where a_1, a_2 and a_3 are top, middle and bottom portion of k-space; (b): brain image corresponding to k-space in a; (c): aliased k-space generated by adding a_1, a_2 and a_3; (d): image corresponding to k-space in c; (e): aliased and sub-sampled k-space formed by sub-sampling c; (f): image corresponding to k-space in e.

following steps:

Step 1: Design the RATE signal excitation module with the following design parameters: (a) the k-space acceleration factor A_{RATE} (b) Appropriate choice of θ and ϕ (c) All relevant gradient waveforms for performing FID encoding. Finally, optimize the duration of the RATE module to improve A_{eff}.

Step 2:: Insert the RATE module into the desired pulse sequence and collect multiple time frames of k-aliased data by incrementing ϕ of all the RF pulses as a function of time frames.

Step 3: Fourier transformation along the temporal axis of the acquired data followed by filtering to separate the overlapped spectra.

Step 4: Generate the final un-aliased $k-t$ data by re-locating the unaliased phase-encodes to their respective locations in $k-t$ space.

Step 5: If sub-sampling is also performed, the result of step 4 will be regularly under-sampled $k-t$ space. GRAPPA reconstruction can then be applied on this data to generate the final, fully restored dataset.

These implementation stages in the RATE and RATE-PMRI combination have been listed in the flow chart in Fig. 4.4. In this work, the GRAPPA [23] method was preferred for the PMRI reconstruction stage.

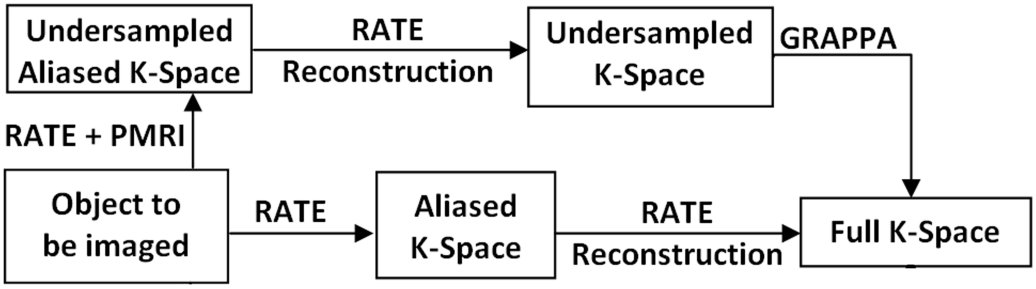

Figure 4.4: Flow chart showing acquisition and reconstruction for k-space aliasing and k-space aliasing with sub-sampling.

4.3 Methods

All data reconstruction was performed on MATLAB (Natick, USA) using a computer with an Intel dual core 1.8GHz processor and 2GB of RAM.

Simulated data: First, simulated data studies were performed on a cardiac (PINCAT) [114] numerical phantom of dimension 240×240 with 60 time frames and a temporal bandwidth of 40 Hz. For $R_k = 3$, the RATE signal excitation module will generate a total of eight signal pathways of different magnitudes that will be a function of the flip angles of the RF excitation pulses in the module. Therefore, in order to determine the impact of the residual signal pathways on reconstruction accuracy, all eight signal pathways that would be generated by the module were simulated and encoded to their appropriate locations along the phase encoding axis. The simulated flip angles of the 3 RF pulses in the module were set to 10° each. Next, the top, middle and bottom phase encode blocks in 2D k-space, containing 80 phase encodes each, were overlapped to generate an aliased k-space time frames. Only the top and bottom phase encode blocks were tagged with the RF phase values of $-5\pi t/6$ and $5\pi t/6$ radians respectively, where t was time frame number. In order to restore the un-aliased $k-t$ space dataset, the overlapped time frames were stacked together to form an overlapped $k-t$ space dataset and a Fourier transformation was performed along the time axis of this dataset. This resulted in a separation of the overlapped spectra, enabling the use of Fermi filters to filter out the overlapped spectra. The maximum fraction of the additional temporal bandwidth ($\eta = 0.8$) was allocated to the central k-space phase encode block as it contained the maximum amount of energy. An inverse Fourier transformation on this dataset resulted in the final set of restored images. In these simulations, the loss in acceleration due to the insertion of the RATE module was ignored.

***in-vivo* data:** A total of five *in-vivo* datasets for cardiac triggered cine imaging

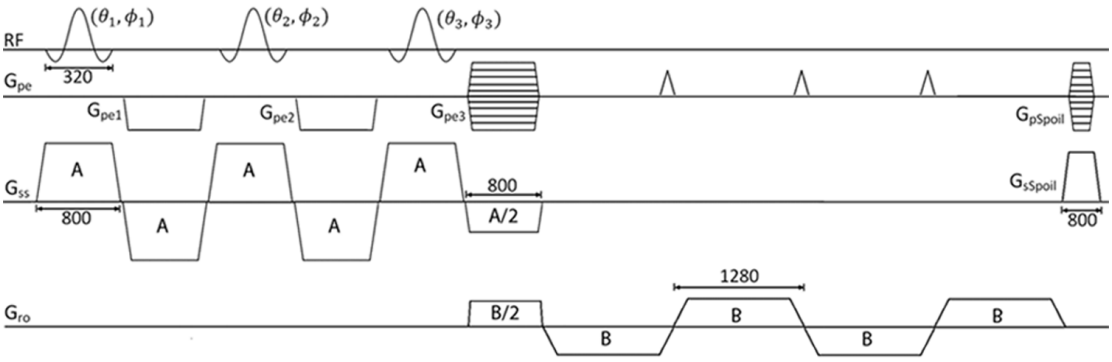

Figure 4.5: Sequence diagram used to acquire k-space aliased dataset that consist of three excitation RF pulses with the flip angle and initial phase of $(\theta_1, \phi_1), (\theta_2, \phi_2)$ and (θ_3, ϕ_3) respectively; G_{pe1} and G_{pe2} were gradient in PE direction that kept constant for the whole acquisition and G_{pe3} is varied for each TR; A and B denotes a finite area under the slice and read gradient respectively; G_{pe}, G_{ss} and G_{ro} were the gradient in phase, slice and readout direction respectively; all timings are in micro seconds.

were acquired of which two were fully sampled datasets and three were accelerated (aliased k-space) datasets. One fully sampled dataset was acquired using gradient echo (GRE) sequence and other was acquired using interleaved gradient echo EPI (IGEPI) with echo train length (ETL) equals to 4. Two accelerated datasets with acceleration factor of 2 and 3 was also acquired using GRE sequence. One accelerated dataset with acceleration facotor of 3 was acquired using IGEPI sequence. An IGEPI sequence for acquisition of aliased k-space data is shown in Fig. 4.5. The accelerated dataset acquires aliased k-space data and the phase encodes for such data is refereed to as aliased phase encodes (APEs). The tagging coefficients in aliasing module designed for acceleration factor of 3 were $-5\pi t/6, 0$ and $5\pi t/6$ for first, second and third RF pulse respectively, where t is time frame number. Table 4.2 shows the parameters used for the scanning protocol.

4.4 Results

All experimental data were acquired on a commercial 3T MRI scanner (Skyra, Siemens Medical Systems, Erlangen, Germany) using 18 receiver elements. Several datasets were acquired to validate the performance of the proposed method and results from some of these datasets are reported next. Informed consent was obtained from all volunteers.

Table 4.2: Parameter for *in-vivo* data acquisition protocol

Parameters	Accelerated datasets-I	Accelerated datasets-II	Accelerated datasets-III	Fully sampled datasets-I	Fully sampled datasets-II
Acceleration factor	2	3	3	-	-
Echo train length (ETL)	1	1	4	1	4
TR (ms)	4.4	5	12	5	12
Temporal resolution (ms)	17.6	20	12	40	36
Number of heart beats	30	20	30	30	20
Cardiac phases	32	30	48	17	24
Flip angle	(5°,5°)	(5°,5°,5°)	(10°,10°,10°)	10°	10°
FOV (mm^2)	300×300	300×300	300×300	300×300	300×300
Aliased phase encodes	120	80	80	-	-
Phase encodes	-	-	-	240	240
Resolution (mm^2)	1.25×1.25	1.25×1.25	1.25×1.25	1.25×1.25	1.25×1.25
Bandwidth (Hz/Pixel)	1220	1220	1220	1220	1220
Slice thickness (mm)	8	8	8	8	8
η	0.8	0.8	0.8	-	-
Image matrix	240×256	240×256	240×256	240×256	240×256

4.4.1 Simulation results

Fig. 4.6 displays the results from the simulation studies on the PINCAT Phantom for R_k=3. Fig. 4.6(a) demonstrates the manner in which the spectra of three overlapped k-space points are separated by applying the Fourier transformation along the temporal axis. Fig. 4.6(b) is a single timeframe from the original dataset while the image in Fig. 4.6(c) is the same time frame reconstructed after k-space unaliasing. The error plot shown in Fig. 4.6(d) confirmed that for this particular ROI, the maximum difference between the original and reconstructed time domain signal was 2 %. This was also the maximum error value over the entire reconstructed dataset.

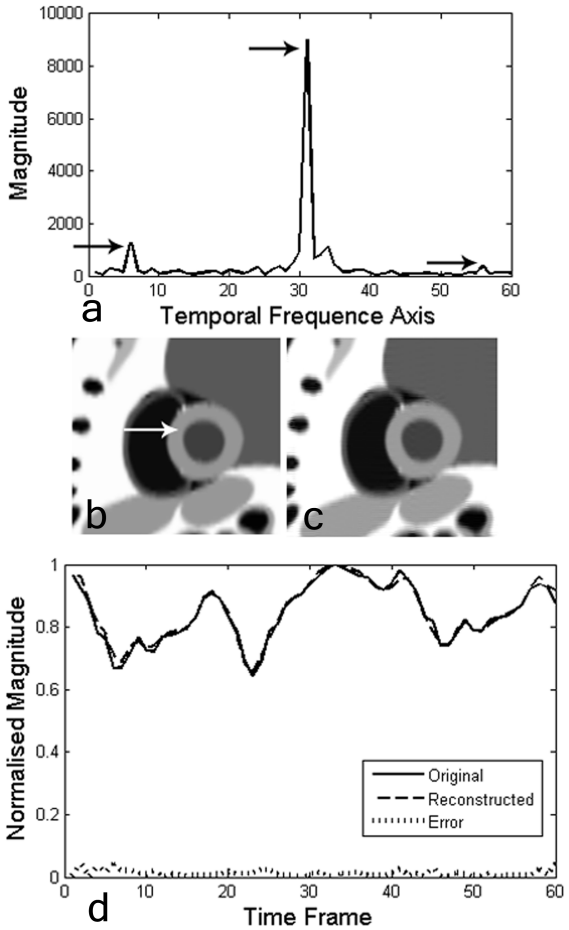

Figure 4.6: **(a):** Spectrum of one of the k-space point after taking Fourier transformation along time frames, where the black arrow indicated the three separate peaks; **(b):** one time frame of original dataset; **(c):** same time frame of reconstructed image after k-space unaliasing; **(d):** Time evolution of the ROI indicated by white arrow; solid line for original dataset, dashed line for reconstructed dataset and dotted line for error between original and reconstructed time frames.

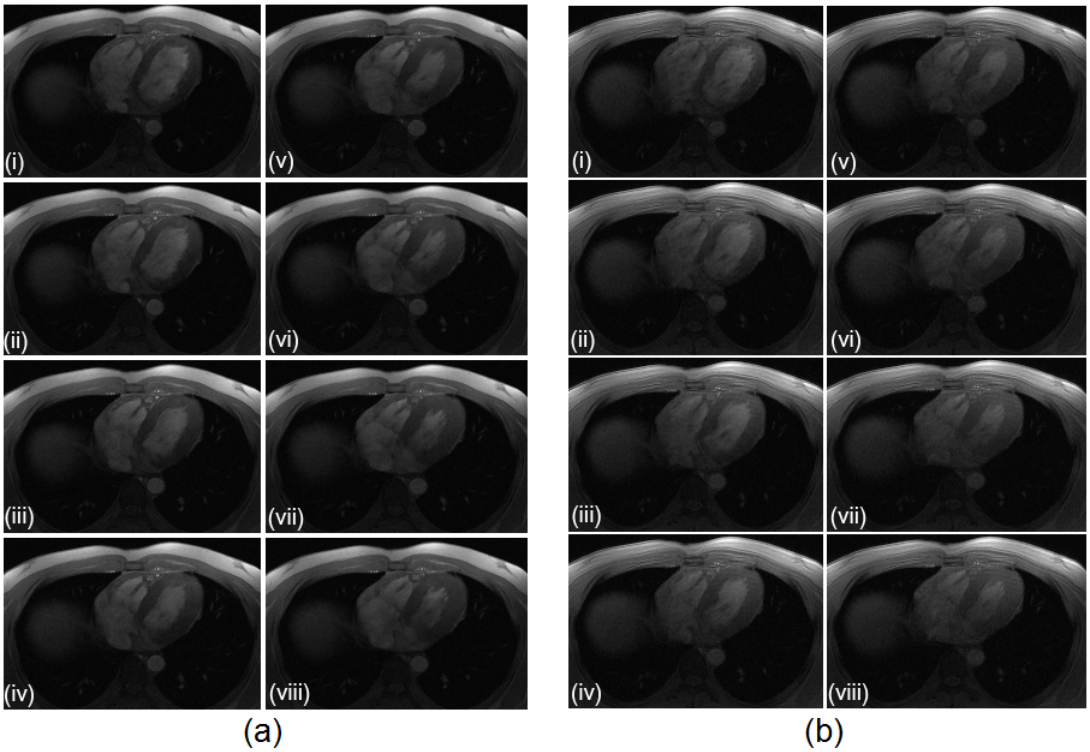

Figure 4.7: **(a):** Eight cardiac phases reconstructed from fully sampled dataset acquired using GRE sequence; **(b):** Eight cardiac phases reconstructed from accelerated dataset with acceleration factor of 2 which acquired using GRE sequence. It can be observed from the images that both the set of images have same quality and there are no visible artifacts due to introduction of aliasing module.

4.4.2 Experimental results

Fig 4.7(a) shows the eight cardiac phases from a fully sampled cardiac triggered cine imaging protocol using GRE sequence and Fig. 4.7(b) shows eight cardiac phases reconstructed from accelerated dataset-I using reconstruction method described in section.4.2.2. It can be seen from the images that both the set of images have similar quality and there are no visible artifacts due to introduction of aliasing module. Fig. 4.8 shows the images reconstructed from accelerated dataset-II with acceleration factor of 3 acquired using GRE sequence. These images are still of high quality but on close inspection we can see a very mild blurring in the images compared to the images reconstructed with acceleration factor of 2.

The aliasing module in our experiments were highly optimized to get minimum possible duration and the duration of aliasing module for acceleration factor of 3 was 4 ms. However this duration is still longer than the conventional single RF pulse used in GRE sequence for excitation. One of the drawback of using aliasing module in GRE sequence is that it increases the TR of the sequence, negating

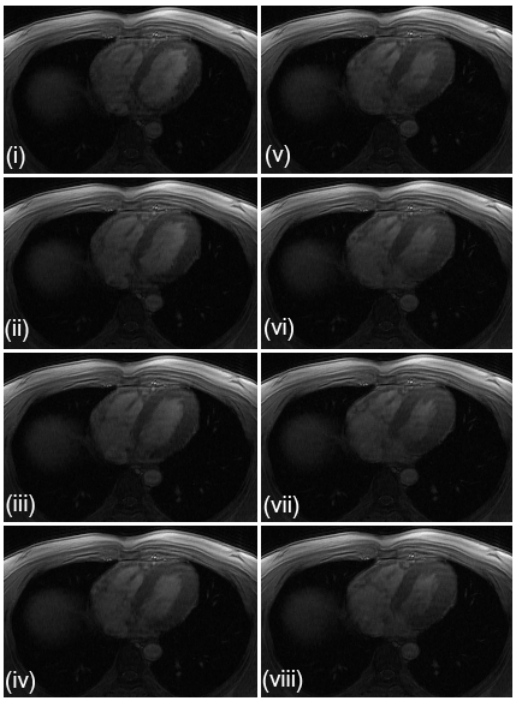

Figure 4.8: Eight cardiac phases reconstructed from accelerated dataset with acceleration factor of 3 acquired using GRE sequence.

some of the acceleration provided by the k-space aliasing technique. To improve upon this problem of increased TR we have incorporated aliasing module for a factor of 3 in an IGEPI sequence. An IGEPI sequence was designed with echo train length of 4, thus the increase in duration introduced by aliasing module was distributed among 4 phase encode lines and effectively the increase in TR per phase encode was minimized. Fig. 4.9 shows the images reconstructed from fully sampled and accelerated datasets-III in IGEPI sequence.

The technique of k-space aliasing can be easily combined with parallel imaging techniques such as SENSE and GRAPPA. K-space aliasing acquires data in aliased form or overlapped form, this aliased k-space data can easily be sub-sampled similar to sub-sampling in parallel imaging. When the aliased k-space data is also sub-sampled then one can use k-space un-aliasing followed by parallel imaging reconstruction to reconstruct the desired full k-space. To validate this technique an aliased k-space data acquired using GRE sequence was retrospectively sub-sampled to simulate aliased and sub-sampled k-space acquisition. The reconstruction of full k-space then became two step process, first k-space un-aliasing was applied to the acquired aliased and sub-sampled data to get sub-sampled k-space data. In the second step GRAPPA reconstruction was applied on sub-sampled data from

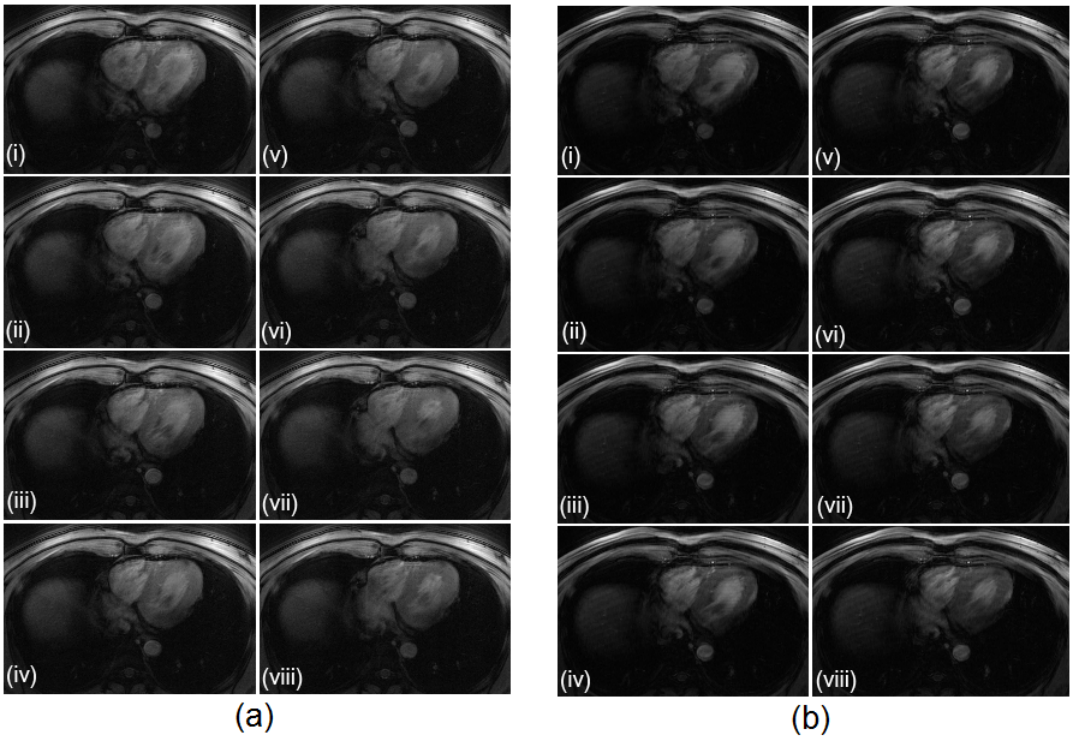

Figure 4.9: **(a):** Eight cardiac phases reconstructed from fully sampled dataset acquired using IGEPI sequence; **(b):** Eight cardiac phases reconstructed from accelerated dataset with acceleration factor of 2 which acquired using IGEPI sequence. It can be observed from the images that both the set of images have same quality and there are no visible artifacts due to introduction of aliasing module.

first step to reconstruct full k-space. The GRAPPA weights was calculated from the first time frame and the same weights were used to reconstruct k-space for every time frame. In real acquisition this requires only one time frame of fully sampled k-space data that would be used to estimate the weights for GRAPPA reconstruction. Using this method we have simulated parallel imaging with PMRI acceleration factor of 2 and 3 on aliased k-space data (k-space aliasing factor of 3) and the reconstruction results are shown in Fig. 4.10. It can be seen on comparing the reconstructed images from fully sampled and accelerated dataset that there were no additional artifacts introduced due to the incorporation of aliasing module in the IGEPI sequence.

4.5 Discussion

In this work, the theory of accelerating dynamic MRI scans via k-aliasing through the RATE method has been presented along with experimental results that validated the same. Several previously proposed non-PMRI/CS techniques attempt

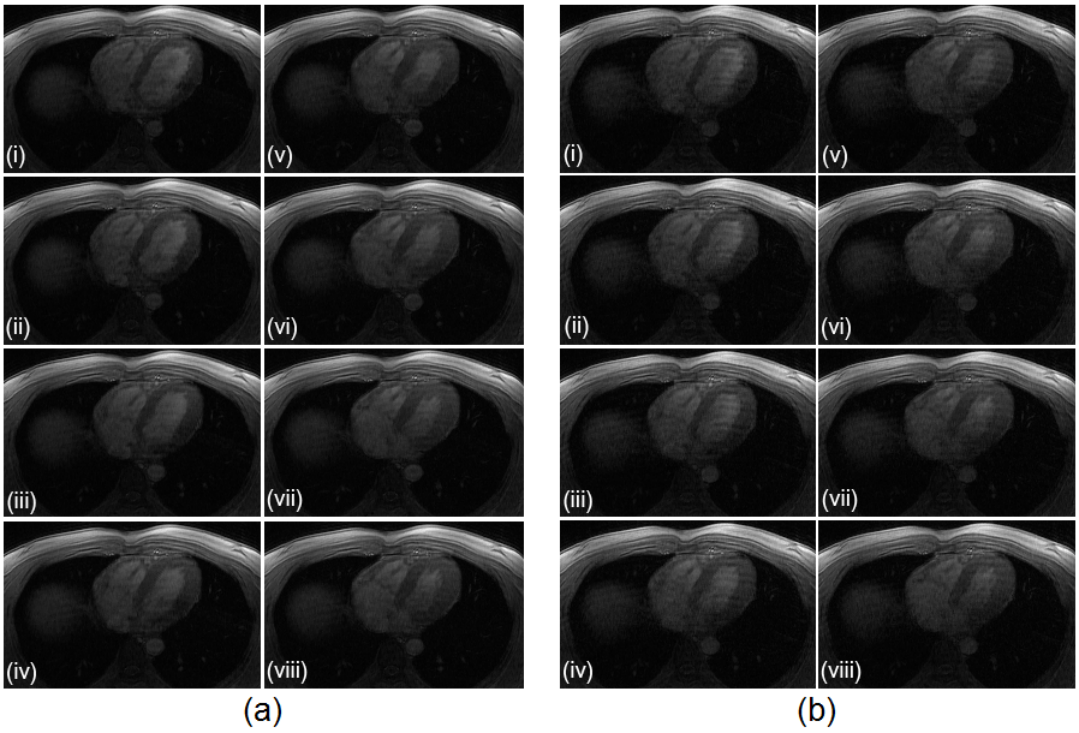

Figure 4.10: (a): Images reconstructed from RATE-PMRI combination, with RATE acceleration factor of 3 and PMRI acceleration factor of 2; **(b):** Images reconstructed from RATE-PMRI combination, with RATE acceleration factor of 3 and PMRI acceleration factor of 3.

to improve the effective temporal resolution of dynamic scans by either skipping some or all high spatial frequencies in every time frame, by sharing data between time frames using a sliding window, by temporally interpolating between acquired data points, or by using low resolution training datasets to correct for any image domain aliasing that may occur in the accelerated datasets. RATE differs from all of these approaches in the following ways: It accelerates a dynamic MRI scan by deliberately causing k-space aliasing rather than image-domain aliasing. Secondly, due to k-aliasing, it is able to sample all k-space points in every time frame and restores the un-aliased k-space data through a simple temporal filtering process. Finally, RATE does not rely on any priory training datasets to correct k-aliasing.

Methods to accelerate MRI scans through the use of multiple RF excitation pulses during excitation have been proposed before [115–117]. The signal excitation approach as proposed in this work circumvents some of the design constraints that limit the broader applicability of these methods for scan acceleration purposes. For instance, the RATE module addresses the issue of slice selection and can be designed to image any slice at any orientation. Furthermore, the simultaneous acquisition of overlapped phase encodes is achieved without any alteration in the duration of the readout gradients. Finally, the RATE module can preserve the

original properties of the pulse sequence into which it is inserted at the expense of a small increase in the TE and TR of the original sequence.

Another interesting property of the RATE module is that when it is designed to overlap single phase encodes, the image domain aliasing artifact is identical to that of sub-sampled PMRI data. As a result, it is possible to use receiver sensitivity maps to correct for the same although as mentioned before, the block aliased approach is ideal when using RATE in combination with PMRI. Nevertheless, noise propagation due to reconstruction will be different from conventional PMRI although whether the same is beneficial or not is yet to be determined.

4.5.1 Image Artifacts

A typical artifact that one can expect to see in an image reconstructed from a k-space dataset that contains residual aliasing is an oscillatory artifact spread along the phase encoding dimension. The severity of this artifact is a function of SNR and the extent of spectral overlap in the temporal spectrum of the accelerated dataset.

For example, the temporal spectrum of an accelerated dataset contains the temporal spectra of all the overlapped k-space points. Each of these will in turn consist of its own DC coefficient. Provided these DC coefficients have not been corrupted by k-aliasing, they can be extracted to reconstruct a baseline estimate of the underlying morphology. The signals in the image domain can be considered to fluctuate around this baseline estimate and the SNR of this baseline will determine whether or not the distortions from the oscillatory artifacts appear severe. This is because the oscillatory artifacts affect the range of signal fluctuations and a poor SNR baseline image will make the same appear exaggerated. Another property of these artifacts is that except under extreme k-aliasing conditions, the artifacts will always remain confined to the most dynamic regions of the image. The largely static regions of the reconstructed image will always remain artifact-free. The static regions will be corrupted by the oscillatory artifact only when the DC components in the spectra of the overlapped points are also corrupted due to substantial spectral overlap.

4.5.2 Implementation challenges

The integration of the RATE module into the IGEPI sequence resulted in certain constraints on the flip angles of the RF pulses in the RATE module. The cumulative flip angle of the RATE module had to remain less than or equal to 45°. For

larger cumulative flip angles, oscillatory artifacts were introduced due to k-space aliasing caused by the unwanted signal pathways, which were no longer negligible.

A second, minor correction that needed to be performed during accelerated data reconstruction was the correction for the relative differences in phase between the various FIDs generated by the RATE module. These can be corrected for by taking into account the RF excitation frequencies and the inter-pulse durations within the module. However, when off-resonance components such as Fat exist, this correction will be sub-optimal for the same that could result in minor blurring and ringing artifacts vis-a-vis the fat component in the image.

With regards to other pulse sequences, the implementation challenges will vary. For example, with SSFP sequences, the increment in RF phase values as a function of time frame number will result in multiple signal pathways whose interference will cause in severe image artifacts. Therefore, whether or not to use the RATE module in an SSFP sequence has to be determined by taking into consideration the imaging conditions. For instance, with real time imaging, a single time frame can be fully acquired using the RATE module in an SSFP sequence since the RF phases will remain constant for the duration of the acquisition for the particular time frame. However, the transverse steady state must be spoiled after the last phase overlapped encode has been acquired as the RF phases for the next time frame will be different due to the data tagging process. Therefore, the steady state condition will have to be re-established for each new time frame resulting in some acquisition inefficiency.

4.6 Conclusion

We have developed and tested a new imaging technique called RATE that relies on k-space aliasing to accelerate dynamic MRI scans. Future work will involve using CS with RATE-PMRI to demonstrate greater acceleration factors. Furthermore, for certain overlapped k-space acquisitions, receiver sensitivity maps can be used to correct for the resultant image domain artifacts potentially broadening the scope of application of the proposed method to even non-dynamic imaging conditions. This remains an active area of investigation and our initial work along these lines has shown promise.

Chapter 5

Accelerating k-t sparse using k-space aliasing for dynamic MRI

5.1 Introduction

When acquiring dynamic scene, there is one more dimension of time frames. The data thus acquired is a three dimensional data called k-t space, two dimension of space and one dimension of time. In order to exploit redundancy along time frames various techniques were proposed such as k-t blast/k-t sense [11], k-t GRAPPA [48], k-t focus [77] and k-t sparse [76]. Here we focus on one of the technique of CS for dynamic imaging, k-t sparse. k-t sparse is a compressive sensing acceleration technique for dynamic imaging that exploits sparsity in k-t space.

In Chapter 4, we have developed a new method of acceleration for reducing scan time in dynamic imaging called k-space aliasing. The technique of k-space aliasing overlaps different portions of k-space and acquires the overlapped/aliased k-space data. The acquired aliased data is then resolved by taking a simple Fourier transformation along time.

The technique of k-space aliasing exploits redundancy in temporal domain to reconstruct image from under-sampled data, while the k-t sparse technique exploits k-t domain sparsity to reconstruct image from randomly under-sampled k-t space data. As the two aforesaid techniques exploits two different kind of redundancy in the acquired data, it make sense to combine both in order to achieve further acceleration in dynamic imaging. Therefore, in this chapter we propose a novel method to combine k-t sparse and k-space aliasing to achieve higher acceleration than each of the individual techniques alone.

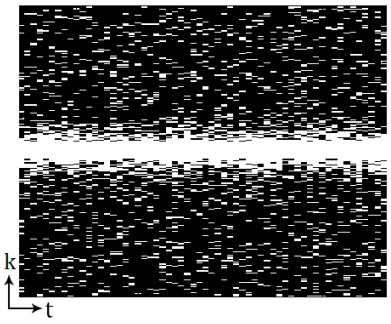

Figure 5.1: Each time frame when randomly under-sampled in phase encode direction with different sampling pattern would result in 2D random under-sampling pattern in k-t space as shown in this figure.

5.2 Background

5.2.1 k-space aliasing

In Chapter 4, an aliasing module that acquires k-space data in aliased from was described in detail.

5.2.2 k-t sparse

K-t sparse [76] is a technique that exploits spatiotemporal sparsity to accelerate dynamic MRI scans. Equidistant under-sampling in k-t space results in aliasing artifact in spatial – temporal frequency (x-f) space. However random under-sampling of k-t space as shown in Fig. 5.1 results in incoherent aliasing artifact in x-f space. The aliasing artifact is also incoherent in sparse transform domain (Wavelet transform in space and Fourier transform in time). This incoherent aliasing artifact in transform domain can be removed by minimizing the sparse representation of k-t space subjected to data fidelity constraint by solving the following non-linear minimization program

$$\min_{x} \quad \|\psi x\|_{l_1} + \lambda \|Fx - y\|_{l_2} \tag{5.1}$$

where x is the dynamic scene and ψ represent the sparsifying transform operator, F is under-sampled Fourier transform operator, y is acquired data after random order under-sampling of phase encodes and λ is a regularization parameter that enforces data consistency and determines the allowed noise level in the reconstructed image.

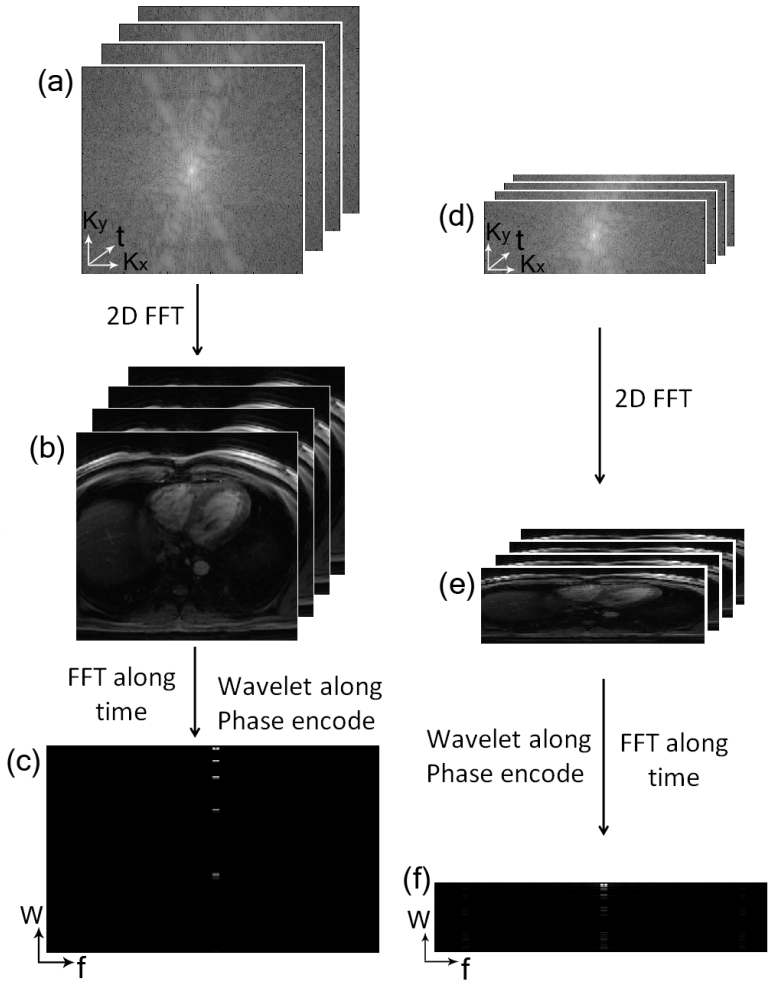

Figure 5.2: **(a)** k-space time frames; **(b)** imaging sequence; **(c)** sparse representation of k-t space; **(d)** overlapped k-space data acquired using k-space aliasing module; **(e)** images obtained by 2D FFT of acquired overlapped data; **(f)** sparse representation of overlapped k-t space.

5.3 Proposed Technique

In k-t sparse Fourier transform is used along time and wavelet tranform is used along phase encode direction to sparsify the imaging sequence. Fig. 5.2(a) shows k-space data acquired without using k-space aliasing module and Fig. 5.2(c) shows sparse representation of the imaging scene. Similarly Fig. 5.2(d) shows the data acquired using k-space aliasing module designed for factor of 3; Fig. 5.2(e) shows the images reconstructed using 2D Fourier transform of aliased k-space data and Fig. 5.2(f) shows their sparse representation. It is evident from Fig. 5.2(d) that the aliased k-space data is also sparse in the same transform domain, however the level of sparsity has changed and it has become less sparse compared to Fig. 5.2(c).

If aliasing module is used in any pulse sequence then effectively we are acquiring

data from an aliased or overlapped k-space. Hereafter, we term the phase encodes acquired using aliasing module as aliased phase encodes (**APE**). While using k-space aliasing module the sequence developer has the flexibility to choose which APEs to acquire. Therefore in order to combine k-space aliasing with k-t sparse, we propose to randomly under-sample the APEs that would result in incoherent aliasing artifact in x-f space. Here we represent X_u to be 2D Fourier transform of K_{alias} ($K_{alias} \overset{FFT}{\longleftrightarrow} X_u$). Similarly, imaging sequence X to be 2D Fourier transform of full k-space data set K ($K \overset{FFT}{\longleftrightarrow} X$).

1. First the acquired data (aliased and under-sampled) is subject to a minimization program that approximate the overlapped k-t space instead of full k-t space.

$$\min_{x} \quad \|\psi X_u\|_{l_1} + \lambda \|F X_u - y\|_{l_2} \tag{5.2}$$

   where λ is the regularization parameter for solving minimization program and F is Fourier transformation operator.

2. Once the aliased k-space data K_{alias} is recovered through Step1, then applying a simple Fourier transformation along time and use of fermi filter can recover the desired k-space data (X) as discussed in k-space aliasing section.

5.4 Simulation Results

The feasibility of the proposed technique was validated on cardiac triggered dataset acquired using Siemens Skyra 3T human scanner. Informed consent was taken from the volunteer in accordance with institute policy. Aliaising module designed for acceleration factor of 3 was inserted in place of RF excitation pulse in an interleaved gradient echo EPI sequence to acquire overlapped k-space data set with echo train length (ETL) = 4, FOV = 300×300 mm^2, TR = 12 ms, cardiac phases = 48, segment size = 4, number of segment = 16, APEs = 80, number of heart beats = 16 and acquisition window = 700 ms (acquisition time after ECG trigger). Echo train length of 4, results in acquisition of 4 APEs for each cardiac phase giving temporal resolution of 12 ms. Echo shifting [113] was implemented in the IGEPI sequence to suppress ghosting due to FAT. The images were reconstructed with k-space unaliasing reconstruction resulting in 48 time frames of size 240×240 pixels. These images were used as reference image for all the simulation presented here.

For simulating k-t sparse, each time frame was under-sampled in phase encode direction with different sampling pattern that would result in 2D random under-sampling pattern in k-t space (Fig. 5.1). The minimization program given in eq.(5.1) was solved using nonlinear conjugate gradient algorithm to recover the imaging sequence. Result for the same is shown in Fig. 5.3(b), (c) and (d).

For simulating k-t sparse and k-space aliasing combination, first the k-space data was overlapped as shown in Fig. 5.2(d) to form aliased k-space; then random under-sampling of aliased phase encode (APE) was done to generate a 2D random under-sampling in k-t space. In reconstruction, first eq.(5.2) was solved to recover aliased k-space data that was then subject to k-space unaliasing reconstruction method to recover full k-space data set. The result for the same is shown in Fig. 5.3(e), (f), and (g). In case of the proposed combination of k-space aliasing and k-t sparse the total acceleration factor would be multiplication of acceleration factor due to k-space aliasing and k-t sparse. It is evident from the simulation results that the proposed method preserves resolution of image and removes incoherent aliasing artifact better than k-t sparse.

Table.1 shows that mean square error (MSE) at different acceleration factors for the k-t sparse alone and the proposed 'combination of k-space aliasing and k-t sparse'. The MSE for the proposed combination was always less than the k-t sparse alone. Therefore, the proposed combination performs better than the k-t sparse at all acceleration factors. Moreover as the acceleration factor increases, the increase in MSE for the k-t sparse was more than that of increase in MSE for the proposed combination. Therefore, the proposed combination becomes even more superior to the k-t sparse at higher acceleration factors.

Table 5.1: Mean square error at different acceleration factors

Acceleration factor	k-t sparse	Proposed method
4	5.5890×10^{-5}	4.9813×10^{-5}
6	5.5977×10^{-5}	4.9817×10^{-5}
8	5.6100×10^{-5}	4.9846×10^{-5}

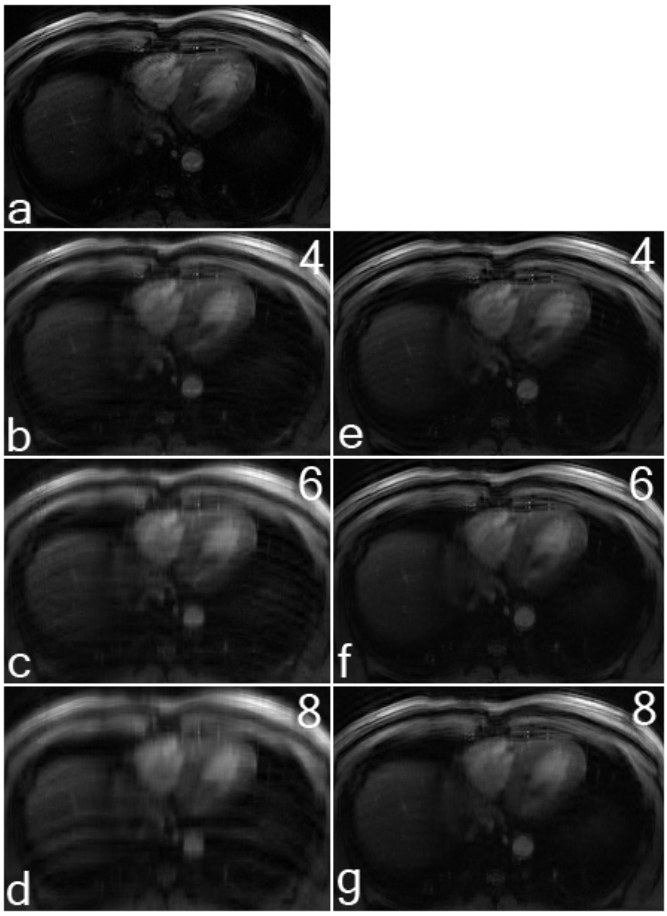

Figure 5.3: **(a)** One time frame of reference image; **(b), (c)** and **(d)** are reconstructed image by k-t sparse for acceleration factors of 4, 6 and 8 respectively; **(e), (f)** and **(g)** are reconstructed image by the proposed method for total acceleration factor (k-space aliasing acceleration factor × k-t sparse acceleration factor) of 4 (3×1.33), 6 (3×2) and 8 (3×2.66) respectively.

5.5 Discussion

K-space aliasing exploits redundancy in temporal domain by allocating targeted temporal bandwidth to different region of k-space, while k-t sparse exploits sparsity of k-t space in transform domain. Therefore each of the technique exploits different redundancy of the imaging process and their combination provides acceleration that would not be achievable by each of the individual techniques alone.

A critical factor in k-t sparse reconstruction is the ratio n/N, where n is the number of acquired PEs and N is the number of targeted PEs to be reconstructed after l_1 minimization. This ratio will be very low when k-t sparse alone is used as compared to the k-t sparse and k-space aliasing combination. For instance, if k-t sparse alone was used and the total number of targeted PEs were 300 and the acquired PEs were only 50, then the ratio n/N would be 0.1667 . However, for the 'k-t sparse and k-space aliasing combination' the target N will be aliased

k-space consisting of only 100 APEs, and the acquired APEs will still be 50. This increases the ratio n/N to 0.5, thereby dramatically increasing the performance of l_1 minimization component of the proposed combination. Also this technique applies the l_1 minimization on aliased k-space (reduced dimension) data, thereby significantly reducing the required computation time to solve non-linear program.

K-space aliasing has been combined with GRAPPA and compressed sensing (CS) in Chapter 4. When combined with GRAPPA, the achievable acceleration factor would be limited by g-factor of the coil geometry. However when combined with CS, the achievable acceleration factor would be limited by sparsity of image and incoherence due to sampling pattern. This scheme differs from the previously presented scheme [39], as it exploits spatiotemporal sparsity rather than only spatial sparsity and exploits 2D incoherence rather than 1D incoherence during reconstruction. The combination of k-space aliasing with GRAPPA or k-t sparse achieves higher acceleration than each of the individual techniques alone. The more optimal combination would be to combine all the three k-space aliasing, GRAPPA and k-t sparse that can provide very high frame rate dynamic imaging. However as the acceleration factor increases there is an inherent penalty on the SNR of the reconstruction. Therefore the above mentioned combination should be used after evaluation of the speed and SNR requirement of the specific clinical imaging application.

5.6 Conclusion

A novel sampling method to rapidly acquire k-t space is proposed. The proposed method reconstructs high frame rate MR images by exploiting both sparsity and temporal redundancy. This method has potential to be used in clinical applications requiring high spatial and temporal resolution.

Chapter 6

Summary and Recommendation

The outcome of the research work undertaken in this thesis is the development of two novel data acquisition techniques and their combination with the parallel imaging and the compressive sensing techniques. Thus the title "Compressive parallel MRI for accelerated imaging" fits well to the thesis. In the first part of the thesis acceleration method for static imaging was developed and in the second part acceleration method for dynamic imaging was developed. The key contribution of the thesis are consolidated into the following points:

- A novel data acquisition method to acquire data in noiselet domain instead of conventional Fourier domain to accelerate static MRI scans using mutichannel compressive sensing is developed. The simulation and experimental results suggest that the noiselelt encoding MCS-MRI outperforms conventional Fourier encoding MCS-MRI and produces higher quality images.

- An empirical analysis comparing the performance of noiselet encoded MCS-MRI over Fourier encoded MCS-MRI is presented. The empirical analysis concludes that for multichannel CS, noiselet measurement matrix have better RIP compared to Fourier measurement matrix. Thus the noiselet encoded MCS-MRI outperforms Fourier encoded MCS-MRI.

- A novel data acquisition method of acquiring aliased k-space data using multiple RF excitation pulses to accelerate dynamic MRI scans is developed.

- A combination of k-space aliasing with parallel imaging technique GRAPPA and with compressive sensing technique k-t sparse is developed. The proposed combination results in high frame rate cardiac cine imaging.

This research work developed two novel data acquisition and reconstruction methods and many possible future extension on them are possible. Some interesting future possibilities are listed below:

- Empirical analysis on noiselet measurement matrix shows large improvement in condition number. Therefore SENSE reconstruction alone can be used with noiselet encoded data to improve the performance of SENSE reconstruction.

- One of the limitation of the current implementation of noiselet encoding pulse sequence is that it can be used only for 2D imaging where one direction is noiselet and other is Fourier. To optimally exploit better RIP provided by noiselet measurement matrix, 3D imaging is better candidate for noiselet encoding MCS-MRI. Therefore, we propose the designing of multidimensional noiselet RF excitation pulses in 3D noiselet encoding where two dimensions will be noiselet encoded and third direction will be Fourier encoded.

- The current implementation of noiselet encoding can only be used under low flip angle regime (flip angle$\leq 30^{\circ}$) that results in some sacrifice of the available SNR. In order to improve the SNR, we propose to design of large flip angle noiselet excitation pulse using SLR algorithm.

- Feasibility of k-space aliasing is shown only for the 2D cardiac cine imaging. It will be interesting to see the application of k-space aliasing and its combination with PMRI, to other dynamic applications such as functional neuroimaging and perfusion which require high temporal resolution.

Bibliography

[1] *Principles of Magnetic Resonance Imaging*. Stanford University Press, 1996.

[2] M. Lustig, D. Donoho, and J. M. Pauly, "Sparse MRI: The application of compressed sensing for rapid MR imaging," *Magnetic Resonance in Medicine*, vol. 58, pp. 1182–1195, 2007.

[3] R. Jones, O. Haraldseth, T. Müller, P. Rinck, and A. Øksendal, "K-space substitution: A novel dynamic imaging technique," *Magnetic resonance in medicine*, vol. 29, no. 6, pp. 830–834, 1993.

[4] J. J. Van Vaals, M. E. Brummer, W. Thomas Dixon, H. H. Tuithof, H. Engels, R. C. Nelson, B. M. Gerety, J. L. Chezmar, and J. A. Den Boer, "keyhole method for accelerating imaging of contrast agent uptake," *Journal of Magnetic Resonance Imaging*, vol. 3, no. 4, pp. 671–675, 1993.

[5] M. Suga, T. Matsuda, M. Komori, K. Minato, and T. Takahashi, "Keyhole method for high-speed human cardiac cine MR imaging," *Journal of Magnetic Resonance Imaging*, vol. 10, no. 5, pp. 778–783, 1999.

[6] M. Doyle, E. G. Walsh, G. G. Blackwell, and G. M. Pohost, "Block regional interpolation scheme for k-space (BRISK): A rapid cardiac imaging technique," *Magnetic resonance in medicine*, vol. 33, no. 2, pp. 163–170, 1995.

[7] M. Doyle, E. G. Walsh, R. E. Foster, and G. M. Pohost, "Rapid cardiac imaging with turbo BRISK," *Magnetic resonance in medicine*, vol. 37, no. 3, pp. 410–417, 1997.

[8] F. R. Korosec, R. Frayne, T. M. Grist, and C. A. Mistretta, "Time-resolved contrast-enhanced 3d MR angiography," *Magnetic Resonance in Medicine*, vol. 36, no. 3, pp. 345–351, 1996.

[9] A. V. Barger, W. F. Block, Y. Toropov, T. M. Grist, and C. A. Mistretta, "Time-resolved contrast-enhanced imaging with isotropic resolution and broad coverage using an undersampled 3d projection trajectory," *Magnetic resonance in medicine*, vol. 48, no. 2, pp. 297–305, 2002.

[10] C. Mistretta, O. Wieben, J. Velikina, W. Block, J. Perry, Y. Wu, and K. Johnson, "Highly constrained backprojection for time-resolved MRI," *Magnetic resonance in medicine*, vol. 55, no. 1, pp. 30–40, 2006.

[11] J. Tsao, P. Boesiger, and K. P. Pruessmann, "k-t BLAST and k-t SENSE: Dynamic MRI with high frame rate exploiting spatiotemporal correlations," *Magnetic Resonance in Medicine*, vol. 50, no. 5, pp. 1031–1042, 2003.

[12] X. Hu and T. Parrish, "Reduction of field of view for dynamic imaging," *Magnetic resonance in medicine*, vol. 31, no. 6, pp. 691–694, 1994.

[13] T. B. Parrish and X. Hu, "Hybrid technique for dynamic imaging," *Magnetic resonance in medicine*, vol. 44, no. 1, pp. 51–55, 2000.

[14] J. O. Fredrickson and N. J. Pelc, "Temporal resolution improvement in dynamic imaging," *Magnetic resonance in medicine*, vol. 35, no. 4, pp. 621–625, 1996.

[15] K. Scheffler and J. Hennig, "Reduced circular field-of-view imaging," *Magnetic resonance in medicine*, vol. 40, no. 3, pp. 474–480, 1998.

[16] B. Madore, G. H. Glover, N. J. Pelc, *et al.*, "Unaliasing by fourier-encoding the overlaps using the temporal dimension (UNFOLD), applied to cardiac imaging and fMRI," *Magnetic Resonance in Medicine*, vol. 42, no. 5, pp. 813–828, 1999.

[17] C. Oesterle and J. Hennig, "Improvement of spatial resolution of keyhole effect images," *Magnetic resonance in medicine*, vol. 39, no. 2, pp. 244–250, 1998.

[18] Z.-P. Liang and P. C. Lauterbur, "An efficient method for dynamic magnetic resonance imaging," *Medical Imaging, IEEE Transactions on*, vol. 13, no. 4, pp. 677–686, 1994.

[19] A. G. Webb, Z.-P. Liang, R. L. Magin, and P. C. Lauterbur, "Applications of reduced-encoding mr imaging with generalized-series reconstruction

(RIGR)," *Journal of Magnetic Resonance Imaging*, vol. 3, no. 6, pp. 925–928, 1993.

[20] D. K. Sodickson and W. J. Manning, "Simultaneous Acquisition of Spatial Harmonics (SMASH): Fast imaging with Radiofrequency Coil Arrays," *Magnetic Resonance in Medicine*, vol. 38, pp. 591–603, 1997.

[21] K. P. Pruessmann, M. Weiger, M. B. Scheidegger, and P. Boesiger, "Sense: Sensitivity Encoding for Fast MRI," *Magnetic Resonance in Medicine*, vol. 42, pp. 952–962, 1999.

[22] K. P. Pruessmann, M. Weiger, P. Bornert, and P. Boesiger, "Advances in Sensitivity Encoding with Arbitrary k-Space Trajectories," *Magnetic Resonance in Medicine*, vol. 46, pp. 638–651, 2001.

[23] M. Bydder, D. J. Larkman, and J. V. Hajnal, "Generalized SMASH imaging," *Magnetic Resonance in Medicine*, vol. 47, pp. 160–170, 2002.

[24] M. Weiger, K. P. Pruessmann, A. Kassner, G. Roditi, T. Lawton, A. Reid, and P. Boesiger, "Contrast-enhanced 3D MRA using SENSE," *Journal of Magnetic Resonance Imaging*, vol. 12, no. 5, pp. 671–677, 2000.

[25] V. Rasche, D. Holz, J. Köhler, R. Proksa, and P. Röschmann, "Catheter tracking using continuous radial mri," *Magnetic resonance in medicine*, vol. 37, no. 6, pp. 963–968, 1997.

[26] S. V. Lossef, S. S. Rajan, R. Patt, M. Carvlin, D. Calcagno, M. Gomes, and K. Barth, "Gadolinium-enhanced magnitude contrast mr angiography of popliteal and tibial arteries.," *Radiology*, vol. 184, no. 2, pp. 349–355, 1992.

[27] P. Lanzer, C. Barta, E. Botvinick, H. Wiesendanger, G. Modin, and C. Higgins, "ECG-synchronized cardiac MR imaging: method and evaluation.," *Radiology*, vol. 155, no. 3, pp. 681–686, 1985.

[28] G. Glover and J. Pauly, "Projection reconstruction techniques for reduction of motion effects in MRI," *Magnetic resonance in medicine*, vol. 28, no. 2, pp. 275–289, 1992.

[29] M. Poustchi-Amin, S. A. Mirowitz, J. J. Brown, R. C. McKinstry, and T. Li, "Principles and Applications of Echo-planar Imaging: A review for the general radiologist," *Radiographics*, vol. 21, no. 3, pp. 767–779, 2001.

[30] R. L. DeLaPaz, "Echo-planar imaging," *Radiographics*, vol. 14, no. 5, pp. 1045–1058, 1994.

[31] K. Oshio and D. A. Feinberg, "GRASE (Gradient-and Spin-Echo) imaging: A novel fast MRI technique," *Magnetic resonance in medicine*, vol. 20, no. 2, pp. 344–349, 1991.

[32] J. Hennig, A. Nauerth, and H. Friedburg, "RARE imaging: a fast imaging method for clinical MR," *Magnetic Resonance in Medicine*, vol. 3, no. 6, pp. 823–833, 1986.

[33] U. Katscher and P. Brnertr, "Parallel magnetic resonance imaging," *The Journal of the American Society for Experimental NeuroTherapeuticse*, vol. 4, pp. 499–510, 2007.

[34] D. K. Sodickson, "Spatial encoding using multiple rf coils: Smash imaging and parallel mri," *Magnetic Resonance in Medicine*, vol. 38, pp. 591–603, 1997.

[35] P. M. Jakob, M. A. Griswold, R. R. Edelman, and D. K. Sodickson, "Auto-smash: A self calibrating technique for SMASH," *Magnetic Resonance Materials in Physics. Biology and Medicine*, vol. 7, pp. 42–54, 1998.

[36] K. Pawar, G. F. Egan, and J. Zhang, "Distributed Compressive Sensing MRI using Noiselet encoding," *IEEE Transaction on Medical Imaging*, vol. (under review).

[37] K. Pawar, A. Arunachalam, G. F. Egan, and J. Zhang, "Noiselet encoded compressive sensing parallel MRI," in *Proc. of the 10th IASTED intl. conf. on Biomedical Engineering, Innsbruck, Austria*, pp. 353–359, ACTA press, 2013.

[38] A. Arunachalam and K. Pawar, "(RATE) Rapid MRI Acquisition using Tailored Signal Excitation modules: A k-space aliasing method to accelerate MRI scans," *Proc. of Intl. Soc. Mag. Res. Med.*, 2012.

[39] K. Pawar and A. Arunachalam, "Simultaneous image and k-space domain aliasing for accelerating dynamic MRI scans," in *Proc. Intl. Soc. Mag. Res. Med*, p. 2236, 2012.

[40] W. S. Hoge, D. H. Brooks, B. Madore, and W. E. Kyriakos, "A Tour of Accelerated Parallel MR Imaging from a Linear Systems Perspective," *Concepts in Magnetic Resonance*, vol. 27A, pp. 17–37, 2005.

[41] D. K. Sodickson, "Tailored SMASH image reconstructions for robust in vivo parallel MR imaging," *Magnetic Resonance in Medicine*, vol. 44, pp. 243–251, 2000.

[42] R. M. Heidemann, M. A. Griswold, A. Haase, and P. M. Jakob, "VD-AUTO-SMASH imaging," *Magnetic Resonance in Medicine*, vol. 45, pp. 1066–1074, 2001.

[43] F. A. Breuer, S. A. Kannengiesser, M. Blaimer, N. Seiberlich, P. M. Jakob, and M. A. Griswold, "General formulation for quantitative G-factor calculation in GRAPPA reconstruction," *Magnetic Resonance in Medicine*, vol. 62, pp. 739–746, 2009.

[44] H. Wang, D. Liang, K. F. King, G. Nagarsekar, Y. Chang1, and L. Ying, "Improving GRAPPA using cross-sampled autocalibration data," *Magnetic Resonance in Medicine*, vol. 67, pp. 1042–1053, 2012.

[45] S. Park and J. Park, "Adaptive self-calibrating iterative GRAPPA reconstruction," *Magnetic Resonance in Medicine*, vol. 67, pp. 1721–1729, 2012.

[46] Y. Chang, D. Liang, and L. Ying, "Nonlinear GRAPPA: A kernel approach to parallel MRI reconstruction," *Magnetic Resonance in Medicine*, 2011.

[47] Z. Chen, J. Zhang, R. Yang, P. Kellman, L. A. Johnston, and G. F. Egan, "IIR GRAPPA for parallel mr image reconstruction," *Magnetic Resonance in Medicine*, vol. 63, pp. 502–509, 2010.

[48] F. Huang, J. Akao, S. Vijayakumar, G. R. Duensing, and M. Limkeman, "k-t GRAPPA: A k-space implementation for dynamic MRI with high reduction factor," *Magnetic Resonance in Medicine*, vol. 54, pp. 1172–1184, 2005.

[49] N. Seiberlich, P. Ehses, J. Duerk, R. Gilkeson, and M. Griswold, "Improved radial GRAPPA calibration for real-time free-breathing cardiac imaging," *Magnetic Resonance in Medicine*, vol. 65, pp. 492–505, 2011.

[50] F. Huang, S. Vijayakumar, Y. Li, S. Hertel, S. Reza, and G. R. Duensing, "Self-calibration method for radial GRAPPA/k-t GRAPPA," *Magnetic Resonance in Medicine*, vol. 57, pp. 1075–1085, 2007.

[51] N. Seiberlich, F. Breuer, R. Heidemann, M. Blaimer, M. Griswold, and P. Jakob, "Reconstruction of undersampled non-cartesian data sets using pseudo-cartesian GRAPPA in conjunction with GROG," *Magnetic Resonance in Medicine*, vol. 59, pp. 1127–1137, 2008.

[52] R. M. Heidemann, M. A. Griswold, N. Seiberlich, M. Nittka, S. A. Kannengiesser, B. Kiefer, and P. M. Jakob, "Fast method for 1D non-cartesian parallel imaging using GRAPPA," *Magnetic Resonance in Medicine*, vol. 57, pp. 1037–1046, 2007.

[53] N. Seiberlich, F. A. Breuer, M. Blaimer, K. Barkauskas, P. M. Jakob, and M. A. Griswold, "Non-Cartesian data reconstruction using GRAPPA operator gridding (GROG)," *Magnetic Resonance in Medicine*, vol. 50, pp. 1257–1265, 2007.

[54] W. Lin, F. Huang, Y. Li, and A. Reykowski, "GRAPPA operator for wider radial bands (GROWL) with optimally regularized self-calibration," *Magnetic Resonance in Medicine*, vol. 64, pp. 757–766, 2010.

[55] R. Baraniuk, "Compressive Sensing," *IEEE Signal Processing Magazine*, vol. 24, pp. 118–121, 2001.

[56] E. Candes, J. Romberg, and T. Tao, "Stable signal recovery from incomplete and inaccurate measurements," *Communications on Pure and Applied Mathematics*, vol. 59, pp. 1207–1223, 2006.

[57] E. Candes and J. Romberg, "Sparsity and incoherence in compressive sampling," *Inverse Problems*, vol. 23, pp. 969–985, 2006.

[58] E. Candes and J. Romberg, "Practical signal recovery from random projections," *Wavelet Applications in Signal and Image Processing XI, Proc. SPIE Conf*, vol. 5914, 2005.

[59] E. J. Candès, J. Romberg, and T. Tao, "Robust uncertainty principles: Exact signal reconstruction from highly incomplete frequency information," *Information Theory, IEEE Transactions on*, vol. 52, no. 2, pp. 489–509, 2006.

[60] E. J. Candès, "The restricted isometry property and its implications for compressed sensing," *Comptes Rendus Mathematique*, vol. 346, no. 9, pp. 589–592, 2008.

[61] E. J. Candes and T. Tao, "Decoding by linear programming," *Information Theory, IEEE Transactions on*, vol. 51, no. 12, pp. 4203–4215, 2005.

[62] K. Ni, S. Datta, P. Mahanti, S. Roudenko, and D. Cochran, "Efficient deterministic compressed sensing for images with chirps and reed-muller codes," *SIAM Journal on Imaging Sciences*, vol. 4, no. 3, pp. 931–953, 2011.

[63] S. S. R. C. L. Applebaum, S. D. Howard, "Chirp sensing codes: Deterministic compressed sensing measurements for fast recovery," *Applied and Computational Harmonic Analysis*, vol. 26, pp. 283–290, 2009.

[64] M. Elad, *Sparse and redundant representations: from theory to applications in signal and image processing*. Springer, 2010.

[65] E. J. Candes and T. Tao, "Near-optimal signal recovery from random projections: Universal encoding strategies?," *Information Theory, IEEE Transactions on*, vol. 52, no. 12, pp. 5406–5425, 2006.

[66] T. Tuma and P. Hurley, "On incoherence of noiselet and haar," (Marseille: France), SAMPTA 09, 2009.

[67] D. L. Donoho, "Compressed sensing," *Information Theory, IEEE Transactions on*, vol. 52, no. 4, pp. 1289–1306, 2006.

[68] E. J. Candes and J. K. Romberg, "Signal recovery from random projections," in *Electronic Imaging 2005*, pp. 76–86, International Society for Optics and Photonics, 2005.

[69] M. Lustig, D. L. Donoho, J. M. Santos, and J. M. Pauly, "Compressed sensing mri," *Signal Processing Magazine, IEEE*, vol. 25, no. 2, pp. 72–82, 2008.

[70] R. Otazo and D. Sodickson, "Distributed compressed sensing for accelerated mri," in *Proceedings of the 17th Annual Meeting of ISMRM*, p. 378, 2009.

[71] D. Liang, B. Liu, J. Wang, and L. Ying, "Accelerating SENSE using compressed sensing," *Magnetic Resonance in Medicine*, vol. 62, no. 6, pp. 1574–1584, 2009.

[72] D. Liang, B. Liu, and L. Ying, "Accelerating sensitivity encoding using compressed sensing," in *Engineering in Medicine and Biology Society, 2008. EMBS 2008. 30th Annual International Conference of the IEEE*, pp. 1667–1670, IEEE, 2008.

[73] R. Otazo, D. Kim, L. Axel, and D. K. Sodickson, "Combination of compressed sensing and parallel imaging for highly accelerated first-pass cardiac perfusion mri," *Magnetic Resonance in Medicine*, vol. 64, no. 3, pp. 767–776, 2010.

[74] M. Lustig and J. M. Pauly, "Spirit: Iterative self-consistent parallel imaging reconstruction from arbitrary k-space," *Magnetic Resonance in Medicine*, vol. 64, no. 2, pp. 457–471, 2010.

[75] J. X. Ji, C. Zhao, and T. Lang, "Compressed sensing parallel magnetic resonance imaging," in *Engineering in Medicine and Biology Society, 2008. EMBS 2008. 30th Annual International Conference of the IEEE*, pp. 1671–1674, IEEE, 2008.

[76] M. Lustig, J. M. Santos, D. L. Donoho, and J. M. Pauly, "kt sparse: High frame rate dynamic mri exploiting spatio-temporal sparsity," in *Proceedings of the 13th Annual Meeting of ISMRM, Seattle*, p. 2420, 2006.

[77] H. Jung, K. Sung, K. S. Nayak, E. Y. Kim, and J. C. Ye, "k-t focuss: A general compressed sensing framework for high resolution dynamic mri," *Magnetic Resonance in Medicine*, vol. 61, no. 1, pp. 103–116, 2009.

[78] C. Qiu, W. Lu, and N. Vaswani, "Real-time dynamic mr image reconstruction using kalman filtered compressed sensing," in *Acoustics, Speech and Signal Processing, 2009. ICASSP 2009. IEEE International Conference on*, pp. 393–396, IEEE, 2009.

[79] H. Jung and J. C. Ye, "Motion estimated and compensated compressed sensing dynamic magnetic resonance imaging: What we can learn from video compression techniques," *International Journal of Imaging Systems and Technology*, vol. 20, no. 2, pp. 81–98, 2010.

[80] E. Candes and J. Romberg, "Sparsity and incoherence in compressive sampling," *Inverse problems*, vol. 23, no. 3, p. 969, 2007.

[81] A. M. Tillmann and M. E. Pfetsch, "The computational complexity of the restricted isometry property, the nullspace property, and related concepts in compressed sensing," *arXiv preprint arXiv:1205.2081*, 2012.

[82] M. Bayati, M. Lelarge, and A. Montanari, "Universality in polytope phase transitions and iterative algorithms," in *Information Theory Proceedings*

(ISIT), 2012 IEEE International Symposium on, pp. 1643–1647, IEEE, 2012.

[83] J. P. Haldar, D. Hernando, and Z.-P. Liang, "Compressed-sensing MRI with random encoding," *IEEE Transactions on Medical Imaging*, vol. 30, 2011.

[84] J. D. Blanchard, "Towards deterministic compressed sensing," in *Proceedings of the National Academy of Sciences,*, pp. 1147–1148, 2013.

[85] G. Puy, J. P. Marques, R. Gruetter, J. Thiran, D. Van De Ville, P. Vandergheynst, and Y. Wiaux, "Spread spectrum magnetic resonance imaging," *Medical Imaging, IEEE Transactions on*, vol. 31, no. 3, pp. 586–598, 2012.

[86] D. Liang, G. Xu, H. Wang, K. F. King, D. Xu, and L. Ying, "Toeplitz random encoding mr imaging using compressed sensing," in *Biomedical Imaging: From Nano to Macro, 2009. ISBI'09. IEEE International Symposium on*, pp. 270–273, IEEE, 2009.

[87] F. Sebert, Y. Zou, and L. Ying, "Compressed sensing mri with random b1 field," *Proc ISMRM,(Toronto, Canada, 2008)*, p. 3151, 2008.

[88] H. Wang, D. Liang, K. King, and L. Ying, "Toeplitz random encoding for reduced acquisition using compressed sensing," *Proc ISMRM,(Honolulu, Hawai, 2009)*, p. 2669, 2009.

[89] X. Qu, Y. Chen, X. Zhuang, Z. Yan, D. Guo, and Z. Chen, "Spread spectrum compressed sensing MRI using chirp radio frequency pulses," *arXiv preprint arXiv:1301.5451*, 2013.

[90] Z. Liu, B. Nutter, and S. Mitra, "Compressive sampling in fast wavelet-encoded MRI," in *Image Analysis and Interpretation (SSIAI), 2012 IEEE Southwest Symposium on*, pp. 137–140, IEEE, 2012.

[91] H. Wang, D. Liang, K. F. King, and L. Ying, "Three-dimensional hybrid-encoded MRI using compressed sensing," in *Biomedical Imaging (ISBI), 2012 9th IEEE International Symposium on*, pp. 398–401, IEEE, 2012.

[92] H. Wang, D. Liang, K. F. King, G. Nagarsekar, and L. Ying, "Three-dimensional hybrid-encoded MRI using compressed sensing," in *International Society of Magnetic Resonance in Medicine Scientific Meeting*, p. 73, 2012.

[93] R. Coifman, F. Geshwind, and Y. Meyer, "Noiselets," *Applied and Computational Harmonic Analysis*, vol. 10, no. 1, pp. 27–44, 2001.

[94] S. Datta, K. Ni, P. Mahanti, and S. Roudenko, "Stability of efficient deterministic compressed sensing for images with chirps and reed-muller sequences," *Applied Mathematics*, vol. 4, p. 183, 2013.

[95] S. Ma, W. Yin, Y. Zhang, and A. Chakraborty, "An efficient algorithm for compressed MR imaging using total variation and wavelets," in *Computer Vision and Pattern Recognition, 2008. CVPR 2008. IEEE Conference on*, pp. 1–8, IEEE, 2008.

[96] L. P. Panych, G. P. Zientara, and F. A. Jolesz, "Mr image encoding by spatially selective rf excitation: An analysis using linear response models," *International journal of imaging systems and technology*, vol. 10, no. 2, pp. 143–150, 1999.

[97] D. Mitsouras, W. S. Hoge, F. J. Rybicki, W. E. Kyriakos, A. Edelman, and G. P. Zientara, "Non-fourier-encoded parallel mri using multiple receiver coils," *Magnetic resonance in medicine*, vol. 52, no. 2, pp. 321–328, 2004.

[98] L. P. Panych, G. P. Zientara, P. Saiviroonporn, S.-S. Yoo, and F. A. Jolesz, "Digital wavelet-encoded mri: A new wavelet-encoding methodology," *Journal of Magnetic Resonance Imaging*, vol. 8, no. 5, pp. 1135–1144, 1998.

[99] L. P. Panych, C. Oesterle, G. P. Zientara, and J. Hennig, "Implementation of a fast gradient-echo svd encoding technique for dynamic imaging," *Magnetic resonance in medicine*, vol. 35, no. 4, pp. 554–562, 1996.

[100] Y. Kim, J. Fessler, and D. Noll, "Smoothing effect of sensitivity map on fmri data using a novel regularized self-calibrated estimation method," in *Proc. Intl. Soc. Mag. Res. Med*, p. 1267, 2008.

[101] P. M. Margosian, G. DeMeester, and H. Liu, "Partial Fourier acquisition in MRI," *eMagRes*, 1996.

[102] G. McGibney, M. Smith, S. Nichols, and A. Crawley, "Quantitative evaluation of several partial Fourier reconstruction algorithms used in MRI," *Magnetic resonance in medicine*, vol. 30, no. 1, pp. 51–59, 1993.

[103] D. Xu, K. F. King, Y. Zhu, G. C. McKinnon, and Z.-P. Liang, "Designing multichannel, multidimensional, arbitrary flip angle RF pulses using an optimal control approach," *Magnetic Resonance in Medicine*, vol. 59, no. 3, pp. 547–560, 2008.

[104] J. Pauly, P. Le Roux, D. Nishimura, and A. Macovski, "Parameter relations for the Shinnar-Le Roux selective excitation pulse design algorithm," *Medical Imaging, IEEE Transactions on*, vol. 10, no. 1, pp. 53–65, 1991.

[105] J. K. Barral, J. M. Pauly, and D. G. Nishimura, "SLR RF pulse design for arbitrarily-shaped excitation profiles,"

[106] W. A. Grissom, D. Xu, A. B. Kerr, J. A. Fessler, and D. C. Noll, "Fast large-tip-angle multidimensional and parallel RF pulse design in mri," *Medical Imaging, IEEE Transactions on*, vol. 28, no. 10, pp. 1548–1559, 2009.

[107] F. A. Breuer, P. Kellman, M. A. Griswold, and P. M. Jakob, "Dynamic autocalibrated parallel imaging using temporal GRAPPA (TGRAPPA)," *Magnetic Resonance in Medicine*, vol. 53, no. 4, pp. 981–985, 2005.

[108] M. Griswold, M. Blaimer, R. Heidemann, P. Speier, S. Kannengeiser, M. Nittka, F. Breuer, M. Mueller, and P. Jakob, "Rapid evaluation of cardiac function using undersampled radial TrueFISP with GRAPPA," in *Proceedings of the 12th Annual Meeting of ISMRM, Kyoto, Japan*, p. 737, 2004.

[109] P. Kellman, F. H. Epstein, and E. R. McVeigh, "Adaptive sensitivity encoding incorporating temporal filtering (TSENSE)," *Magnetic Resonance in Medicine*, vol. 45, no. 5, pp. 846–852, 2001.

[110] B. Madore, "Using unfold to remove artifacts in parallel imaging and in partial-fourier imaging," *Magnetic resonance in medicine*, vol. 48, no. 3, pp. 493–501, 2002.

[111] A. Haase, J. Frahm, D. Matthaei, W. Hanicke, and K.-D. Merboldt, "Flash imaging. rapid nmr imaging using low flip-angle pulses," *Journal of Magnetic Resonance (1969)*, vol. 67, no. 2, pp. 258–266, 1986.

[112] R. Ordidge, P. Mansfield, and R. Coupland, "Rapid biomedical imaging by nmr," *The British journal of radiology*, vol. 54, no. 646, pp. 850–855, 1981.

[113] G. McKinnon, "Ultrafast interleaved gradient-echo-planar imaging on a standard scanner," *Magnetic resonance in medicine*, vol. 30, no. 5, pp. 609–616, 1993.

[114] B. Sharif and Y. Bresler, "Physiologically improved NCAT phantom (PINCAT) enables in-silico study of the effects of beat-to-beat variability on cardiac MR," in *Proceedings of the Annual Meeting of ISMRM, Berlin*, vol. 3418, 2007.

[115] J. Hennig and M. Hodapp, "Burst imaging," *Magma*, vol. 1, no. 1, pp. 39–48, 1993.

[116] T. J. Mosher and M. B. Smith, "A dante tagging sequence for the evaluation of translational sample motion," *Magnetic Resonance in Medicine*, vol. 15, no. 2, pp. 334–339, 1990.

[117] L. P. Panych, P. D. Jakab, and F. A. Jolesz, "Implementation of wavelet-encoded mr imaging," *Journal of Magnetic Resonance Imaging*, vol. 3, no. 4, pp. 649–655, 1993.